UNIVERSITY OF BELGRADE

SCHOOL OF ELECTRICAL ENGINEERING

Marija M. Ćurčić

# APPLICATION OF QUANTUM AND NONLINEAR PHENOMENON IN HOT POTASSIUM VAPOUR FOR CONTROLING PROPERTIES OF LASER RADIATION

Doctoral Dissertation

Belgrade, 2023.

УНИВЕРЗИТЕТ У БЕОГРАДУ
ЕЛЕКТРОТЕХНИЧКИ ФАКУЛТЕТ

Marija M. Ćurčić

# ПРИМЕНА КВАНТНИХ И НЕЛИНЕАРНИХ ФЕНОМЕНА У ПАРИ КАЛИЈУМА ЗА КОНТРОЛУ ОСОБИНА ЛАСЕРСКОГ ЗРАЧЕЊА

Докторска дисертација

Београд, 2023.

**Supervisor/Ментор:**

Dr. Branislav Jelenković, naučni savetnik

Univezitet u Beogradu – Institut za fiziku

**Jury members/Чланови комисије:**

Dr. Jasna Crnjaski, vanredni profesor

Univezitet u Beogradu – Elektrotehnički fakultet

_____

Dr. Ivan Popović, redovni profesor

Univezitet u Beogradu – Elektrotehnički fakultet

_____

Dr. Dušan Arsenović, naučni savetnik

Univezitet u Beogradu – Institut za fiziku

_____

Defense date/Датум одбране:_____

*To my family*

# Acknowledgement

First and foremost, I would like to express my gratitude to my supervisor, Brana Jelenković, who introduced me to the exciting world of science, and for giving me an opportunity to learn and develop as a researcher. Thank you for continuing to tirelessly pass on your enthusiasm and knowledge to the younger generations. You are an inspiration to all of us.

I would also like to thank our Group leader, Dušan Arsenović, and our colleague Milan Minić. Without their help and assistance the realization of this work wound not be possible.

I also have to use this opportunity to thank our colleagues from the Stuttgart University, who provided us with the cell that I used in the experiment, but also for welcoming me to their Institute and their team during our collaborations.

Finally, I would like to thank my family, for their limitless love and support. I dedicate this thesis to you.

# Abstract

This work presents the study of classical and quantum properties of the four-wave mixing (FWM) process in hot potassium vapour. FWM is a third order nonlinear process in which interaction of two photons, in a nonlinear medium, produce two new photons at different frequencies. Or in terms of usual terminology associated with FWM: two pump photons are converted into probe and conjugate photons. There are different nonlinear media, and different schemes for FWM. Here, the process of FWM is generated on a double-lambda scheme on $D_1$ line of potassium isotope $^{39}K$.

We have studied - in both theoretical and experimental manner - the response of FWM process to various FWM parameters - one-photon pump detuning, two-photon pump-probe detuning, atomic density, and powers of the laser beams. Numerical nonperturbative model, based on Maxwell-Bloch system of equations, has been adopted to the special case of potassium atom and used for calculating a classical property of FWM, the parametric gains of probe and conjugate. It has been demonstrated that FWM in K can result in a higher amplification of the newly generated beams than with any other alkali atom. Both experimental and theoretical results show a strong dependence of the probe and conjugate gains on the FWM parameters.

Studding the probe and conjugate gain was important since it is already established, in Rb and Cs, that the generation of quantum correlation between probe and conjugate, i.e., the twin beams, and the amplitude squeezed light depend on values of gains of the new beams. In that context, the first part of the study of FWM as an amplifier was a prelude to the research work that followed. In the second part of the thesis, the study of FWM as a source of the correlated/entangled beams is presented. We have demonstrated that for the adequate set of experimental parameters this system can produce noise reduction in the difference signal between the correlated probe and conjugate, below the standard quantum limit. We have discussed how various experimental parameters affect the results, and compared the values we have measured with the ones predicted by the models. In the theoretical study of squeezing we have employed phenomenological models, as it was done previously for other alkali species. In addition, we have developed a microscopic model for hot atoms based on Heisenberg-Langevin equations, that enables us to predict both gains and squeezing by FWM that could be obtained in K, as a function of different system parameters. This is the first such study with this alkali atom as FWM medium.

Strong quantum correlations and entanglement between twin beams has been in the focus of interest of many research groups because of important applications: improvements of resolution and sensitivity of different measurement techniques, and for many emerging quantum technologies. Hence, learning about and getting more insights in the way we can efficiently generate and control quantum properties of light have a strong implication on a future of global research and development.

**Key words:** four-wave mixing, potassium, relative-intensity squeezed light

**Scientific field:** Technical physics

**Scientific subfield:** Quantum and nonlinear optics

# Сажетак

Овај рад представља студију класичних и квантних особина процеса четвороструког мешања таласа у загрејаној пари калијума. Ово је нелинеарни процес трећег реда током кога интеракција два фотона, у нелинеарној средини, генерише два нова фотона на различитим фреквенцијама. Или, уколико употребнимо уобичајену терминологију када је овај ефекат у питању, два фотона пумпе се конвертују у фотон пробе и конјуговани фотон. Постоје различите нелинеарне средине и различите шеме за генерисање овог ефекта. Овде се четвороталасно мешање реализује на двострукој ламбда шеми на Д1 линији калијумовог изотопа $^{39}$К.

Проучавали смо, како на теоријски тако и на експериментален начин, одговор процеса мешања на промену различитих параметара, једнофотонског фреквенцијског пемераја пумпе, двофотонског фреквенцијског помераја пробе, густине атома и снаге ласерских снопова. Нумерички непертурбативни модел, заснован на Максвел-Болтзмановим једначинама, је примењен на случај атома калијума и коришћен при рачунању класичних особина које карактеришу четвороталано мешање. тј. појачања пробе и конјугованог снопа. Показано је да четвороталасно мешање у пари калијума може довести до високог појачања новогенерисаних снопова. И експериментални и теоријски резултати показују снажну зависност појачања пробе и конјугиваног снопа у фунцији параметара система.

Студија појачања била је од вежности јер је раније утврђено, када су у питању рубидијум и цезијум, да генерисање кватних корелација између пробе и конјугованог снопа, односно снопова близанаца, и амплитудски стиснуте светлости зависе од вредности појачања. У том констексту, први део студије четвороталсног мешања био је увод у истраживачки рад који је уследио. У другом делу рада приказана је студија четвороталасног мешања као извора корелисаних/увезаних снопова, Показали смо да за адекватан скуп екеспримениталих параметара овај систем може произвести смањење шума у сигналу разлике између пробе и конјугованог, који ће се спустити испод вредности стандардне кванте границе. Извршили смо дискусију на тему утицаја различитих експерименталних параметара на резултате и упоредили вредности које смо измерили са вредностима модела. У теоријској студији коришћени су феноменолошки модели, као сто је раније одрађено за друге алкалне врсте. Поред тога, развили смо микроскопски модел за вруће атоме заснован на Хајзенберг-Ланжевиновим једначинама, који нам омогућава да предвидимо појачања и стискање светлости у функцији различитих параметара система. Ово је прва таква студија са овим алкалним атомом као активно средином.

Снажне квантне корелације које су уочене у сноповима близанцима су у фокусу интересовања многих истраживачких група јер се могу искористити за побољшање осетљивости и резолуције разних мерних техника, као и многе нове квантне технологије. Дакле, учење о и стицаљње увида у начин на који можемо ефиксно генерисати и контролисати ове корелације има снажне импликације за будућност глобалног истраживања и развоја.

**Кључне речи:** четвороструко мешање таласа, калијум, релативно интензитетски стиснута светлост

**Научна област:** Техничка физика

**Ужа научна област:** квантна и нелинеарна оптика

# Table of contents

# 1. Introduction

Research and developments at the frontier of science are constantly and unequivocally changing and reshaping the way we perceive the world around us, so as the our everyday living. We have been exploiting the developments in optical science in all aspect of our lives. Nowadays, research teams at universities and companies are striving and making big steps towards implementing developments from realm of quantum science to practical applications. These attempts are foundation and building blocks of a new *quantum revolution* [1]. Once exotic and mysterious, now topics in quantum science have become an essential part of research and fabrication of new technological platforms.

Quantum science is a field of physics studies that is built on quantum mechanical principles. Its beginning originates at the beginning of the $20^{th}$ century with an efforts to explain the nature of light, departing from the classical framework. It was Albert Einstein's quantum theory of light [2] that struck the foundation of a non-classical understanding of light and matter interaction. In his paper that was based on the Max Planck's work on black body radiation [3], we are for the first time introduced with the existence of light quanta [4], later called photon. These works pawed the way to the still on-going discoveries and research developments in the area of quantum science, and we referred to them as the first quantum revolution. However, it was only with the development of the laser [5], in 1960's, when this research area started rapidly advancing and booming. Invention of lasers turned out to be an invaluable tool in proving the new concepts and theorems of quantum mechanics, so as in the realization of new experiments that unravelled mysteries of quantum world. Within this era of studying fundamental effects that led the first quantum revolution, scientists discovered new ways of generation and control of photons and atomic states. The relevance of these successes, with the nowadays obtainable precision in control and manipulation over the experimental settings, has become even more obvious and dominant when we entered the time of the *second quantum revolution* [6]. The knowledge gained and understanding of the quantum optical world is paving the way to the realization of quantum-inspired devices, which can potentially find application in various areas of both research and everyday life. Quantum based set-ups that, up to recently, were only operational and studied in our laboratory conditions, have become to integrate in every aspect of on-going technological development. With this in mind, we cannot be surprised by the fact that huge sums of money are being invested in the development of this research discipline. There is a world-wide effort and competition between many research institutions and companies in reaching new milestones and breakthroughs.

So, what the tools obtained within the framework of quantum science can offer? Firstly and probably the most obvious, is the aspect of miniaturization, with a constant demand for smaller scale devices for technical applications. Secondly, from a practical perspective, with known properties of light, especially the fact that photons weakly interact with the environment, photon has become a perfect carrier of information over long distances. New concepts relying on the engineering of non-classical photon states and interactions between photons have been proposed for all-optical quantum computation [7] and quantum communication protocols [8,9], and find applications in developments of quantum memory [10-12], quantum metrology [13], quantum sensing [14], and quantum repeaters [15].

Some of the most intriguing topics in quantum optics are probably quantum entanglement and squeezing. Importance of discoveries of non-classical properties of light led to the last year

Nobel Prize award for the work on the experiments demonstrating and investigating quantum entanglement [16,17]. These works present pioneering step in further development of quantum science. Entanglement can be generated in various degrees of freedom. Hence, we can discuss entanglement in time and energy [18], position [19], momentum [20], polarization [21]. These possibilities make entangle photons advantageous over classical light for applications in imaging [22,23], spectroscopy [24], lithography [25], microscopy [26]. Microscopic imaging of biological systems with quantum states of light has shown improvements in precision of phase and absorption measurements [27]. Recently, quantum microscopes based on entangled heralded photons have been demonstrated, with improved sensitivity and signal-to-noise ratio (SNR) [28]. Some of the todays burning topics, like data privacy and internet security advancements are also relying on the practical implementation of quantum generated states of light in communication channels.

Squeezed states have also gained a considerable interest when it comes to their application for increasing precision of measurements [29], quantum interferometry [30], but also in quantum teleportation [31-33], and quantum information [34]. Quantum noise reduction by the means of squeezed light sources has become an integral part of a new class of sensors [35]. When classical noise is sufficiently suppressed, measurements precision becomes quantum noise limited. This quantum noise is known as the shot noise, often referred as the standard quantum limit (SQL), arising from the discrete nature of photons. Continuous research and attempts to overcome this limit are motivated by a growing number of experiments and applications requiring enhancement in sensitivity, resolution and improved signal-to-noise ratio (SNR). The solution was found in definition of Heisenberg uncertainty principle. The Heisenberg uncertainty relation presented in 1927. [36], defining the limitation on the accuracy of particle position and momentum detection, has been one of the most important baselines when it comes to the development of modern quantum science. It imposes a limit on the precision of simultaneous determination of light amplitude and phase, but it doesn't limit them individually. This can be translated in the possibility of minimizing the amplitude noise fluctuations, on the expense of increasing phase uncertainty. This is basically an explanation of what the squeezing is.

Following proposed solution, squeezes states found their role in enhancement of measurements precision in various areas. One example includes application which depends on amplitude modulation such as absorption measurement, where the signal-to-noise ratio is boosted by decreasing the amplitude noise [37,38]. Polzik et al. demonstrated that squeezed light could be utilized for the improvement of a wide range of atomic spectroscopy measurements [39]. Squeezed light with reduced uncertainty in the detected quadrature was used to improve the sensitivity of optical magnetometers [40-41]. We now have demonstrations of plasmonic sensors [42], micromechanical sensors [43], atomic magnetometers [44], LIGO interferometers [45], all of them showing improvements compared to previous class of sensors (their classical predecessor), just by exploiting squeezed light sources. Squeezed light has also been used to improve the sensitivity in photo-sensitive measurements of biological samples [46] and in Raman spectroscopy for probing molecular bonds [47].

Development of one more branch of optics was crucial in order to obtain all of the necessary tools for the generation and study of mentioned quantum light sources. Namely, controlling properties of a medium is a kind of precursor to control of properties of light. Hence, study of so called nonlinear effects [48] has become one of the pillars of the quantum science development during past few decades. For sufficiently strong light field incident on a medium, optical response becomes nonlinear. This response is directly related to the optical susceptibility, which characterizes the properties of a medium. With a development of the lasers, the necessary power levels of light radiation were easily obtained and different nonlinear effects of second and third order, described with second and third order of optical susceptibility, were demonstrated. Of a special interest in our line of studies are wave mixing processes, most commonly obtained in

nonlinear crystals and atomic vapours. In nonlinear crystals, second order nonlinear polarization, induced by the pump field, due to the interaction with incident light can generate new photons at output frequencies. Through the spontaneous parametric down conversion (SPDC) in nonlinear crystal two *correlated twin beams* can be generated [49,50] . This method is a common tool in generation of previously mentioned entangled states. However, conversion efficiency of this process is rather low and the bandwidth of generated photons is large, which is not always desirable when it comes to particular applications. Also, frequencies of generated pair of photons are typically far from atomic transitions, thus limiting application in atomic optics, for quantum state engineering.

Nonlinear effect which is in the focus of our study is generated through the nonlinear interaction with alkali atoms. What sets alkali apart from other elements is their unique energy structure. Their macroscopic properties are very easily controlled [51-53], while their energy structure is sensitive to externally applied electric [54] and magnetic fields [55]. This makes alkali really desirable as an active medium for different spectroscopic applications. Specially, when optical field is tuned close to the atomic resonance, susceptibility of a system highly increases [48]. There is a wide range of nonlinear and quantum effects that were already successfully demonstrated in this type of medium, some of them being electromagnetically induced transparency (EIT) [56], electromagnetically induced absorption (EIA) [57], coherent population trapping (CPT) [58],… These effects had been realized on different atomic schemes, ranging from simpler two [59] and three level [60] systems employing only ground and first exited states, to the ones employing highly exited Rydberg states, in different configurations [61,62]. Nowadays, alkali cells can be miniaturized [63], hence future set-ups can be made more compact. There have already been examples where vapour cells are integrated with semiconductor based quantum dots in order to generate new states of light [64].

In our study, we have utilized Four Wave Mixing (FWM) process. It is nonlinear phenomenon based on optical susceptibility of third order, that presents coherent interaction of four modes of electromagnetic field [48]. It was demonstrated and studied in different types of mediums, ranging from atomical [65-68] to solid ones, like optical fibers [69]. FWM in atomic system has already demonstrated the ability to slow [70,71] and stop light pulses [72] in different alkali elements, such as Rb [71-73], Na [74], and K[70]. It was subject of studies as phase-sensitive [75] and phase-insentive amplification system [76], and as a source of optical nonreciprocity [77]. It was also studied in pump-probe counter-propagating scheme [78]. Multiple applications of FWM have already been demonstrated. But, most relevant for our line of research is the fact that it is useful and promising tool for production of squeezed and entangled photons [79-82]. In a configuration typical for alkali atoms, strong pump and weak probe seed mix to produce pairs of correlated photons so-called twin beams. Due to strong nonlinearity of FWM media, intense parametric amplification of generated twin photons and large squeezing could be obtained in a single pass of the pump beam through atomic vapour. Same as for SPDC, there have been demonstrations of polarization [83,88] and orbital angular momentum [84-86] entangled photon states, and time [81,82,87] and space [89-91] correlated twin-photon pairs.

Squeezing was firstly demonstrated by Schuler [92]. It was generated in sodium (Na) by means of FWM. From then on, different systems have been proposed and tested as a source of squeezed light. The best squeezing by the second harmonic generation reached level of -3 dB in a doubly resonant system [93]. Experiments on pulsed fibre squeezing using the Kerr effect are presented in [94], and eventually have brought the squeezing levels to around -7 dB [95]. Up to date, the best squeezing levels have been obtained with parametric processes in nonlinear crystals, with a -12.3 dB of noise suppression at a wavelength of 1550 nm and −12.7 dB at 1064 nm [96]. In general, squeezing can be generated in a wide range of wavelengths, spanning from 500 nm to 1550 nm. When it comes to atomic based systems, both cold and hot alkali ensembles have been used as

a medium for generation of squeezing. In cold rubidium -3.5 dB of squeezing level was measured [97], while in cold Cs only -1.8 dB was obtained [98]. However, the simplicity of the hot vapour set-ups, with no need for cooling and trapping of atoms and additional cavities, has prevailed as an advantage and experiments utilizing cold mediums moved out of the focus of researches. Light beams in both CW [81,99,100] and pulsed regime have been successfully squeezed in Rb vapour.

Nonlinear Kerr effect, based on the change of effective index of refraction, was also shown to be able to produce squeezed light in atomic vapour, however, with a lower efficiency. Another, alternative way to squeeze light in atomic mediums is thought polarization self-rotation effect. First experimental implementation of this effect for generation of squeezed vacuum was in solid media [101]. Successful demonstration in Rb vapour followed [102], and – 3 dB of squeezing level was eventually reported [103].

With respect to number of squeezed quadratures, we can distinguish two cases – single- and two-mode squeezes states [104]. Different FWM configuration can be used in order to generate either of the mentioned quantum states of light. It is important to distinguish these two possibilities when discussing possible applications. Single-mode (vacuum) squeezed light have been often used in sensing and interferometry [105]. However, multimode and multidimensional squeezed light [106,107] could even have more advantage when it comes to the use in quantum networks systems, quantum computing, imaging, and microscopy.

Renewed interest in a FWM as a source of two-mode squeezing source followed McCormick et al. publication in 2008 [81]. In this work, FWM in Rb vapour was used to generate two-mode squeezing in a joint quadrature of correlated probe and conjugate fields, or intensity difference squeezing (IDS). Large intensity squeezing obtained by phase-insensitive FWM in Rb of -9.2 dB [82] is close to the highest level of squeezing produced by any method for generating squeezed light [108]. This result made FWM in hot alkali vapours widespread method for testing limits of FWM with different gases, and different atomic schemes [99,100,109-112]. Several groups tried different approaches to enhance IDS, by modulating internal energy level with additional laser [113], or by conical pump beam [114]. With FWM based two-beam phase sensitive amplifier, IDS above -10 dB was obtained in Rb vapour [82]. The strongest IDS obtained in hot Cs vapour was -6.5 dB [111]. The difficulty in getting higher quantum correlation in Cs is believed to be due to larger hyperfine splitting (hfs) of the ground state in Cs [110]. Recently, study of IDS based on FWM on double lambda scheme was extended with the use of two pump beams [115,116], generating multi-beam quantum correlation and with integration of FWM system with optical parametric amplifier [117]. Also, multipartite quantum squeezing was demonstrated with cascaded FWM system [118]. These studies could pave the way to expanding the range of the possible applications of IDS based on FWM in atomic vapour. However, not much has been done with potassium [112].

It is obvious that there is a variety of quantum squeeze states that today state-of-art experiments enable us to study. However, each of the mentioned methods of generation has its own advantages and rooms for improvement, which is confirmed by the still present interest of research community into tackling the existing problems and downsides of every method, while trying to push the boundaries of achieved results even further.

Within this thesis, results of a study of FWM in potassium vapour are presented. We conducted both experimental and theoretical study of FWM in co-propagating pump-probe configuration, realized on double-lambda atomic scheme on D1 line in K. We have gained a new insight into the advantages of a studied system as a phase-insensitive amplifier. We have also tested FWM in Potassium as a source of relative intensity squeezing. We aimed to show that K is competitive with other alkali elements. The initial idea presented in [81] was followed, and a set-up

for a squeezing on a far detuned scheme was developed, first time demonstrated in K. We have explored different parameters that can increase the squeezing level and attempt to find to ones for maximal noise reduction. Alongside to the experimental work, we have developed the first microscopic quantum model for calculation of squeezing and gain produced by FWM in hot atomic vapour, while taking into account all of decoherence effects, Doppler broadening and transit time of the atoms through the interaction area. The model has been tested in several regimes of interest and results presented in this thesis.

Of a special interest in our research group is a possibility of implementing this type of light sources for enhanced optical microscopy and spectroscopy. Getting the more insights and detailed knowledge into the processes occurring at the atomic and molecular level of biological system is definitely one of the reasons for conducting the research presented in this thesis. Our developed set-up, with the obtained results, has a potential of being a tool for nondestructive and noninvasive imaging of biological system by the means of entangled two-photon absorption (ETPA), since efficient generation of time correlated photons has been confirmed.

# Part I

# Study of classical properties of Four Wave Mixing in Potassium vapour

# 2. Light – alkali atoms interaction

In our study, we are interested in the interaction of the light radiation and atomic medium. Hence, in this chapter we give an introductory overview over the basic concepts of atom-light interactions on which the process of FWM is based. Description of the main tools is given, starting with atomic specie that was used as an active medium in our work. Then, we introduce a two level system driven by an incident light, and its theoretical description, as the simplest approximation of the studied schemes. The more complex modelling of three-level $\Lambda$ system follows. In this part of the thesis we use a semi-classical theoretical approach. In this manner, we characterize and describe the atomic medium as a quantum system, while the light filed is presented classically. The content of this chapter is based on the references [51,119-122].

## 2.1. Alkali atoms - Potassium

Atomic mediums interacting with the light radiation have been shown to be a rich source of interesting phenomena, as pointed out in the introduction. One of the steps in successful understanding, generation and control of this interaction is becoming familiar with the active medium being in use. Experiments based on the atomic vapours have been extensively studied for the past few decades. When the light field frequencies are close to the atomic transitions, strong nonlinear response could be expected, under certain conditions. Alkali metal group elements (Rb, Cs, K, Na, Li) has been attracting special interest. Although characteristics and properties of these elements have been well-documented and number of experiments in quantum and nonlinear physics already carried out, weather in thermal or laser-cooled atoms, the interest in these mediums is still not waning. Their electronic structure, with a one valence electron, makes them similar to a hydrogen atom, hence, relatively easy for theoretical simulations. This characteristic also leads to strong interactions with external magnetic and electrical fields, making them useful in quantum atomic experiments and applicable for precise sensing elements, like, for example, atomic clocks [123]. In addition, nowadays, there are plenty of available and affordable laser sources at frequencies for probing atomic transitions of interest in alkali metals. Specially, thermal alkali vapours have shown to be a key part of a number of experiments in quantum and nonlinear physics. When it comes to the advantages of hot vapour system compared to the use of cold active medium, one of the most important is considerably lower price of the experimental set-up, its simplification and miniaturization. On the other hand, a wide number of effects could still be realized and demonstrated.

In this manuscript, we present a study performed with a cell filled with $^{39}$K atoms. Rubidium and Caesium have been popular choice in experiments exploring nonlinear light-matter integration, and effects producing new, quantum sources of light. However, there were only few studies on these topics employing Potassium. The first study done by our group, with potassium [124], gave us a hint that this element could compete with the rubidium and caesium, and be successfully used in quantum optics experiments, and formed the starting point for the further work.

There are three isotopes of potassium - $^{39}$K, $^{40}$K and $^{41}$K, of which $^{40}$K is radioactive. For the purpose of using potassium in experimental conditions, it is stored in glass cells, which can be of different shapes and sizes. In the following sections, some of the most important properties of potassium are listed and summarized, which consequently dictate the requirements of the system for FWM in potassium for both classical and quantum studies. More detailed review is presented in [51,122].

### 2.2.1. Atomic structure – fine and hyperfine structure

Now, we take a look and the energy structure of atom of our choice. On the Figure 2.1, partial potassium energy structure is presented, including only transitions of interest. Namely, we can observe so-called doublet or fine structure of potassium atom. It is a result of spin-orbit coupling, i.e. the interaction between the electron spin angular momentum S and its orbital angular momentum L. The total angular momentum J is defined with:

$$\boldsymbol{J} = \boldsymbol{L} + \boldsymbol{S}. \tag{2.1}$$

The associated magnitudes of angular momentums are described with quantum numbers $S, L$ and $J$, that present the eigenstates of the operators $S^2$, $L^2$ and $J^2$. Here, $J$ has to satisfy:

$$|L - S| \leq J \leq L + S, \tag{2.2}$$

and can take a value of integer or half integer. For potassium, $S = 1/2$, value of $L$ is zero or positive integer. Hence, for a ground state of $^{39}$K, $4S$, since $L = 0$, $J$ can only take a value of $J = 1/2$. For the first excited state, $4P$, we have $L = 1$, hence two possible values for $J$: $J = 1/2$ and $J = 3/2$. This leads to the doublet structure of Potassium, and the two presented D-lines, one of which, $D_1$, couples the ground state $4S_{1/2}$ to the excited state $4P_{1/2}$, and other, $D_2$, that couples the ground state $4S_{1/2}$ to the excited state $4P_{3/2}$, as presented on Figure 1.

Next, there is a coupling between the total angular momentum J and the total nuclear angular spin momentum I, from which hyperfine structure arises. It is described with total atomic angular momentum F, defined with:

$$\boldsymbol{F} = \boldsymbol{J} + \boldsymbol{I}. \tag{2.3}$$

Similarly, magnitude $F$ can take values from the following range:

$$|J - I| \leq F \leq J + I. \tag{2.4}$$

Value of quantum number $I$ is different for each potassium isotope. For a $^{39}$K, nuclear spin $I = 3/2$ [122]. The hyperfine splitting of the ground state gives two sublevels with $F_g = 1$ and $F_g = 2$, while the excited $4P_{1/2}$ splits into two sublevels with $F_e = 1$ and $F_e = 2$, and $4P_{3/2}$ into four sublevels with $F_e = 0$, $F_e = 1$, $F_e = 2$ and $F_e = 3$. In our research, our focus is on the $D_1$ transition, with four mentioned transitions, around 770 nm.

The energy split of the ground state can be calculated according to [122]:

$$\Delta E_{hf} = \frac{1}{2}A + B\frac{\frac{3}{2}K(K+1) - 2I(I+1)J(J+1)}{4I(2I-1)J(2J-1)}. \tag{2.5}$$

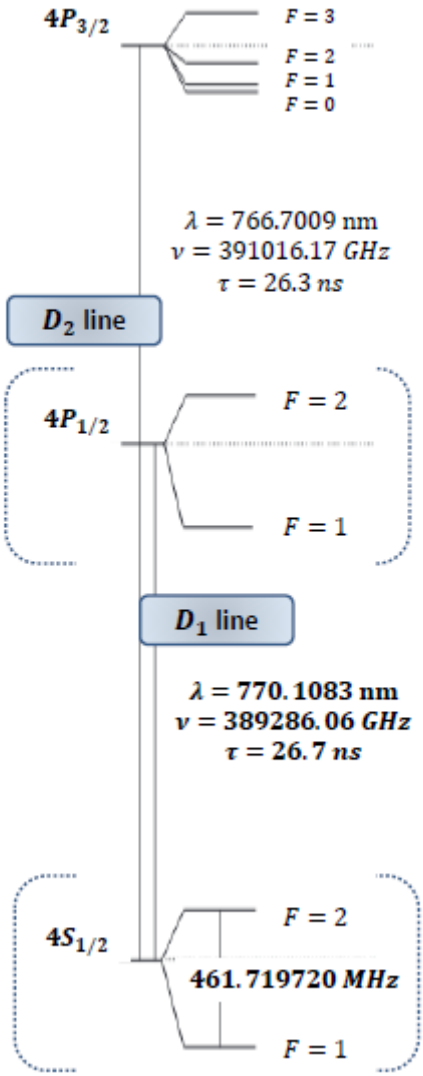


Figure 2.1 $^{39}$K doublet D-level structure.

Here, the magnetic dipole is characterized by $A$, $B$ is the electronic quadrupole constant, while $K = F(F+1) - I(I-1) - J(J-1)$. The main differences, between potassium and commonly used elements, like rubidium and caesium, are the smaller fine and hyperfine splittings. Specially the value of the hyperfine splitting of the ground state in $^{39}$K, of 462 MHz, makes it really intriguing and promising as a medium for some of the mentioned studies.

In addition, hyperfine energy levels can be split into Zeeman sublevel, when atoms are exposed to the weak external magnetic field. This splitting is a consequence of the interaction of the magnetic dipole moment of the electron with a magnetic field. As a result, each hyperfine sublevel is further split into $m_F$ states, where $m_F$ is a projection of $F$ onto a quantization axis defined by magnetic field. It is integer, and takes values from $-F$ to $+F$. This splitting widens the spectra of possible interesting application of these atomic medium due to its specific energy structure.

### 2.2.2. Physical and optical properties of potassium

In this section, we review particular properties of potassium vapours. As it was already mentioned, there are three natural isotopes of potassium. These isotopes slightly differ by the atomic mass, have different nuclear spins and the transition frequencies, as noted in the Table 2.1.

Table 2.1 The main properties of different potassium isotopes (data taken from [51,122])

| Mass number $A$ | Neutrons $N$ | Abundance (%) | $m$ (u) | $\tau$ | $I$ |
|---|---|---|---|---|---|
| 39 | 20 | 93.2581(44) | 38.96370668(20) | stable | 3/2 |
| 40 | 21 | 0.0117(1) | 39.96399848(21) | $1.28 \times 10^9$ y | 4 |
| 41 | 22 | 6.7302(44) | 40.96182576(21) | stable | 3/2 |

*Atomic density*

When it comes to the potassium, as is the case with other alkaline elements, there is a possibility for a relatively simple manipulation of some parameters of the atomic medium, in order to target its desired characteristics, which makes it really appealing for the use in previously mentioned experiments. One of the most important features, when using hot alkali vapours, is the option to change the density of atoms only by changing the temperature.
We operate our medium at thermal equilibrium. In that state, the behaviour of the gas can be described by an ideal gas law, in the limit of low pressure:

$$PV = nk_BT. \tag{2.6}$$

Here, $P$ is the vapour pressure, $V$ is the occupied volume, $T$ is the gas temperature, $n$ the number of atoms, and $k_B$ is the Boltzmann constant. On the other hand, the vapour pressure can be approximated by corrected Boyle law [125] in the following way:

$$P = 10^{a-\frac{b}{T}}, \tag{2.7}$$

where, for the potassium vapour, coefficients $a$ and $b$ have the following values:

$$\begin{aligned} a = 7.9667, b = 4646\ K,\ \ 289 < T < T_m \\ a = 7.4077, b = 4453\ K,\ \ T_m < T < 600, \end{aligned} \tag{2.8}$$

for $T_m$ being the temperature of melting. Finally, from the equations (2.6) and (2.7), we can calculate the expected atomic density of potassium as a function of temperature:

$$N \equiv \frac{n}{V} = \frac{P}{k_BT} \tag{2.9}$$

Expected relation is presented on Figure 2.2.

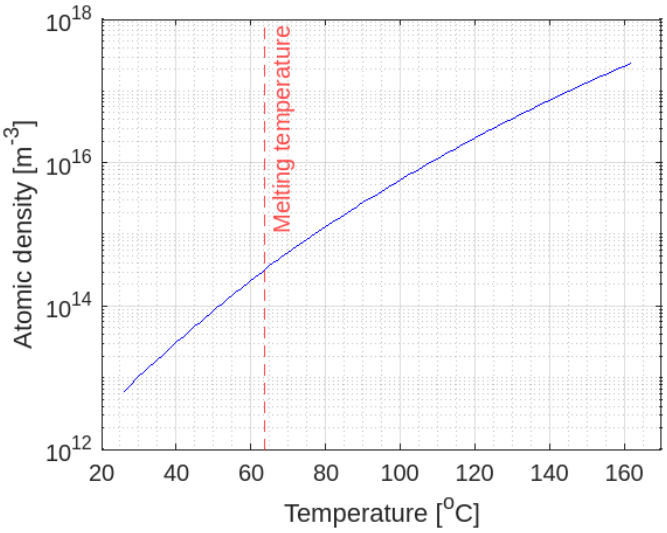


Figure 2.2 Atomic density of potassium as a function of temperature.

*Doppler Effect (averaging)*

At the experimental operational temperatures, atoms move at the mean velocity:

$$\bar{v} = \sqrt{\frac{8k_B T}{\pi m_a}}. \tag{2.10}$$

Due to this motion, we have to take into consideration an effect of Doppler broadening. Namely, atoms moving at different velocities are subjected to the different frequencies of light due to the Doppler effect. As a result, an incident laser frequency $\omega_L$ seen by the atom is $\omega = \omega_L - \mathbf{kv}$. Hence, we have to take into account, when discussing this system, a shift of an atomic transition frequencies by:

$$\Delta_D = -\boldsymbol{kv} = \mp k v_z. \tag{2.11}$$

Here, $\boldsymbol{k}$ is a wave vector of the incident light, assumed to be propagating in $z$-direction, and $v_z$ is the velocity projection on the propagation axis. The atoms will have a distribution of velocities described by the Maxwell-Boltzmann function:

$$M(v) = \frac{1}{\bar{v}\sqrt{\pi}} \exp\left(\frac{-v^2}{\bar{v}^2}\right). \tag{2.11}$$

The atomic motion significantly modifies the line shape around the resonance. In a warm atomic vapour this effect is crucial to understand the dynamics of the system, as Doppler broadening can be much greater than the natural linewidth $\Gamma$. For an atom of a mass $m$ at temperature $T$ the Doppler linewidth $\Gamma_D$ is given by:

$$\Gamma_D = \omega \sqrt{\frac{8ln(2)k_B T}{mc^2}}, \tag{2.12}$$

where $m$ and $\omega$ are the mass of an atom and frequency of the transition, respectively. On the Figure 2.3, Doppler broadening of D1 line of $^{39}$K is presented as a function of temperature. One can notice,

that at the temperatures above $100^{o}C$, which are of interest in our experiments, broadening of the line is way above the natural linewidth of $\Gamma \approx 6$ MHz. Even at the room temperature this broadening exceeds the value of hyperfine splitting of the ground state of potassium, making it impossible to distinguish respective transitions from these sublevels to the same excited state. This leads us to the conclusion that energy levels of interest will be masked by the Doppler broadened line and not observable. In order to resolve them, different experimental techniques have been developed. One of them, employed in our experiment will be described in the following chapter.

When modelling the behaviour of a hot vapour system, and its response to interaction with light radiation, one has to consider performing Doppler averaging over the velocity classes.

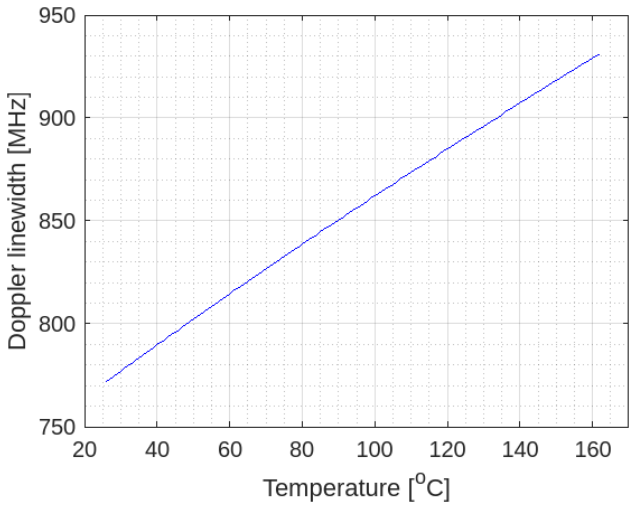


Figure 2.3 Doppler linewidth of potassium D1 line as a function of temperature.

*Optical depth*

The density of alkali vapour significantly affects the optical depth of the cell medium, atomic polarization, and atomic relaxation rate. As a function of the density, absorption of the light propagating through the atomic medium is defined with:

$$\alpha = n\sigma_0, \tag{2.12}$$

where $\sigma_0$ is the cross section of the optical transition. The optical depth, $OD = \alpha L$, can be measured according to the changes in the light intensity passing the atomic cloud. Based on the Lambert-Beer law of absorption for the beam of initial intensity $I_0$, we have:

$$I = I_0 exp(-\alpha L), \tag{2.13}$$

where $L$ is the length of atomic medium. Optical depth quantifies the absorption on the resonance, hence, it is an important parameter in calculations of the system response.

*Saturation intensity*

Besides the optical absorption, we should consider optical saturation, parameter that also depends on choice of an atomic species. Previously defined cross section of a transition applies for low intensity light fields. However, higher intensities can modify the medium behaviour, in accordance with which we can define the saturation intensity, $I_{sat}$. The saturation intensity is defined, such that, if a laser beam is resonant with an atomic transition and has an intensity $I_{sat}$, the atom will spend one quarter of its time in the excited state (the intensity at which the resonant scattering rate is half that of its maximum possible value). In this case, the cross section reduces compared to its initial value $\sigma_0$, and we can write [126]:

$$\sigma = \frac{\sigma_0}{1 + I/I_{sat}}. \tag{2.14}$$

In terms of atomic parameters, $I_{sat}$ can be calculated in a following way:

$$I_{sat} = \frac{\pi hc\Gamma}{3\lambda^3} = \frac{hc\Gamma}{3\lambda\sigma_0} = \frac{h\omega^3\Gamma}{12\pi c^2}. \tag{2.15}$$

Often, in our experiments, we are detuned with the laser frequencies from the resonant transitions, and it is useful to introduce the proper calculation of described medium parameters for particular case. If the light is detuned by $\Delta = \omega - \omega_0$, we have:

$$I_{sat}(\Delta) = (1 + 4(\Delta/\Gamma)^2) I_{sat}(0), \tag{2.16}$$

and

$$\sigma(\Delta) = \frac{\sigma_0}{1 + 4(\Delta/\Gamma)^2 + I/I_{sat}}. \tag{2.17}$$

## 2.2. Theory of light-matter interaction

### 2.2.1. Maxwell's equations and wave propagation equation

For the description of light propagation through the medium we utilize a propagation equation. In order to derive it, we start with the well-known set of Maxwell's equations for description of creation and propagation of electro-magnetic field:

$$\nabla \times E = -\frac{\partial B}{\partial t}, \tag{2.18}$$

$$\nabla \times H = j + \frac{\partial D}{\partial t}, \tag{2.19}$$

$$\nabla \cdot D = \rho, \tag{2.20}$$

$$\nabla \cdot B = 0. \tag{2.21}$$

Here, $E$ is electric field, $H$ magnetic field, $D$ is electric flux density, while $B$ is magnetic flux. A total current density and free charge density are denoted with $j$ and $\rho$, respectively.
The relationship between the electric displacement and electric field is described by:

$$D = \varepsilon_0 E + P, \tag{2.22}$$

where $P$ is polarization, and $\varepsilon_0$ free space electric permittivity. Similarly, we have

$$B = \mu_0 H + M, \tag{2.23}$$

with $\mu_0$ as magnetic permeability of a free space, and magnetization $M$. In our case, non-magnetic medium is of interest, hence we can neglect magnetic polarization. In addition, there are no free charges or currents. Taking this into account, Maxwell's equations obtain following form:

$$\nabla \times E = -\frac{\partial B}{\partial t}, \tag{2.24}$$

$$\nabla \times B = \mu_0 \frac{\partial D}{\partial t}, \tag{2.25}$$

$$\nabla \cdot D = 0, \tag{2.26}$$

$$\nabla \cdot B = 0. \tag{2.27}$$

Taking the curl of the equation $(2.24)$ , and combining it with a time derivative of $(2.25)$, we get

$$\nabla \times (\nabla \times E) = \nabla \times \left(-\frac{\partial B}{\partial t}\right) = -\mu_0 \frac{\partial^2 D}{\partial t^2}. \tag{2.28}$$

With the use of vector identity

$$\nabla \times (\nabla \times E) = \nabla(\nabla \cdot E) - \nabla^2 E, \tag{2.29}$$

one can obtain following:

$$\nabla(\nabla \cdot E) - \nabla^2 E = -\mu_0 \frac{\partial^2 D}{\partial t^2}. \tag{2.30}$$

Assuming that the plane wave is transverse and infinite, meaning $\nabla \cdot E \approx 0$, we can write:

$$\nabla^2 E = \mu_0 \frac{\partial^2 D}{\partial t^2}. \tag{2.31}$$

Finally, we obtain wave propagation equation for the electric field:

$$\nabla^2 E - \frac{1}{c^2}\frac{\partial^2 E}{\partial t^2} = \mu_0 \frac{\partial^2 P}{\partial t^2}, \tag{2.32}$$

where $c$ is defined with $c = \frac{1}{\sqrt{\varepsilon_0 \mu_0}}$.

### 2.2.2. Density matrix approach

For a description of a medium, density matrix formalism is used. As it was already mentioned, within the semi-classical theoretical approach, atomic medium is treated quantum mechanically. Namely, all information about the closed system of interest are contained within the state vector, noted as $|\psi\rangle$.

Time evolution of the system is described with the time-dependent Schrodinger equation:

$$\frac{\partial|\psi\rangle}{\partial t} = -\frac{i}{\hbar}H|\psi\rangle, \tag{2.33}$$

where Hamiltonian is given by:

$$H = H_0 + H_{int}. \tag{2.34}$$

Here, $H_0$ is unperturbed Hamiltonian, which, in the absence of the external field or any dissipation effects, is described with:

$$H_0 = \sum_i \mathcal{E}_i|i\rangle\langle i|. \tag{2.35}$$

$\mathcal{E}_i = \hbar\omega_i$ is the energy eigenvalue for a corresponding eigenstate $|i\rangle$. $H_{int}$ describes the interaction of an atom with an electrical field $\boldsymbol{E}$. This is perturbation energy, related to the projection of an electric dipole $\boldsymbol{d}$ onto the electric field:

$$H_{int} = -\boldsymbol{d}\cdot\boldsymbol{E}(\boldsymbol{r},t). \tag{2.36}$$

Since, usually, the size of the atom is small compared to the light wavelength, we can apply electric dipole approximation and assume that the field is spatially constant $\boldsymbol{E} = E(t)$.

The Schrodinger equation is useful for describing an evolution of a pure state. However, for a description of a mixed state and effects that cannot be described statistically, it is more convenient, and sometimes even necessary to switch to a different notation, i.e. density formalism. Hence, we introduce density matrix operator, as an outer product of the wavefunction and its conjugate:

$$\hat{\rho} = |\psi\rangle\langle\psi|. \tag{2.37}$$

The expectation value of an operator $\hat{A}$ is calculated in a following way:

$$\langle\hat{A}\rangle = Tr(\hat{\rho}\hat{A}). \tag{2.38}$$

For a state of an atomic ensemble, i.e. mixed state, we write the density matrix operator as:

$$\hat{\rho} = \sum_i P_i\,|i\rangle\langle i|, \tag{2.39}$$

where $P_i$ is the probability amplitude for a state $|i\rangle$.

If we disregard the spontaneous emission, the time evolution of a density operator is described with generalized Schrodinger equation, so-called von Neumann equation:

$$\frac{\partial\rho}{\partial t} = -\frac{i}{\hbar}[H,\rho]. \tag{2.40}$$

The master equation above gives us the population dynamics of a quantum state of atomic ensemble. Obtained diagonal elements of the density matrix will contain the information on the populations of the states, while off-diagonal elements characterises the coherence between the states.

As already mentioned, the equation (2.40) only consider absorption and stimulated emission. For the realistic description of the studied systems, one also has to include decay and relaxation terms. These decoherence processes are accounted by the Lindblad operator:

$$L = \sum_{i,j} \left( 2C_{ji}\rho {C_{ji}}^{\dagger} - \left( \rho {C_{ji}}^{\dagger} C_{ji} + {C_{ji}}^{\dagger} C_{ji} \rho \right) \right) / 2, \tag{2.41}$$

with $C_{ji} = c_{ji}\sqrt{\Gamma_i}|j\rangle\langle i|$ and $\sum_j |c_{ji}|^2 = 1$, where $\Gamma_i$ is decay rate of an excited state, which is anti-proportional to the state lifetime. The first term in Lindblad operator is diagonal and gives information on the repopulation due to spontaneous decay. The second part describes dephasing effects and other mechanisms of the repopulation.

Finally, we have Lindblad maser equation:

$$\frac{\partial \rho}{\partial t} = -\frac{i}{\hbar}[H, \rho] + L. \tag{2.42}$$

### 2.2.3. Two-level system

First, we consider simple system of two levels, schematically presented on the Figure 2.4. We start with a pure states of an atom, with ground state $|g\rangle$ and an excited state $|e\rangle$, with $\omega_g$ and $\omega_e$ as their angular frequencies, respectively. States have the energies $\hbar\omega_g$ and $\hbar\omega_e$, which results in the transition energy of:

$$E = \hbar(\omega_e - \omega_g) = \hbar\omega_{eg}. \tag{2.43}$$

State of the system is described with a wavefunction:

$$\psi(\boldsymbol{r}, t) = c_g \langle \boldsymbol{r}|g\rangle e^{-i\omega_g t} + c_e \langle \boldsymbol{r}|e\rangle e^{-i\omega_e t}, \tag{2.44}$$

where $c_g$ and $c_e$ are coupling coefficients.

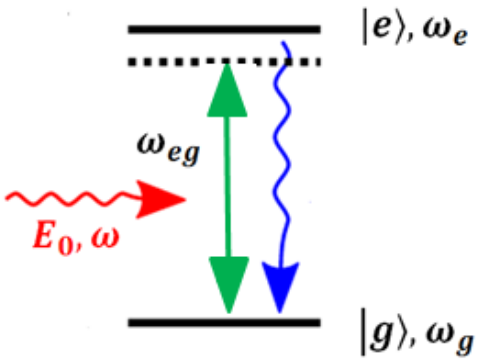


Figure 2.4 Energy scheme of two-level system.

In order to characterize the system we have to define the Hamiltonian of an atom driven with a time dependent light radiation, that induces a dipole. Atomic Hamiltonian of unperturbed system is:

$$H_0 = \hbar\omega_g|g\rangle\langle g| + \hbar\omega_e|e\rangle\langle e|. \tag{2.45}$$

Assuming that $\hbar\omega_g = 0$, we get:

$$H_0 = \hbar\omega_{eg}|e\rangle\langle e|. \tag{2.46}$$

Light-atom interaction is described with interaction Hamiltonian, as a response to oscillating electrical field $\boldsymbol{E}(t)$:

$$\boldsymbol{E}(t) = E_0\boldsymbol{e}cos(\omega t) = E_0\boldsymbol{e}(e^{i\omega t} + e^{-i\omega t})/2. \tag{2.47}$$

Here, $E_0$ is an amplitude of electric field, and $\boldsymbol{e}$ is the orientation of field polarization. The dipole transition operator describes the measure of the interaction strength and has a following form:

$$\boldsymbol{d} = \boldsymbol{d}_{eg}|e\rangle\langle g| + \boldsymbol{d}_{ge}|g\rangle, \tag{2.48}$$

with $\boldsymbol{d}_{eg} = \boldsymbol{d}_{ge}^*$. Dipole operator contains only off-diagonal elements, as it is non-zero only for states of opposite parity [127]. We assume that the light induced dipoles are aligned to the field polarization, hence:

$$H_{int} = -Ed(|g\rangle\langle e| + |e\rangle\langle g|). \tag{2.49}$$

Next, we introduce Rabi frequency:

$$\Omega = -\frac{E_0 d_{ge}}{\hbar}, \tag{2.50}$$

which describes a strength of the coupling between the states. Usually, we model the light as a Gaussian beam, so we can write:

$$E_0 = \sqrt{\frac{4P}{c\epsilon_0\pi w^2}}, \tag{2.51}$$

where P is the power, $w$ beam waist, and $\epsilon_0$ the vacuum permittivity. Then Rabi frequency can be calculated as:

$$\Omega = -\frac{d_{ge}}{\hbar}\sqrt{\frac{4P}{c\epsilon_0\pi w^2}}. \tag{2.52}$$

Now, we can solve a Schrodinger equation (2.33) for the total Hamiltonian that is given by:

$$H = H_0 + H_{int} = \\ = c_g e^{-i\omega_{eg}t}|g\rangle\langle g| + c_e e^{-i\omega_e t}|e\rangle\langle e| - \frac{\Omega}{2}\left(e^{i\omega t} + e^{-i\omega t}\right)|g\rangle\langle e| - \frac{\Omega}{2}\left(e^{i\omega t} + e^{-i\omega t}\right)|e\rangle\langle g|. \tag{2.53}$$

One can notice that Hamiltonian is time dependent. However, we can get rid of this dependence. Having in mind that $|g\rangle\langle e| \sim e^{-i\omega_{eg}t}$ and $|e\rangle\langle g| \sim e^{+i\omega_{eg}t}$, we obtain the following set of differential equations:

$$\frac{\partial c_g}{\partial t} = i\frac{\Omega}{2}\left(e^{i(\omega-\omega_{eg})t} + e^{-i(\omega+\omega_{eg})t}\right)c_g, \tag{2.54}$$

$$\frac{\partial c_e}{\partial t} = i\frac{\Omega}{2}\left(e^{-i(\omega-\omega_{eg})t} + e^{i(\omega+\omega_{eg})t}\right)c_e. \tag{2.55}$$

The rotating wave approximation (RWA) allows us to neglect the fast oscillating terms, i.e. $e^{i(\omega+\omega_{eg})t}$, since they will average to zero over the time period of interest. If we define a detuning $\Delta = \omega - \omega_{eg}$, set of equations $(2.54) - (2.55)$ can be rewritten in the next form:

$$\frac{\partial c_g}{\partial t} = i\frac{\Omega}{2}e^{i\Delta t}c_g, \tag{2.56}$$

$$\frac{\partial c_e}{\partial t} = i\frac{\Omega}{2}e^{-i\Delta t}c_e. \tag{2.57}$$

If we substitute $c_g e^{-i\Delta t}$ and $c_e e^{i\Delta t}$ with $\tilde{c}_g$ and $\tilde{c}_e$, respectively, we get the following matrix form for the previous set of equations:

$$\frac{\partial}{\partial t}\begin{bmatrix}\tilde{c}_g \\ \tilde{c}_e\end{bmatrix} = \frac{i}{2}\begin{bmatrix}-\Delta & \Omega \\ \Omega & \Delta\end{bmatrix}\begin{bmatrix}\tilde{c}_g \\ \tilde{c}_e\end{bmatrix}. \tag{2.58}$$

With this we can fully describe a behavior of the system with pure states. In the case of a resonant transition $\Delta = 0$ , for a system with initial conditions $\tilde{c}_g(t=0) = 1$ and $\tilde{c}_g(t=0) = 0$, with all the population in the ground state, the result of the equation (2.58) is:

$$\tilde{c}_g(t) = \cos\left(\frac{\Omega t}{2}\right), \tag{2.59}$$

$$\tilde{c}_e(t) = \mathrm{i}\sin\left(\frac{\Omega t}{2}\right). \tag{2.60}$$

The state populations can then be calculated:

$$\rho_{gg} = \left|\tilde{c}_g(t)\right|^2 = \cos^2\left(\frac{\Omega t}{2}\right), \tag{2.61}$$

$$\rho_{ee} = |\tilde{c}_e(t)|^2 = \sin^2\left(\frac{\Omega t}{2}\right). \tag{2.62}$$

However, as it was already mentioned, if we want to include random events in our calculation, we have to apply density matrix formalism.

$$\rho = \begin{bmatrix}c_g c_g^{\,*} & c_g c_e^{\,*} \\ c_e c_g^{\,*} & c_e c_e^{\,*}\end{bmatrix} = \begin{bmatrix}\rho_{gg} & \rho_{ge} \\ \rho_{eg} & \rho_{ee}\end{bmatrix}. \tag{2.63}$$

Elements of the Lindblad operator can be introduced easily and intuitively. We define decay rate from the excited state as Γ. Population decaying from the excited level will repopulate the ground level of an atom. Other decoherence mechanisms are included as presented in [128]:

$$L = \begin{bmatrix}\Gamma\rho_{ee} & -\frac{\Gamma}{2}\rho_{ge} \\ -\frac{\Gamma}{2}\rho_{eg} & -\Gamma\rho_{ee}\end{bmatrix}. \tag{2.64}$$

From the master equation (2.42) we obtain set of coupled differential equations governing the evolution of the system, so-called optical Bloch equations (OBEs):

$$\frac{d}{dt}\rho_{gg} = \frac{i\Omega}{2}\left(\tilde{\rho}_{ge} - \tilde{\rho}_{eg}\right) + \Gamma\rho_{ee}, \tag{2.65}$$

$$\frac{d}{dt}\rho_{ee} = -\frac{i\Omega}{2}\left(\tilde{\rho}_{ge} - \tilde{\rho}_{eg}\right) - \Gamma\rho_{ee}, \tag{2.66}$$

$$\frac{d}{dt}\rho_{eg} = -\frac{i\Omega}{2}\left(\rho_{gg} - \rho_{ee}\right) - \left(\frac{\Gamma}{2} - i\Delta\right)\tilde{\rho}_{eg}, \tag{2.67}$$

$$\frac{d}{dt}\rho_{ge} = \frac{i\Omega}{2}\left(\rho_{gg} - \rho_{ee}\right) - \left(\frac{\Gamma}{2} + i\Delta\right)\tilde{\rho}_{ge}. \tag{2.68}$$

With $\tilde{\rho}_{ge} = \rho_{ge}e^{-i\Delta t}$ and $\tilde{\rho}_{eg} = \rho_{eg}e^{-i\Delta t}$. The energy is conserved through the condition $\rho_{gg} + \rho_{ee} = 1$. In addition, off-diagonal elements of a density matrix are complex conjugate $\rho_{eg} = \rho_{ge}^{*}$. OBEs present one of the most commonly used tools in modelling the behaviour of optical quantum systems.

On the Figure 2.5 solutions of the OBEs are presented. The populations of the ground and excited states, and coherence are calculated for a Rabi frequency of $\Omega = 2\pi$ MHz, a detuning $\Delta = 0$. We can observe oscillatory behaviour due to Rabi oscillation at frequency $\Omega$. As a result of decay, eventually, density matrix elements reach so-called steady-state. Looking at the Figure 2.5, we can also come to the conclusion that transmission of the coupling light, described by the imaginary part of the coherence element, oscillates with Rabi frequency.

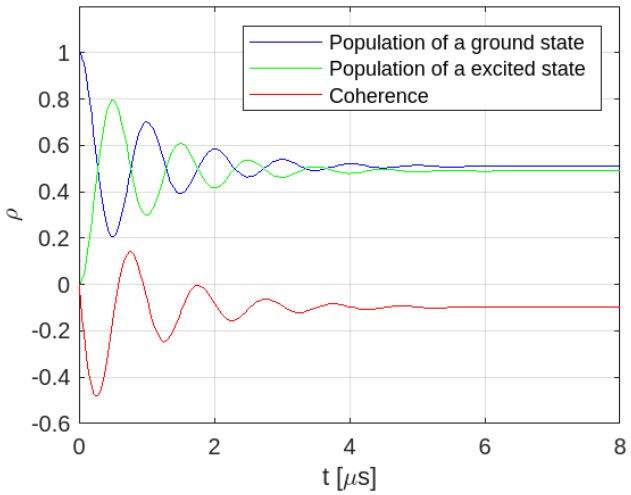


Figure 2.5 Transient solution for the states populations and the coherence, as a function of time.

In the simple cases, as this one, one can derive analytical solutions for the states populations and respective coherences making $\frac{d\rho}{dt} = 0$:

$$\rho_{gg} = \frac{\frac{\Omega^2}{4} + 4\left(\frac{\Gamma^2}{4} + \Delta^2\right)}{\Delta^2 + \frac{\Omega^2}{2} + \frac{\Gamma^2}{4}}. \tag{2.69}$$

$$\rho_{ee} = \frac{\frac{\Omega^2}{4}}{\Delta^2 + \frac{\Omega^2}{2} + \frac{\Gamma^2}{4}}, \tag{2.70}$$

$$\rho_{eg} = i\frac{\Omega\left(\frac{\Gamma^2}{4} + \Delta^2\right)}{\left(\frac{\Gamma}{2} + i\Delta\right)\left(\Omega^2 + \frac{\Gamma^2}{2} + 2\Delta^2\right)}. \tag{2.71}$$

On the Figure 2.6 the results for imaginary and real part of the $\rho_{eg}$ for a steady state solution are presented. Imaginary part gives us information on the absorption/transmission and we can notice it has a Lorentzian shape as a result of a homogeneous decay. Real part of the coherence is dispersion.

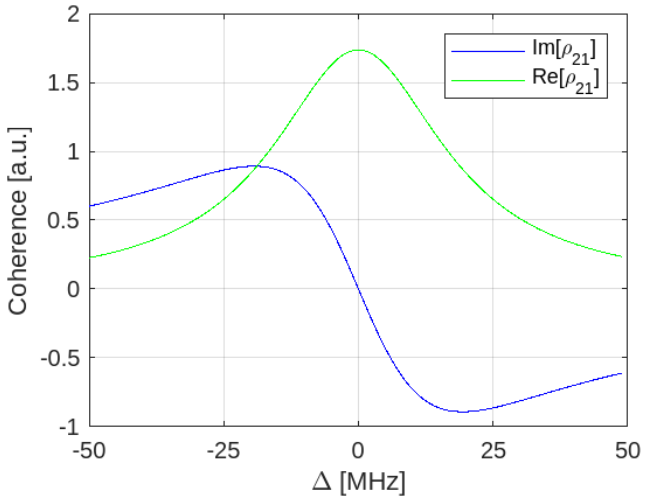

Figure 2.6 Real and imaginary part of the coherence as a function of detuning.

### 2.2.4. Three-level Λ system

Characteristic energy structure of alkali atoms enables the researches to realize experiments on different atomic scheme. For decades, special intention was directed to three-level schemes, like lambda, ladder and $V$ type energy structures. Probably, the mostly studied is Λ scheme. In this section, a short overview of such type of scheme is given. Extensively studied effect of electromagnetically induced transparency in alkali vapour is often realized on the three-level Λ scheme, such as one presented on the Figure 2.7. Again, we go back to the master equation (2.42). Now we have two electrical fields, coupling and probe, that interact with the atomic medium:

$$\boldsymbol{E}_c(t) = E_{c,0}\boldsymbol{e}cos(\omega_c t), \tag{2.72}$$

$$\boldsymbol{E}_p(t) = E_{p,0}\boldsymbol{e}cos\left(\omega_p t\right), \tag{2.73}$$

where coupling beam is acting between the levels $|2\rangle \rightarrow |3\rangle$, while probe beam couples levels $|1\rangle \rightarrow |3\rangle$ as depicted on the Figure 2.7.

For this system, density matrix operator has a following form:

$$\rho = \begin{bmatrix} \rho_{11} & \rho_{12} & \rho_{13} \\ \rho_{21} & \rho_{22} & \rho_{23} \\ \rho_{31} & \rho_{32} & \rho_{33} \end{bmatrix}. \tag{2.74}$$

As in the previous case, with two-level system, we need to define Hamiltonian $H$ of the system, and Lindblad operator $L$. The process is analogous to the one performed for the two-level system. The atomic Hamiltonian is:

$$H_0 = \hbar\omega_1|1\rangle\langle 1| + \hbar\omega_2|2\rangle\langle 2| + \hbar\omega_3|3\rangle\langle 3|. \tag{2.75}$$

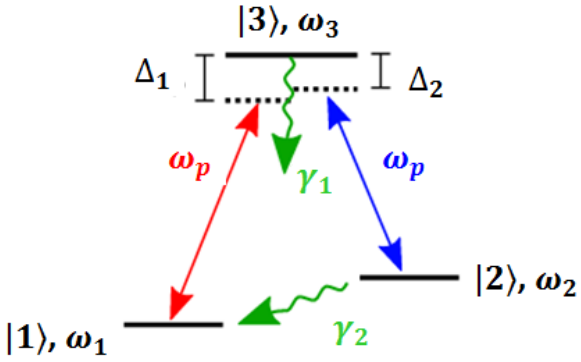


Figure 2.7 Energy scheme of a three-level Λ system.

while interaction Hamiltonian has the next form:

$$H_{int} = -\frac{\hbar}{2}\left(\Omega_p|3\rangle\langle 1|e^{i\Delta_1 t} + \Omega_c|3\rangle\langle 2|e^{i\Delta_2 t}\right). \tag{2.76}$$

Here, $\Delta_1 = \omega_p - \omega_3 + \omega_1$, $\Delta_2 = \omega_c - \omega_3 + \omega_2$, $\Omega_p = -\frac{E_p d_{13}}{\hbar}$ and $\Omega_c = -\frac{E_c d_{23}}{\hbar}$. The total Hamiltonian is then given by:

$$H = -\frac{\hbar}{2}\begin{bmatrix} 0 & 0 & \Omega_p \\ 0 & 2(\Omega_p - \Omega_c) & \Omega_c \\ \Omega_p & \Omega_c & 2\Omega_p \end{bmatrix}. \tag{2.77}$$

As a next step, we want to define the elements of the Lindblad operator, in order to include decay and dephasing effects. From the excited states, we have radiative, spontaneous decay Γ to two lower levels. In the radiative decay limit, nonradiative decoherences $\gamma_{ij}$ are equal to the half of radiative decays from respective state, $\gamma_{ij} = \frac{1}{2}(\gamma_i + \gamma_j)$. They also include the dephasing rates due to the collisions.

Finally, one can obtain set of OBEs for Λ system:

$$\frac{d\tilde{\rho}_{11}}{dt} = \Gamma_2\rho_{22} + \Gamma_3\rho_{33} + \frac{i}{2}\Omega_p(\rho_{21} - \rho_{12}), \tag{2.78}$$

$$\frac{d\tilde{\rho}_{22}}{dt} = -\Gamma_2\rho_{22} - \frac{i}{2}\Omega_c(\rho_{21} - \rho_{12}), \tag{2.79}$$

$$\frac{d\tilde{\rho}_{33}}{dt} = -\Gamma_3\rho_{33} + \frac{i}{2}\Omega_c(\rho_{23} - \rho_{32}), \tag{2.80}$$

$$\frac{d\tilde{\rho}_{12}}{dt} = -\frac{i}{2}\Omega_c\tilde{\rho}_{13} + \frac{i}{2}\Omega_p\tilde{\rho}_{32} - \left(\gamma_{21} - i(\Delta_2 - \Delta_1)\right)\tilde{\rho}_{12}, \tag{2.81}$$

$$\frac{d\tilde{\rho}_{13}}{dt} = \frac{i}{2}\Omega_p(\tilde{\rho}_{33} - \tilde{\rho}_{11}) - \frac{i}{2}\Omega_c\tilde{\rho}_{12} - (\gamma_{31} + i\Delta_1)\tilde{\rho}_{13}, \tag{2.82}$$

$$\frac{d\tilde{\rho}_{23}}{dt} = \frac{i}{2}\Omega_c(\tilde{\rho}_{33} - \tilde{\rho}_{22}) - \frac{i}{2}\Omega_p\tilde{\rho}_{21} - (\gamma_{32} + i\Delta_2)\tilde{\rho}_{23}. \tag{2.83}$$

If we make an assumption of a strong coupling beam (weak-probe regime), atoms will be trapped in the state $|1\rangle$. Along this statement, we can write:

$$\tilde{\rho}_{11} \approx 1, \;\; \tilde{\rho}_{22} = \tilde{\rho}_{33} \approx 0.$$

Previous set of the equations can be further simplified to:

$$\frac{d\tilde{\rho}_{12}}{dt} = -\frac{i}{2}\Omega_c\tilde{\rho}_{13} - \big(\gamma_{21} - i(\Delta_2 - \Delta_1)\big)\tilde{\rho}_{12}, \tag{2.84}$$

$$\frac{d\tilde{\rho}_{13}}{dt} = -\frac{i}{2}\Omega_p - \frac{i}{2}\Omega_c\tilde{\rho}_{12} - (\gamma_{31} + i\Delta_1)\tilde{\rho}_{13}, \tag{2.85}$$

$$\frac{d\tilde{\rho}_{23}}{dt} = -\frac{i}{2}\Omega_p\tilde{\rho}_{21} - (\gamma_{32} + i\Delta_2)\tilde{\rho}_{23}. \tag{2.86}$$

For a steady state, we can obtain simple analytical solutions:

$$\tilde{\rho}_{12} = \frac{\Omega_c\Omega_p}{4(i\gamma_{21} + \Delta_2 - \Delta_1)(-i\gamma_{31} + \Delta_1) + {\Omega_c}^2}. \tag{2.87}$$

$$\tilde{\rho}_{13} = \frac{2\big(\gamma_{21} - i(\Delta_2 - \Delta_1)\big)\Omega_p}{4(\gamma_{31} + i\Delta_1)(-i\gamma_{21} - \Delta_2 + \Delta_1) - i{\Omega_c}^2}. \tag{2.88}$$

In Figure 2.8 we have plotted the absorption and the dispersion of the probe, as a function of a probe detuning $\Delta_1$, for $\Delta_2 = 0$, $\gamma_{21} = 0$, $\gamma_{31} = 3$ MHz and $\Omega_c = 10$ MHz. On the Figure 2.6, we have seen how these profiles look when only probe is applied, with Lorentzian profile of the absorption. However, when the coupling beam is introduced, a sharp dip in the absorption profile appears. This is a distinctive feature of EIT effect.

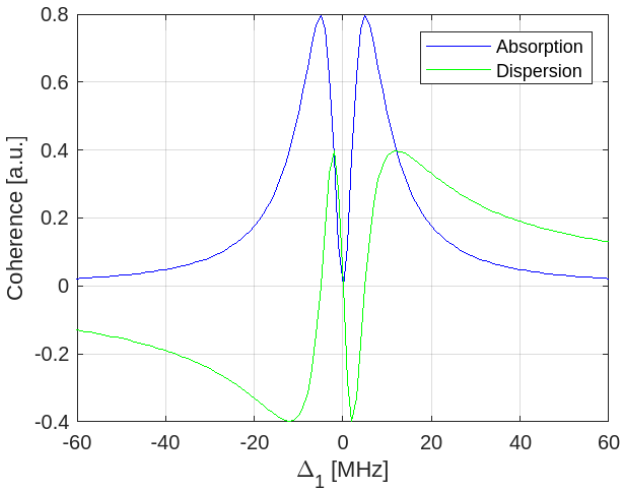


Figure 2.8 Absorption and dispersion a probe beam in EIT three-level Λ scheme.

# 3. Four-Wave Mixing as a Phase-Insensitive Amplifier – experiment and semi-classical description

In this chapter we present both experimental and theoretical study of nonlinear effects of Four Wave Mixing (FWM) in hot potassium vapour. We have demonstrated and studied the conditions of the system, when it behaves as a phase-insensitive amplifier.

We start by introducing nonlinear effects as a basis for understanding the special photon-light interaction when strong pump and weak (seed) probe beams interact with alkali atoms contained in alkali vapour. A description of a FWM effect on a double lambda scheme in K follows. In the next section, we have modified the set of optical Bloch equations, derived in the previous chapter for a three-level lambda scheme, by adding one more level, for the better description of a new system behaviour. This was a backbone of the theoretical study that followed. Non-perturbative numerical calculations of optical Maxwell-Bloch equations have been performed for a double-lambda system in potassium, in order to derive the atomic polarization and then amplitudes of electric fields of propagating electromagnetic waves, the pump and the twin beams - probe and conjugate, as the products of FWM. To the best of our knowledge this is the first and only fully numerical model developed and implemented for this type of the study. We have focused special intention to the discussion of a relevance (and inclusion) of Doppler effect on the obtained results.

Another section of this chapter is dedicated to the description of experimental setup, used for this study. Description of important instrumentation and optical elements, and their roles in the experiment, are given.

Finally, we presented the obtained experimental and theoretical results, compare them and discuss their agreement. In order to get a deeper insight into the studied effect, we performed comprehensive study of the results of gains of twin beams under a large span of FWM parameter. This highlighted the complexity of the studied system, but also gave us a basis and motivation to extend our study to the usage of FWM in K as a potential source of relative intensity squeezed light.

## 3.1. Nonlinear optics

An optical field, incident on a dielectric medium, induces a dipole moment and polarizes the material. In that case we can define the induced polarization of a system as a dipole moment per unit volume. Usually, for the isotropic mediums, it is linear, and can be calculated from [48]:

$$P = \varepsilon_0 \chi E, \tag{3.1}$$

where $\epsilon_0$ is a permitivity of a free space, and E is the applied electric field. $\chi$ is the property of the dielectric medium, called the susceptibility. This induced polarization results in the newly generated light that, in addition, can interfere with the incident light. This interaction is described by the Eq. (2.32), derived in the Chapter 2, that describes the behaviour of electromagnetic field.

The first order susceptibility is related to the index of refraction of a medium and its absorption as:

$$n = \sqrt{1 + Re(\chi)}, \tag{3.2}$$

$$\alpha = Im\,(\chi). \tag{3.3}$$

However, in research work, we are mainly interested in the nonlinear effects. They are a result of the higher order terms in the Taylor expansion of the optical polarization. For certain materials, and for sufficiently strong optical fields, the higher orders of optical susceptibility, i.e. polarization, appears and become relevant, and we can write [48]:

$$P = \varepsilon_0\left[\chi^{(1)} + \chi^{(2)}E + \chi^{(3)}E^2 + \cdots\right]E = \varepsilon_0\chi^{(1)}E + \left[\varepsilon_0\chi^{(2)}E^2 + \varepsilon_0\chi^{(3)}E^3\right] = P_L + P_{NL}, \tag{3.4}$$

where $\chi^{(n)}$ is the dielectric susceptibility tensor of n-th order. It is dimensionless and dependent on the material parameters. The nonlinear components of the polarization contribute to a variety of nonlinear processes, generating light at new frequencies.

In general, for a majority of media, the susceptibility becomes increasingly small with increasing order, and, hence, negligible at low and moderate amplitude (intensity) of interacting fields. In order for these higher orders to be comparable to the first order nonlinearity, as already mentioned, high field intensities are necessary. In some cases, in crystals that are lacking inversion symmetry, second order nonlinearity, $\chi^{(2)}$ becomes relevant and second order polarization component becomes:

$$P_{NL} = \varepsilon_0\chi^{(2)}E^2. \tag{3.5}$$

Let us consider the interaction with a second order nonlinear material with the total electrical field presented with:

$$E = E_1\cos(k_1z - \omega_1t + \varphi_1) + E_2\cos(k_2z - \omega_2t + \varphi_2). \tag{3.6}$$

Substituting Eq. (3.6) in Eq. (3.5), we can obtain the following term describing the nonlinear polarization [48]:

$$\begin{aligned} P_{NL} = \varepsilon_0\chi^{(2)}E^2 \quad &= \varepsilon_0\chi^{(2)}\begin{pmatrix} {E_1}^2\cos^2(k_1z - \omega_1t + \varphi_1) + {E_2}^2\cos^2(k_2z - \omega_2t + \varphi_2) \\ +2E_1E_2\cos(k_1z - \omega_1t + \varphi_1)\cos(k_2z - \omega_2t + \varphi_2) \end{pmatrix} \\ &= \varepsilon_0\chi^{(2)}\left(\frac{1}{2}{E_1}^2\cos\big((k_1z - \omega_1t + \varphi_1)\big)\right. \\ &+ \frac{1}{2}{E_2}^2\cos\big((k_2z - \omega_2t + \varphi_2)\big) \\ &+ E_1E_2\cos\big((k_1 + k_2)z - (\omega_1 + \omega_2)t + (\varphi_1 + \varphi_2)\big) \\ &+ E_1E_2\cos\big((k_1 - k_2)z - (\omega_1 - \omega_2)t \\ &\left.+ (\varphi_1 - \varphi_2)\big)\right). \end{aligned} \tag{3.7}$$

From Eq. (3.7), it is evident that new frequency components can be generated. With the newly obtained oscillating term at the sum of the frequencies, we are taking about the effect of the sum-frequency generation (SFG). On the other side, the process called difference-frequency generation (DFG) implies that the new frequency is generated at the difference of the input fields frequencies. There is also an additional field component, oscillating at $2\omega$. These media are said to support second order nonlinear effects (SHG), like parametric down conversion and frequency doubling effect [48]. Nonlinear crystals were common choice as a source for a generation of photon pairs, which found a wide range of applications, as we were introduced to in Chapter 1.

On the other hand, in the mediums which are centro-symmetric, like atomic vapour of interest in our work, even order susceptibility is zero . The generation of nonlinear effects is result of third-order nonlinearity, i.e. third-order polarization:

$$P_{NL} = \varepsilon_0 \chi^{(3)} E^3. \tag{3.8}$$

These effects are often called wave mixing processes. Some of the examples are – third harmonic generation, the intensity dependent index of refraction (Kerr effect), self-phase modulation and cross-phase modulation [48]. One of the alternative approaches to generate previously mentioned photon pairs is third-order nonlinear effect, four-wave mixing. It can be generated in different mediums, like alkali atoms, silicon waveguides, and photonic crystal fibres.

In Figure 3.1, some of the nonlinear effects that are mostly used in research are schematically presented.

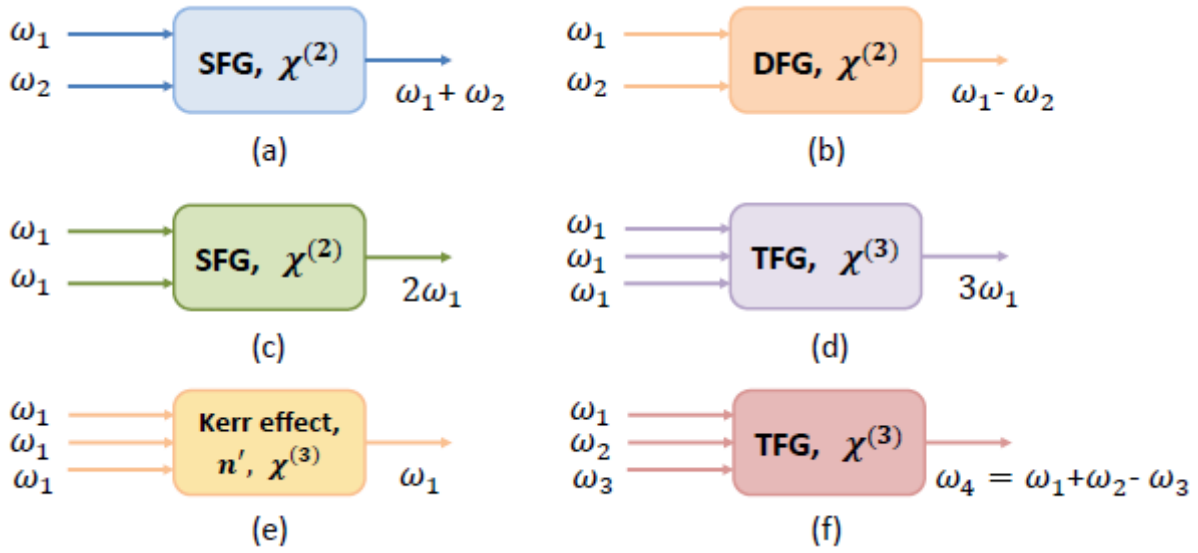


Figure 3.1 Schematic diagrams for second and third order nonlinear effects. (a) SFG; (b) DFG; (c) SHG; (d) THG; (e) Kerr effect; (f) FWM.

## 3.2. Four wave mixing in potassium vapour

Within this thesis, we are focused on the third order nonlinear effect called four-wave mixing in alkali atomic medium. This effect presents the interaction of three light fields within nonlinear medium, described with third order susceptibility, $\chi^{(3)}$. Characteristic of FWM is the interaction of two pump photons and a probe photon, carefully tuned to atomic transitions of alkali atom, that produces new photons at the frequency of the probe laser, and new photons at the new frequency. This fourth beam involved in the FWM is commonly called conjugate. Evidently, for the process to be efficient the pump beam ought to be very strong, The probe, also called seed beam, is week, orders of magnitude below the pump intensity. In addition to the generation of the beam at a new frequency, amplification of the probe and conjugate beams is also distinctive for this process.

This feature makes FWM specially interesting and perspective when it comes to its possible applications.

In general, there are two types of FWM processes – spontaneous and stimulated. When we discuss the spontaneous FWM, we consider the case when two pump photons produce two time correlated photons, probe and conjugate (or signal and idler) [129]. When there is a third, seed/probe beam at the input of the atomic medium, the process is considered to be stimulated, Figure 3.2. The latter one is in the focus of our study.

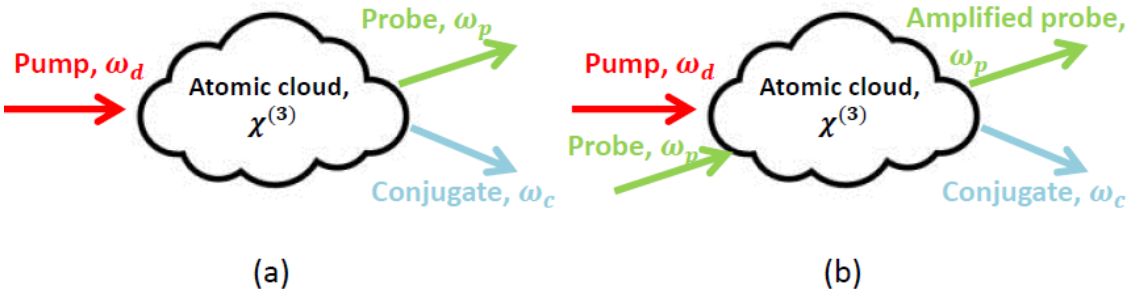


Figure 3.2 Schematic presentation of (a) spontaneous and (b) stimulated four-wave mixing process.

*Four Wave mixing in Potassium*

We study FWM that is realized on the D1 line of $^{39}$K [122], as presented in the Figure 3.3. The process involves four levels in a double Λ configuration, both hyperfine sublevels of the ground state and the sublevel of the excited state. Hyperfine levels in alkali atoms. of $4S_{1/2}$, $F = 1$ and $F = 2$ are noted as levels $|1\rangle$ and $|2\rangle$, respectively, while level $|3\rangle$ is $4P_{1/2}$, while with level $|4\rangle$ we define virtual detuned state, for the easier explanation and modelling of FWM. The hyperfine structure of the excited level is neglected compared to the ground state splitting.

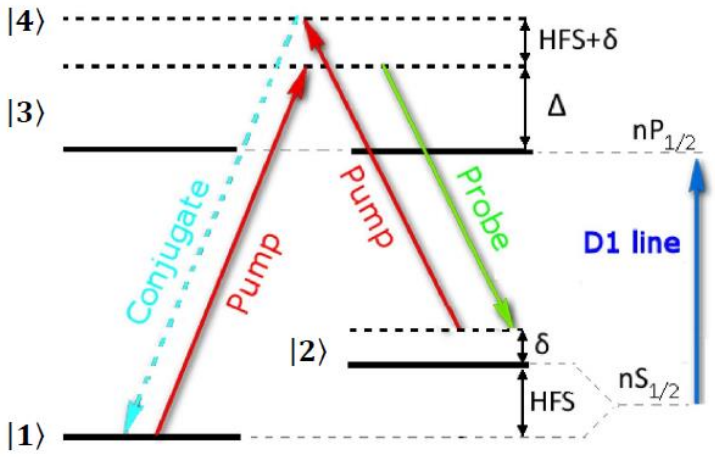


Figure 3.3 Four wave mixing using a double Λ scheme at $D_1$ line of potassium. HFS – hyperfine splitting, Δ – one-photon pump detuning, $\delta$ – two-photon probe detuning.

The lower lambda scheme consists of the pump photon that couples the level $|1\rangle$ to the level $|3\rangle$, with the one photon pump detuning Δ. The other leg of the first Λ scheme is the probe photon that stimulates Stokes scattering from the level $|3\rangle$ to the level $|2\rangle$, with two-photon probe detuning $\delta$. The pump is sufficiently strong to drive the off-resonant transition $|2\rangle \rightarrow |4\rangle$ in the upper Λ

scheme. By the way of stimulating anti-Stokes scattering, the conjugate photon closes the upper scheme. The total detuning of the level $|4\rangle$ is $\left(2\omega_d - \omega_p\right) - (\omega_4 - \omega_1)$, where $\omega_4 - \omega_1$ is angular frequency of the transition $|4\rangle \rightarrow |1\rangle$, while $\omega_d$ and $\omega_p$ are pump and probe frequencies, respectively. We introduce level $|4\rangle$, which is degenerate to the level $|3\rangle$, and like level $|3\rangle$, is weakly coupled to both level $|1\rangle$ and level $|2\rangle$ because of a large detuning.

*Phase-matching condition*

FWM is known to be a parametric process, which means that its final state, after the interaction, is the same as the initial one, before the process occurred. Alongside with this statement goes the following one - the energy and momentum have to be conserved.

Conservation of energy, that requires that energy of incident pump photons must be equal to the energy of output photons, probe and conjugate, (can be written in terms of pump, probe and conjugate frequencies as:) follows from:

$$2\omega_d = \omega_p + \omega_c, \tag{3.9}$$

where $\omega_d, \omega_p$ and $\omega_c$ are pump, probe and conjugate frequencies, respectively.

The momentum conservation is fulfilled through the phase matching condition [130,], described by:

$$2\boldsymbol{k}_d = \boldsymbol{k}_p + \boldsymbol{k}_c. \tag{3.10}$$

Here, $\boldsymbol{k}_d, \boldsymbol{k}_p$ and $\boldsymbol{k}_c$ are the wave vectors of the respective beams inside the medium. When propagation of the beams is collinear, as in Figure 3.4(a), this condition is fulfilled. However, spatial directions of the beams in the experimental conditions are usually as presented in Figure 3.4(b) and (c). When this is the case, as it was already noted by the others [131], a change of the refractive index for the probe beam has to be included, and the modification of a phase-matching condition is required, since, as demonstrated in Figure 3.4(b):

$$\Delta\boldsymbol{k} = 2\boldsymbol{k}_d - \boldsymbol{k}_2 + \boldsymbol{k}_3 \neq 0. \tag{3.11}$$

As it will be demonstrated in the following section, angle $\theta$ is one of the parameters of the system that has to be considered and adjusted for the optimal efficiency of the FWM process.

As a result of a described wave mixing inside the alkali vapour, when the strong pump beam and weaker probe are sent through the heated atomic cloud, in co-propagating direction with an angle $\theta$ relative to each other, we will observe amplified probe and newly generated conjugate beam on the opposite side, travelling at angle $2\theta$ with respect to each other, Figure 3.5.

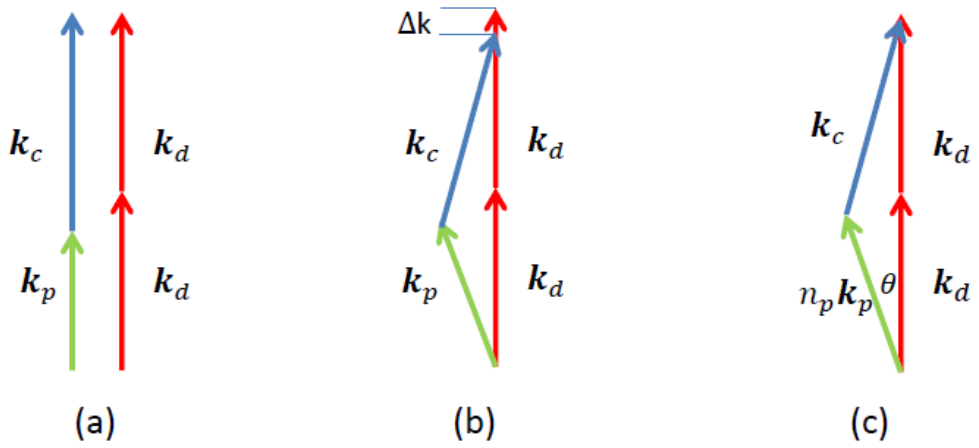


Figure 3.4 (a) Phase-matching condition in collinear beams configuration, (b) Phase mismatch - when probe is at angle $\theta$ relative to the pump direction, (3) Phase-matching condition is satisfied when the change of the index of refraction seen by the probe, $n_p$, is included.

*Analytical description of FWM process by the means of $\chi^{(3)}$ tensor elements*

Full analytical description of this process through calculations of respective susceptibilities, together with the use of propagation equations for predicting probe and conjugate behaviour, was previously developed [131] and implemented in the study of a different alkali specie. We have employed this approach for initial calculations and predictions, when we considered potassium as a potential medium for the efficient four wave mixing source.

The process of FWM is described with a system of equations [131,132]:

$$\frac{\partial}{\partial z}E_p = \frac{ik_p}{2\epsilon_0}P_p(\omega_p)e^{-i\boldsymbol{k}_p\cdot\boldsymbol{r}} \tag{3.12}$$

$$\frac{\partial}{\partial z}E_c = \frac{ik_c}{2\epsilon_0}P_c(\omega_c)e^{-i\boldsymbol{k}_c\cdot\boldsymbol{r}} \tag{3.13}$$

with

$$P_p(\omega_p) = \epsilon_0\chi_{pp}(\omega_p)E_p + \epsilon_0\chi_{pc}(\omega_p)E_c^{\dagger}e^{i\Delta\boldsymbol{k}\cdot\boldsymbol{r}} \tag{3.14}$$

$$P_c(\omega_c) = \epsilon_0\chi_{cc}(\omega_c)E_c + \epsilon_0\chi_{cp}(\omega_c)E_p^{\dagger}e^{i\Delta\boldsymbol{k}\cdot\boldsymbol{r}}. \tag{3.15}$$

Here $E_p$ and $E_c$ are probe and conjugate fields, respectively. Susceptibilities $\chi_{pp}$ and $\chi_{cc}$ are effective linear responses of the atomic medium to the probe and conjugate beams. As previously noted, they are related to the absorption and dispersion. Susceptibilities $\chi_{pc}$ and $\chi_{cp}$ are called cross terms, and are responsible for the cross-coupling FWM process. Assuming that the pump is undepleted in the vapour, and slowly varying electric field envelopes one can obtain following set:

$$\frac{\partial}{\partial z}E_p = \frac{ik_p}{2}\left(\chi_{pp}(\omega_p)E_p + \chi_{pc}(\omega_p)E_c^{*}e^{i\Delta\boldsymbol{k}\cdot\boldsymbol{r}}\right), \tag{3.16}$$

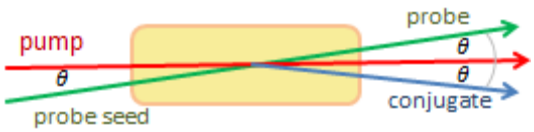


Figure 3.5 Simplified schematic of the FWM process for co-propragating pump and probe seed beams, crossing at the angle $\theta$ inside the alkali cell.

$$\frac{\partial}{\partial z}E_c = \frac{ik_c}{2}\left(\chi_{cc}(\omega_c)E_c + \chi_{cp}(\omega_c)E_p^* e^{i\Delta \boldsymbol{k}\cdot\boldsymbol{r}}\right). \tag{3.17}$$

Susceptibilities are calculated by:

$$\chi_{pp} = \frac{iN|d_{23}|^2\gamma_{41}^*}{\epsilon_0\hbar D^*}\left(\frac{\gamma_{21}^*}{\gamma_{42}^*}\sigma_{2,4} + \frac{\gamma_{43}^*}{\gamma_{31}^*}\sigma_{1,3} - \left(\frac{\gamma_{21}^* + \gamma_{43}^*}{\gamma_{41}^*} + \frac{4\gamma_{21}^*\gamma_{43}^*}{|\Omega|^2}\right)\sigma_{2,3}\right), \tag{3.18}$$

$$\chi_{cc} = \frac{iN|d_{14}|^2\gamma_{32}^*}{\epsilon_0\hbar D}\left(\frac{\gamma_{43}}{\gamma_{42}^*}\sigma_{2,4} + \frac{\gamma_{21}}{\gamma_{31}^*}\sigma_{1,3} - \left(\frac{\gamma_{21} + \gamma_{43}}{\gamma_{32}^*} + \frac{4\gamma_{21}\gamma_{43}}{|\Omega|^2}\right)\sigma_{1,4}\right), \tag{3.19}$$

$$\chi_{pc} = \frac{iNd_{14}d_{23}\Omega^2\gamma_{41}^*}{\epsilon_0\hbar D^*|\Omega|^2}\left(\frac{\gamma_{21}^*}{\gamma_{31}}\sigma_{1,3} + \frac{\gamma_{43}^*}{\gamma_{42}}\sigma_{2,4} + \left(\frac{\gamma_{21}^* + \gamma_{43}^*}{\gamma_{41}^*}\right)\sigma_{1,4}\right), \tag{3.20}$$

$$\chi_{cp} = \frac{iNd_{14}d_{23}\Omega^2\gamma_{32}^*}{\epsilon_0\hbar D|\Omega|^2}\left(\frac{\gamma_{43}}{\gamma_{31}}\sigma_{1,3} + \frac{\gamma_{21}}{\gamma_{42}}\sigma_{2,4} + \left(\frac{\gamma_{21} + \gamma_{43}}{\gamma_{32}^*}\right)\sigma_{2,4}\right), \tag{3.21}$$

where $N$ is the atomic density, $d_{ij}$ is atomic dipole moment for the transition $j \to i$, $\sigma_{ij}$ is the population difference between the levels $i$ and $j$, obtained by [131]:

$$\sigma_{1,3} = \sigma_{1,4} = \frac{|\gamma_{31}|^2}{|\Omega|^2 + |\gamma_{31}|^2 + |\gamma_{42}|^2}, \tag{3.22}$$

$$\sigma_{2,3} = \sigma_{2,4} = \frac{|\gamma_{42}|^2}{|\Omega|^2 + |\gamma_{31}|^2 + |\gamma_{42}|^2}, \tag{3.23}$$

and

$$D = (\gamma_{21} + \gamma_{43})(\gamma_{41} + \gamma_{32}^*) + \frac{4\gamma_{21}\gamma_{43}\gamma_{41}\gamma_{32}^*}{|\Omega|^2}. \tag{3.24}$$

In the previous equations $\Omega$ is the pump Rabi, $\gamma_{ij}$ are complex decay rates, which are for potassium D1 line, such on Figure 3.3, defined as:

$$\gamma_{43} = iHFS - \gamma, \tag{3.25}$$

$$\gamma_{42} = i(HSF + \Delta - \delta) - \gamma/2, \tag{3.26}$$

$$\gamma_{41} = i(HFS + \Delta) - \gamma/2, \tag{3.27}$$

$$\gamma_{32} = i(\Delta - \delta) - \gamma/2, \tag{3.28}$$

$$\gamma_{31} = i\Delta - \gamma/2, \tag{3.29}$$

$$\gamma_{21} = i\delta - \gamma_c. \tag{3.30}$$

with the spontaneous decay rate γ and ground state decoherence $\gamma_c$.

Finally, we are interested in the effectiveness of the FWM process, described by the amplification of the probe and conjugate beams. In order to determine the gain due to FWM process, one has to solve the propagation equations $(3.12 - 3.13)$. With the assumptions of weak probe beam at the input of the interaction medium, $E_{p,0}$, and no conjugate, $E_{c,0} = 0$, one can obtain following solutions [131]:

$$E_p(L) = E_{p,0}e^{AL}\left(\cosh(\zeta L) + \frac{B}{\zeta}\sinh(\zeta L)\right), \tag{3.31}$$

$$E_c^*(L) = E_{p,0}e^{AL}\frac{B_{cp}}{\zeta}\sinh(\zeta L). \tag{3.32}$$

Here, $L$ is the medium length, and

$$A = \frac{B_{pp} - B_{cc} + i\Delta k}{2}, \tag{3.33}$$

$$B = \frac{B_{pp} - B_{cc} - i\Delta k}{2}, \tag{3.34}$$

$$\zeta = \sqrt{-B_{pc}B_{cp} + B^2}, \tag{3.35}$$

$$B_{pi} = \frac{i\chi_{pi}k_p}{2}, \quad i = p, c, \tag{3.36}$$

$$B_{ci} = \frac{i\chi_{ci}^*k_c}{2}, \quad i = p, c, \tag{3.37}$$

with

$$\Delta k = 2k_d - n_p k_p \cos\theta - k_c \sin\theta, \tag{3.38}$$

which follows from the geometric configuration as presented on the Figure 3.4(a), for $n_p = \sqrt{1 + Re(\chi_{pp})}$.

Now, gains of the probe and conjugate can be calculated by:

$$G_p = \frac{\left|E_p(L)\right|^2}{E_{p,0}^2}, \tag{3.39}$$

$$G_c = \frac{|E_c(L)|^2}{E_{p,0}^2}. \tag{3.40}$$

## 3.3. Maxwell-Bloch equations for double-$\Lambda$ system

Theoretical study, complementary with the experiment, gives us an additional tool for gaining deeper understanding of phenomena of interest. In addition, when studying effect like four-wave mixing, where there are multiple parameters whose values can be varied in a wide span of values, theoretical model could significantly ease the search for optimal system parameters. Following the theoretical descriptions of two- and three- level system in Chapter 2, we now turn to the analysis and discussions of a atomic system that employs four energy levels in double-Λ configuration, as the on described in previous section.

There are different theoretical studies on FWM that were published, for degenerate and counter-propagating beams [133], as well for non-degenerate in co-propagating configuration [131,132]. In the later, nonlinear parametric processes in FWM were studied in a double Λ configuration, either with resonant (larger contribution from CPT and EIT phenomena) [132] or off-resonant pump frequency [132], in hot gas vapours or in cold atoms [133]. There are different approaches to model complex processes in FWM. They depend on the intended applications of the system, which can be parametric gain, quantum-correlations of twin beams, squeezing and entanglement, slow and stored light, i.e. whether classical or quantum properties are of interest. For work presented in this part of the thesis, most relevant are models that analyse CW regime and calculate gains of twin beams. In most models, the treatment is based on analytical solutions, after perturbation theory and number of approximations being applied [133,134]. In the seminal paper [132], pump and probe are resonant with atomic transitions with conditions for EIT, while cross susceptibilities are enhanced by coherence in the ground hyperfine levels. Within our work, we have developed nonperturbative, numerical model based on optical Maxwell-Bloch equations [65]. With the use of optical Bloch equations, we were able to calculate atomic polarization, and then applied the obtained results in the propagation equations to get the results for the amplitudes of the propagating fields of pump, probe and conjugate.

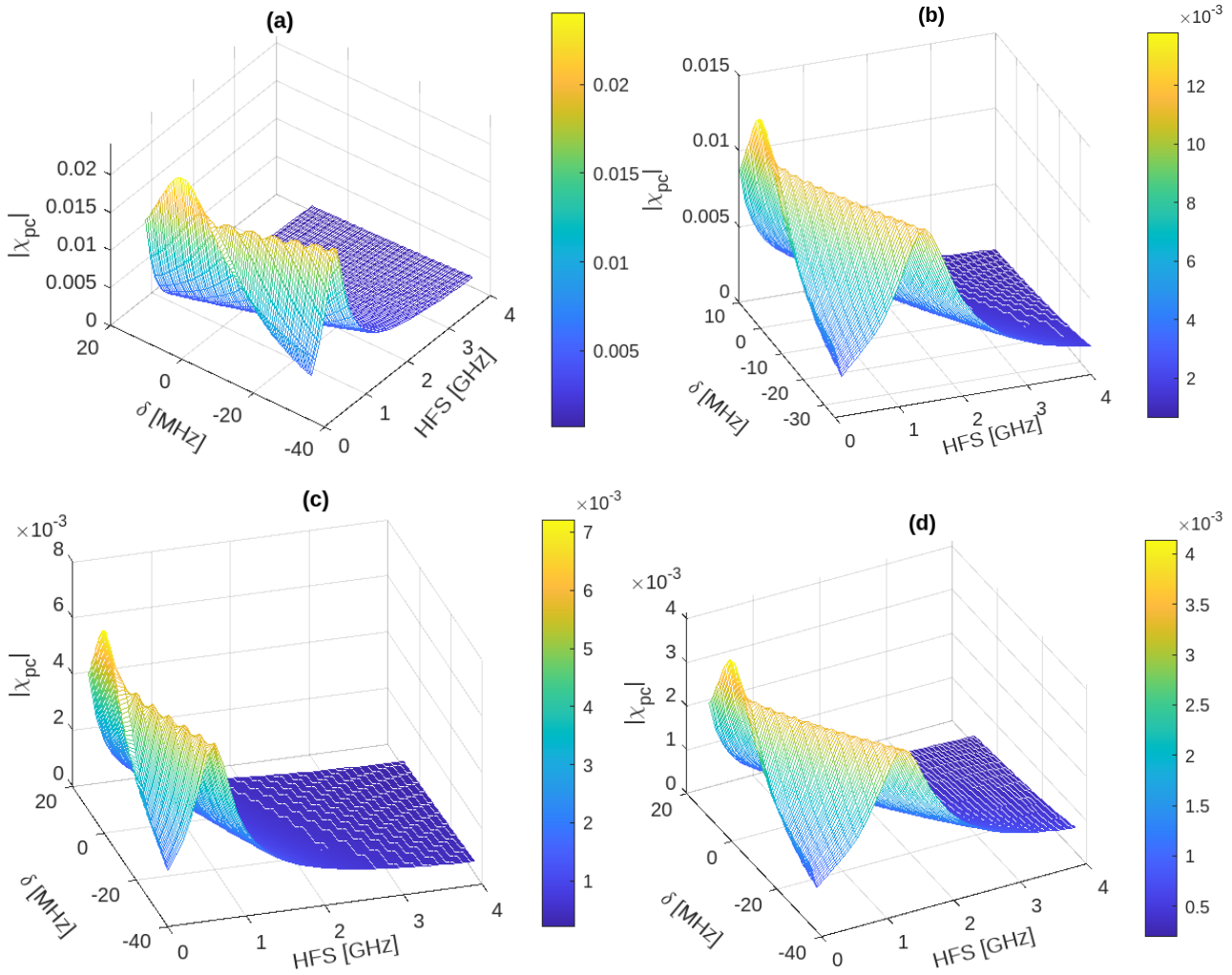


Figure 3.6 Calculated cross-susceptibilities for FWM process in Potassium. (a) (a),(b) $N = 3 \times 10^{12}$ cm$^{-3}$ (120 $^{o}$C) and Figure 3.6 (c),(d) $N = 1 \times 10^{13}$ cm$^{-3}$ (140 $^{o}$C). (a),(c) $\Delta$= 0.7 GHz and (b),(d) $\Delta$= 1 GHz. $\gamma = 6$ MHz, $\gamma_c = 1.2$ MHz.

We follow the same procedure, as described in Chapter 2, to arrive to the desired set of equations. We want to solve wave propagating Equation (2.32).

$$\nabla^2 E - \frac{1}{c^2}\frac{\partial^2 E}{\partial t^2} = \mu_0 \frac{\partial^2 P}{\partial t^2}. \tag{3.41}$$

Atoms are simultaneously illuminated by the pump, probe and conjugate. Hence, they experience total electrical field that can be approximated as a sum of three monochromatic fields:

$$\boldsymbol{E} = \sum_{i=d,p,c} \boldsymbol{e}_i E_i^{(+)} e^{-i\omega t + i\boldsymbol{k}_i \boldsymbol{r}} + c.c. \tag{3.42}$$

Here, $\boldsymbol{e}_i$ is polarizing vector, $E_i^{(+)}$ are slowly varying approximations of the fields amplitudes, with positive frequencies. We can also define a polarization in a similar form:

$$\boldsymbol{P} = \boldsymbol{e}_i P_i^{(+)} e^{-i\omega t + i\boldsymbol{k}_i \boldsymbol{r}} + c.c. \tag{3.43}$$

with the assumption of SVA, we have:

$$\left|k_i E_i^{(+)}\right| \gg \left|\frac{\partial E_i^{(+)}}{\partial z}\right|, \tag{3.44}$$

$$\left|\omega_i E_i^{(+)}\right| \gg \left|\frac{\partial E_i^{(+)}}{\partial t}\right|. \tag{3.45}$$

After substituting (3.42) and (3.43) into Equation (3.41), we obtain the following form for the equation of propagation:

$$\frac{\partial E_i^{(+)}}{\partial z} + \frac{1}{c}\frac{\partial E_i^{(+)}}{\partial t} = i\frac{k}{2\epsilon_0}P_i^{(+)}. \tag{3.46}$$

Next, we define the total Hamiltonian of the system presented on the Figure 3.3 as:

$$H = H_0 + H_{int} = \sum_{i=1}^{4} \hbar\omega_i |i\rangle\langle i| - \boldsymbol{d}\cdot\boldsymbol{E}(\boldsymbol{r},t). \tag{3.47}$$

Again, $H_0$ is unperturbed Hamiltonian of the system, $H_{int}$ is the interaction Hamiltonian, $\hbar\omega_i$ is the energy of level $|i\rangle$, and $\boldsymbol{d}$ is electric atomic dipole moment, with off-diagonal elements equal to zero for the forbidden dipole transitions.

Dynamics of the atoms is described with density matrix:

$$\hat{\rho} = \begin{bmatrix} \rho_{11} & \rho_{12} & \rho_{13} & \rho_{14} \\ \rho_{21} & \rho_{22} & \rho_{23} & \rho_{24} \\ \rho_{31} & \rho_{32} & \rho_{33} & \rho_{34} \\ \rho_{41} & \rho_{42} & \rho_{43} & \rho_{44} \end{bmatrix}. \tag{3.48}$$

Its behavior is governed by the set of optical Bloch equations:

$$\frac{\partial\hat{\rho}}{\partial t} = -\frac{i}{\hbar}[\hat{H},\hat{\rho}] + \hat{L} = -\frac{i}{\hbar}[\hat{H},\hat{\rho}] + \widehat{SE} + \hat{R}, \tag{3.49}$$

where the Lindblad operator is presented as the sum of two terms, of which the first $\widehat{SE}$ denotes the spontaneous emission from the excited states, and second $\hat{R}$ is the relaxation due to atom transit time induces losses and collisional dephasing. Their matrix forms are defined as follows:

$$\widehat{SE} = \begin{bmatrix} \Gamma_{1,3}\rho_{33} + \Gamma_{1,4}\rho_{44} & 0 & -\frac{\Gamma_{1,3}+\Gamma_{2,3}}{2}\rho_{13} & -\frac{\Gamma_{1,4}+\Gamma_{2,4}}{2}\rho_{14} \\ 0 & \Gamma_{2,3}\rho_{33} + \Gamma_{2,4}\rho_{44} & -\frac{\Gamma_{1,3}+\Gamma_{2,3}}{2}\rho_{23} & -\frac{\Gamma_{1,4}+\Gamma_{2,4}}{2}\rho_{24} \\ -\frac{\Gamma_{1,3}+\Gamma_{2,3}}{2}\rho_{31} & -\frac{\Gamma_{1,3}+\Gamma_{2,3}}{2}\rho_{32} & -\Gamma_{1,3}\rho_{33} + \Gamma_{2,3}\rho_{33} & -\frac{\Gamma_{1,3}+\Gamma_{2,3}+\Gamma_{1,4}+\Gamma_{2,4}}{2}\rho_{34} \\ -\frac{\Gamma_{1,4}+\Gamma_{2,4}}{2}\rho_{41} & -\frac{\Gamma_{1,4}+\Gamma_{2,4}}{2}\rho_{42} & -\frac{\Gamma_{1,3}+\Gamma_{2,3}+\Gamma_{1,4}+\Gamma_{2,4}}{2}\rho_{43} & -\Gamma_{1,4}\rho_{44} - \Gamma_{2,4}\rho_{44} \end{bmatrix}, \tag{3.50}$$

$$\hat{R} = -\gamma\left[\hat{\rho} - \mathrm{diag}\left(\frac{1}{2}, \frac{1}{2}, 0, 0\right)\right] - \gamma_{deph}[\hat{\rho} - \mathrm{diag}(\rho_{11}, \rho_{22}, \rho_{33}, \rho_{44})]. \quad (3.51)$$

Here, $\Gamma_{i,j}$ is the decay rate from level $|j\rangle$ to level $|i\rangle$, with $\Gamma_i = \Gamma_{i,1} + \Gamma_{i,2}$. $\gamma$ is spontaneous decay from the excited state and $\gamma_{deph}$ is dephasing decay rate.

After substituting Equation (3.47) into Equation (3.49), we obtain fast oscillating terms in $\rho_{ij}$, due to fast oscillating terms in laser fields description. Then, we can make a substitution:

$$\tilde{\rho}_{ij} = \rho_{ij} e^{-i(\omega_{ij} t - \boldsymbol{k}_{ij}\boldsymbol{r})}, \quad (3.52)$$

where $\omega_{ij}$ are angular frequencies defined as: $\omega_{13} = \omega_{24} = \omega_d$, $\omega_{23} = \omega_p$, $\omega_{14} = \omega_c$, $\omega_{12} = \omega_{13} - \omega_{23}$, $\omega_{34} = \omega_{14} - \omega_{13,}$ and $\omega_{ij} = -\omega_{ji}$. $\boldsymbol{k}_{ij}$ are sums and differences of respective wave vectors: $\boldsymbol{k}_{13} = \boldsymbol{k}_{24} = \boldsymbol{k}_d$, $\boldsymbol{k}_{23} = \boldsymbol{k}_p$, $\boldsymbol{k}_{14} = \boldsymbol{k}_c$, $\boldsymbol{k}_{12} = \boldsymbol{k}_{13} - \boldsymbol{k}_{23}$, $\boldsymbol{k}_{34} = \boldsymbol{k}_{14} - \boldsymbol{k}_{13,}$ and $\boldsymbol{k}_{ij} = -\boldsymbol{k}_{ji}$. In order to simplify the obtained equations, one can apply rotating wave approximation to get rid of the terms that oscillate at the sum of the frequencies. Resulting system of Bloch equations are now time-independent, with some spatially dependent terms oscillating with $e^{i\Delta kz}$, where $\Delta\boldsymbol{k} = 2\boldsymbol{k}_d - \boldsymbol{k}_p - \boldsymbol{k}_c$.

Now, we get the set of OBEs for double $\Lambda$ system:

$$\frac{d\rho_{11}}{dt} = \gamma\left(\frac{1}{2} - \rho_{11}\right) + \Gamma_{1,3}\rho_{33} + \Gamma_{1,4}\rho_{44} + \frac{i}{\hbar}\left(E_d^{(+)*} d\rho_{31} - E_d^{(+)} d\rho_{13} + E_c^{(+)*} d\rho_{41} - E_c^{(+)} d\rho_{14}\right),$$

$$\frac{d\rho_{22}}{dt} = \gamma\left(\frac{1}{2} - \rho_{22}\right) + \Gamma_{2,3}\rho_{33} + \Gamma_{2,4}\rho_{44} + \frac{i}{\hbar}\left(E_d^{(+)*} d\rho_{32} - E_d^{(+)} d\rho_{23} + E_c^{(+)*} d\rho_{42} - E_c^{(+)} d\rho_{24}\right),$$

$$\frac{d\rho_{33}}{dt} = -\gamma\rho_{33} + \Gamma_3\rho_{33} + \frac{i}{\hbar}\left(E_d^{(+)} d\rho_{13} - E_d^{(+)*} d\rho_{31} + E_p^{(+)} d\rho_{23} - E_p^{(+)*} d\rho_{32}\right),$$

$$\frac{d\rho_{44}}{dt} = -\gamma\rho_{44} + \Gamma_4\rho_{44} + \frac{i}{\hbar}\left(E_c^{(+)} d\rho_{14} - E_c^{(+)*} d\rho_{41} + E_d^{(+)} d\rho_{24} - E_d^{(+)*} d\rho_{42}\right),$$

$$\frac{d\rho_{12}}{dt} = -(\gamma + \gamma_{deph} + i\delta)\rho_{12} + \frac{i}{\hbar}\left(E_d^{(+)*} d\rho_{32} - e^{i\Delta kz} E_d^{(+)} d\rho_{14} + e^{i\Delta kz} E_c^{(+)*} d\rho_{42} - E_p^{(+)} d\rho_{13}\right),$$

$$\frac{d\rho_{13}}{dt} = -\left(\gamma + \gamma_{deph} + \frac{\Gamma_3}{2} + i\Delta\right)\rho_{13} + \frac{i}{\hbar}\left(E_d^{(+)*} d\rho_{33} - E_d^{(+)*} d\rho_{11} + E_c^{(+)*} d\rho_{43} - E_p^{(+)*} d\rho_{12}\right),$$

$$\frac{d\rho_{14}}{dt} = -\left(\gamma + \gamma_{deph} + \frac{\Gamma_4}{2} + i(HFS + \Delta)\right)\rho_{14} + \frac{i}{\hbar}\left(E_d^{(+)*} d\rho_{34} - e^{-i\Delta kz} E_d^{(+)*} d\rho_{12} + E_c^{(+)*} d\rho_{44} - E_c^{(+)*} d\rho_{11}\right),$$

$$\frac{d\rho_{23}}{dt} = -\left(\gamma + \gamma_{deph} + \frac{\Gamma_3}{2} + i\Delta\right)\rho_{23} + \frac{i}{\hbar}\left(E_p^{(+)*} d\rho_{33} - E_d^{(+)*} d\rho_{21} + e^{-i\Delta kz} E_d^{(+)*} d\rho_{43} - E_c^{(+)*} d\rho_{22}\right),$$

$$\frac{d\rho_{24}}{dt} = -\left(\gamma + \gamma_{deph} + \frac{\Gamma_4}{2} + i(HFS + \Delta)\right)\rho_{24} + \frac{i}{\hbar}\left(E_d^{(+)*} d\rho_{44} - E_d^{(+)*} d\rho_{22} + e^{i\Delta kz} E_p^{(+)*} d\rho_{34} - e^{i\Delta kz} E_c^{(+)*} d\rho_{11}\right),$$

$$\frac{d\rho_{34}}{dt} = -\left(\gamma + \gamma_{deph} + \frac{\Gamma_3}{2} + \frac{\Gamma_4}{2} + i(HFS + \Delta - \delta)\right)\rho_{34} + \frac{i}{\hbar}\left(E_d^{(+)} d\rho_{14} - e^{-i\Delta kz} E_d^{(+)*} d\rho_{32} + e^{i\Delta kz} E_p^{(+)} d\rho_{24} - E_c^{(+)*} d\rho_{31}\right),$$

$(3.53) - (3.62)$

We are interested in the ratio between the intensity of the probe we send to the medium and the intensity of the one leaving it, i.e. gain. In order to obtain this value, we calculate the propagation along the $z$ axis and temporal evolution of the beams interacting inside the vapor by the set of nonlinear equations for the slowly varying envelopes of these three fields:

$$\left(\frac{\partial}{\partial z} + \frac{1}{c}\frac{\partial}{\partial z}\right) E_d^{(+)} = i\frac{kN}{2\epsilon_0} d(\tilde{\rho}_{42} + \tilde{\rho}_{31}), \tag{3.63}$$

$$\left(\frac{\partial}{\partial z} + \frac{1}{c}\frac{\partial}{\partial z}\right) E_p^{(+)} = i\frac{kN}{2\epsilon_0} d\tilde{\rho}_{32}, \tag{3.64}$$

$$\left(\frac{\partial}{\partial z} + \frac{1}{c}\frac{\partial}{\partial z}\right) E_c^{(+)} = i\frac{kN}{2\epsilon_0} d\tilde{\rho}_{41}, \tag{3.65}$$

where $N$ is the atom density.

Our numerical model is without approximations needed for instance for analytical solutions, but its accuracy, i.e., agreement with the experiment depends on carefully chosen parameters, like the ones describing the dephasing mechanisms, types and corresponding values. In comparison with previous models for alkali atoms [131], we have included Doppler averaging and additional term that corresponds to the dephasing mechanisms that could be due to the atoms collisions or transit through the cross beam section. These additions make our model more appropriate for modelling hot atomic system and give us an additional tool to study influence of Doppler effect in such systems. In order to deal with Doppler averaging, we divide atoms in $n$ groups, with each having different $z$ component of the velocity $v_z$, for which Maxwell distribution is given by:

$$f(v_z) = \sqrt{\frac{m}{2\pi k_B T}} e^{-\frac{m v_z^2}{2k_B T}}. \tag{3.66}$$

Due to the Doppler effect, each of these groups differ by the effective detuning. For the group of atoms with the velocity $v_z$, observed angular frequency is:

$$\omega_0 = \sqrt{\frac{1-\beta}{1+\beta}}\,\omega_s, \tag{3.67}$$

where $\omega_s$ is the angular frequency of the source, and $\beta = v_z/c$. The frequency shift alters one photon detuning, $\Delta \rightarrow \Delta + \Delta_D$, which is consequently defined individually for each group of atoms, where Doppler shift is $\Delta_D = \omega_0 - \omega_s$. Two photon detuning remains the same, since the pump and probe are nearly copropagating. Since density matrix is dependent on $v_z$, in order to obtain the solutions, we have to solve $n$ sets of Bloch equations. In addition, propagation equations are also modified in the following way:

$$\left(\frac{\partial}{\partial z} + \frac{1}{c}\frac{\partial}{\partial z}\right) E_d^{(+)} = i\frac{kd}{2\epsilon_0}\sum_{v_z} N(v_z)\left(\tilde{\rho}_{42}(v_z) + \tilde{\rho}_{31}(v_z)\right), \tag{3.68}$$

$$\left(\frac{\partial}{\partial z} + \frac{1}{c}\frac{\partial}{\partial z}\right) E_p^{(+)} = i\frac{kd}{2\epsilon_0}\sum_{v_z} N(v_z)\tilde{\rho}_{32}(v_z), \tag{3.69}$$

$$\left(\frac{\partial}{\partial z} + \frac{1}{c}\frac{\partial}{\partial z}\right) E_c^{(+)} = i\frac{kd}{2\epsilon_0}\sum_{v_z} N(v_z)\,\tilde{\rho}_{41}(v_z). \tag{3.69}$$

Finally, we are able to calculate the gains of the probe and the conjugate from the ratio of the beams amplitudes at the exit from the vapour to the probe amplitude at the cell entrance.

## 3.4. Experimental set-up

In this section we describe our experimental setup, and give an overview of the main parts of the experiment and the components. A schematic of an experiment, we used in the study of FWM, is presented on the Figure 3.7. This setup was also used in previous research with potassium, done by our team [124]. As a light source, we use single high power, narrow line Ti:Sapphire laser (Coherent, MBR 110 [135]). In the experiment, it is split in two by a 90:10 beam splitter. Stronger beam is used as the pump, while the weaker fraction is acting as the probe beam. Probe is sent through two AOMs for the probe frequency detuning with respect to the pump frequency, summing two frequency offsets to the total that is close to HFS of the K ground state. To keep probe spatially stable during fine detuning, the second AOM had to be in a double pass. Thus, we vary two-photon detuning by changing the probe frequency. With the use of the AOMs, we are able to shift the frequency of the beam, but still preserve these two interacting beams coherently in phase. On the other hand, one-photon pump detuning is changed by tuning the pump, i.e. laser frequency. The pump beam is sent through a set of lenses, to obtain the pump diameter of 1.1 mm. The probe waist is set to be 0.75 mm inside the cell. Two beams are orthogonally polarized by the use of the lambda-half waveplates, and recombined on the polarizing beam cube before entering the cell. They enter the cell at the small angle $\theta$, which can be adjusted by changing the probe and pump directions with the two entrance steering mirrors, placed before the combining cube. With the pump beam redirected with another polarizing beam splitter behind the cell, two beams emerge - probe and the frequency up-shifted beam (conjugate). Both beams are detected with the pair of photodetectors. We get the gains of the probe and the conjugate from the ratios of measured powers of probe and conjugate beams behind the cell to the probe beam input power. Radius and shape of beams behind the cell are monitored with a CCD camera.

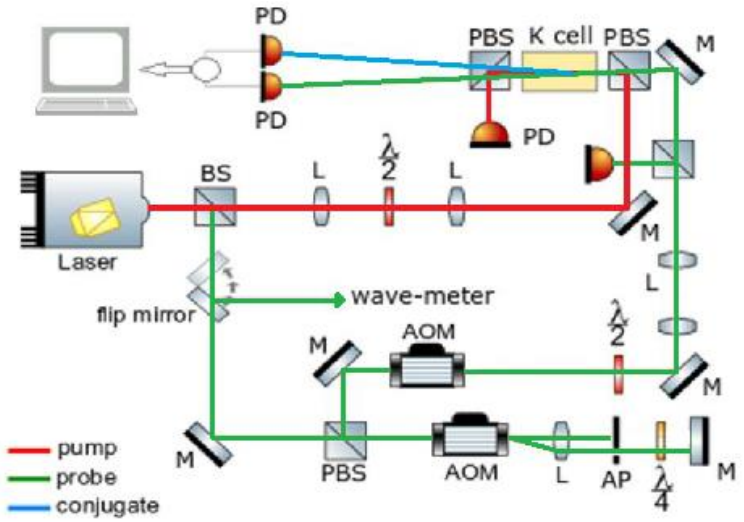


Figure 3.7 Scheme of the experimental setup for FWM, M - Mirror, L - Lens, PBS - Polarization beam splitter, AOM - Acousto-Optical Modulator, AP - Aperture, PD – Photodetector.

*Light source*

Single-frequency Ti:Sa MBR laser can be commonly found as a part of the experiments in quantum atomic physics in the laboratories all around the world. Depending on the power of the pump laser, it can produce up to the 1500 mW of the output power. Together with this high obtainable power, its broad tuning range, from 700 nm to 1000 nm, makes it a powerful experimental tool, especially compared to the diode lasers, which are often used. The schematic of the MBR, and its cavity are presented on the Figure 3.8. The active medium is a Titanium:Saphire crystal placed inside the ring bow-tie cavity, with Brewster cut front and back to minimise the reflection and support horizontally polarized light inside the cavity. The crystal holder is water cooled. The working wavelength is selected by rotating birefringent Lyot filter and intracavity thin etalon, which are indicated in the Figure 3.8. The etalon is mounted on a piezo controlled galvanometer that can be controlled by the MBR electronic box, being an additional way of stabilizing laser frequency and locking it to the desired one. As presented on the Figure, MBR comes with the external reference Fabry-Perot cavity. MBR design enables us to lock the laser cavity to this external stabilized reference cavity by feeding back to the signal to the tweeter mirror M3. In the described experimental setup, we have used VERDI V-5, as the pump source, which provide us with 5.5 W at 532 nm. With this pump, we were able to obtain a total of ~550 mW @ 770 nm.

*Frequency stabilization – laser locking*

As already stated in the Chapter 2, due to the Doppler broadening, hyperfine transitions at D1 line of K are not resolvable, even at the room temperature. However, there are different techniques that have been developed in order to overcome this issue. In our study we employ method called saturation absorption spectroscopy (SAS). Schematic of the setup we use for SAS is shown on a Figure 3.9(a). Two counter-propagating beams overlapping inside the cell are used. A small portion of the output laser power is sent to the cell as a pump beam. From the opposite direction, trough the cell is sent the another attenuated beam, called probe, which is used to measure the atomic saturation. The probe intensity is recorded by the photodetector. In this configuration, a standing wave is formed by the probe and pump, in which potassium atoms are moving. When the frequency

of the pump is resonant to one of the transitions, pump is being absorbed and it saturates the transition. As a result, the absorption of the probe is reduced in a narrow frequency range, which leads to the appearance of so called Lamb dips. In this manner, upon subtracting the Doppler background, we can obtain the saturation absorption spectrum as one shown on the Figure 3.9(b). With the resolved transitions, we are able to lock the laser to the desired one, providing frequency stabilization necessary for performing the further experimental studies. As one can observe, besides hyperfine transitions, other lines are presented in the measured spectrum. Namely, for the atoms with the zero velocity hyperfine transitions are obtained. However, due to other velocity groups, more dips appear. These are called cross-over resonances.

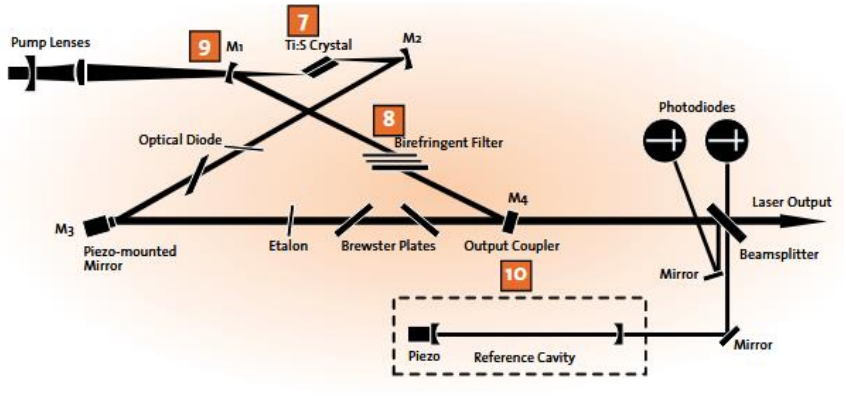


(a)

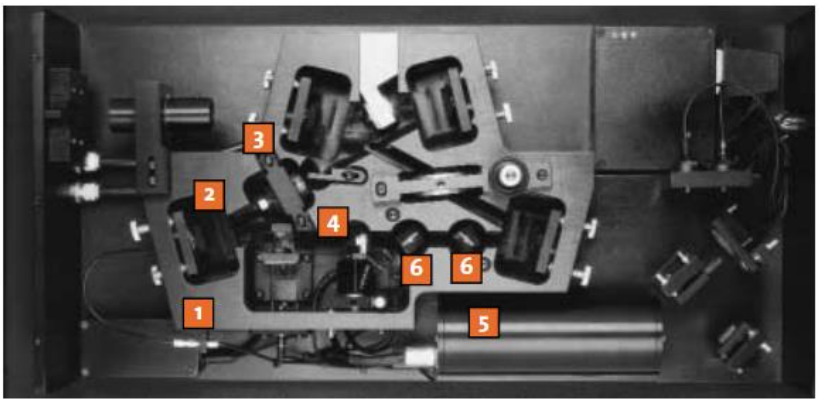


(b)

Figure 3.8. (a) Optics schematic of the MBR-110 Ti:Sapphire laser, and (b) the image of its optical cavity, with main components labelled: 1 – stable and robust monolithic resonator, 2 – piezo-mounted mirror that ensures a tight lock corresponding to a very narrow linewidth, 3 - miniature optical diode ensures unidirectional operation, 4 – thin etalon than ensured single-mode operation using servo-lock to eliminate mode-hops, 5 – high-finesse, temperature-controlled and sealed reference cavity used for the laser locking, achieving relative linewidths as low as 10 kHz, 6 – galvanometer-mounted tilting twin Brewster plates – enables scanning in excess of 40 GHz, 7 – Ti:Sapphire crystal provides a wide tuning range from 700 nm to 1000 nm, 8 – birefringent filter as a combination of three birefingent plates (Lyot filter) enables smooth tuning over a broad range, 9 – mirrors, 10 – output coupler. (*Figures and data are provided by Coherent [135])*

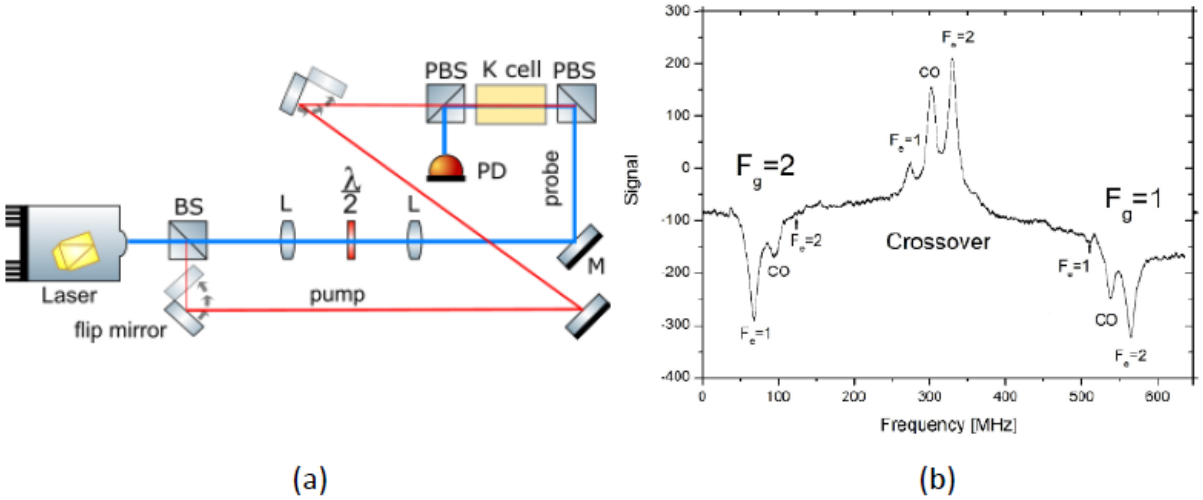


Figure 3.9. (a) Experimental schematic of SAS setup. (b) Measured transmission spectrum of the probe beam.

*Control of the probe detuning*

It was mention above that we use an AOM for control of the probe frequency. The acousto-optical modulators are devices which can be used for frequency, amplitude and phase light modulation. Its operation is based on diffraction of light passing through the crystal [136]. AOM consists of a crystal and a piezo electric transducer, as shown on a Figure 3.10(a). Its operation is based on the modulation induced by the change of the refractive index due to sound wave traveling through the crystal, created by the transducer. These changes in refractive index appear to form a kind of a Bragg grating. Hence, when light is passing through the crystal, it diffracts, with the $m^{th}$ order described by:

$$\sin\theta = \frac{m\lambda}{2\Lambda}. \tag{3.70}$$

Here, $\theta$ is the angle of diffraction, $\lambda$ is the wavelength of the light, and $\Lambda$ is the wavelength of the sound. The frequency shift, that we are interested in, is defined by:

$$\omega_m = \omega_0 + m\Omega_s, \tag{3.71}$$

where $\Omega_s$ is the frequency of the sound wave.

AOM is often use in a double-pass configuration [136], Figure 3.10(b). Special convenience of this arrangement is that beam propagation direction is not altered after passing twice through the AOM, compared to the beam we sent to the modulator. Hence, there is no need for the realignment of the setup after we change the probe frequency.

*Cell and the vapour heating system*

One of the most essential elements in the atomic physics experiments is the cell with a desired element. In this experiment we have used the vacuum K cell with natural abundance of isotopes, with no buffer gas. It is a cylindrical glass cell, 5 cm long, 25 mm in diameter, with Brewster's angled windows, shown in Figure 3.11

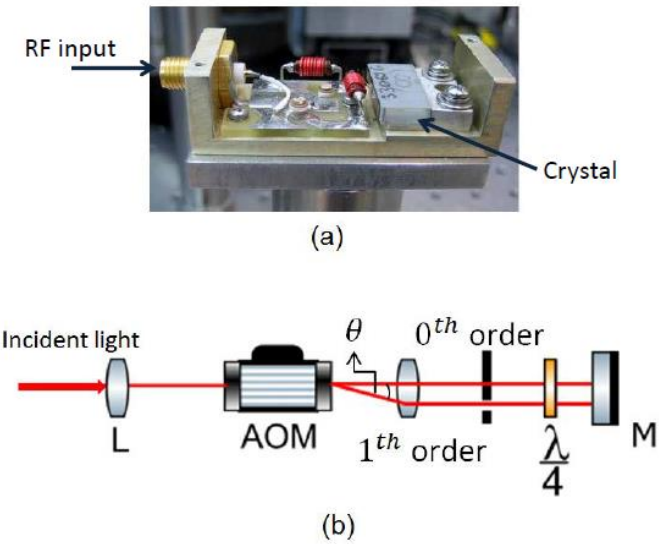


Figure 3.10 (a) Acousto-optical modulator used in the experiment. (b) Schematic of the AOM in double pass.

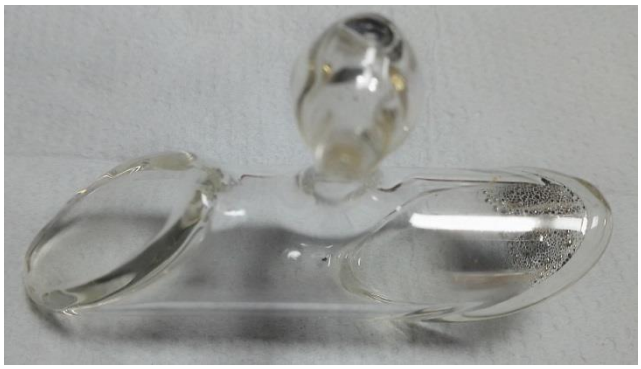

Figure 3.11. Potassium vapour cell used in the experiment studying classical gain of FWM.

The efficiency of four wave mixing process is highly dependent on the density of the atoms. Hence, it was necessary to build a stable heating system that could enable us to reach the desired operating temperatures of 100 – 150 $^{o}$C. We used home-made heating system, whose schematic is presented on the Figure 3.12(a). The cell is placed inside the aluminium cylinder, which is heated by the hot air. As can be seen in Figure 3.12(b) heated air is circulating through the cavities drilled inside the cylinder, and heats the aluminum in the process. Due to the heat transfer between the holder and the glass, with time our vapor is being vaporized. Two platinum resistance thermistors have been integrated in this system. One pt1000 sensor measures the temperature of the air right after the heater, and is used for the control of the current that is being sent to the heater, by the PID controller. Another pt1000 is glued with the thermal paste next to the cell. We have assumed that the temperature read at this spot is equal to the temperature of the vapor after a reasonable period of time. For the better thermal insulation, the aluminum block is placed inside the Teflon holder. With this heating system, we could heat up the cell up to 150 $^{o}$C, which corresponded to the vapour density of $1.75 \cdot 10^{13}$cm$^{-3}$. More details on this system one can find in [137].

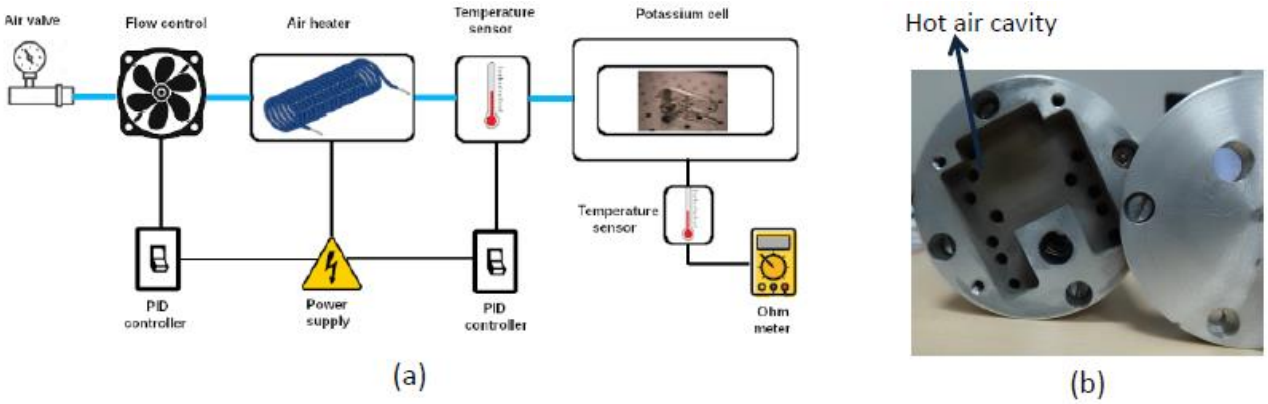


Figure 3.12 (a) Home-built heating system. (Picture taken from [137]) (b) Aluminum cell holder/heater, back-side view.

## 3.5. Results

Since experimental work previously done with the Rb [81] and Cs [110], on the topic of squeezing by FWM, together with the phenomenological theoretical model for two-mode relative intensity squeezing, as will be presented in Part II of this theses, indicated direct relation between the gain and the expected/measured squeezing, the step towards estimating FWM parameters for maximum squeezing was to first characterize our FWM system in terms of possible amplification of the probe and conjugate beams. In this section both theoretical and experimental results of the gains of the probe and conjugate are presented and discussed. We study dependence of FWM gain on different parameters of the system – the angle between the pump and the probe intersecting in the vapour cell, the cell temperature, the one-photon $\Delta$, and the two-photon detuning $\delta$, and the probe power. We also calculate how Doppler effect, and the transmission of the probe, which also important for the squeezing [81], affect FWM gain. .

The following results of the model are obtained with a few assumptions. One of which is that the pump and the probe are fully overlapped. Since, in the experiment, we use a cell which is 5 cm long, and the beams usually intersect at an angle of few mrad, they are only overlapped in the part of the cell. For this reason, when using the model, we set the interaction region length to be 1 cm. The value of the atom density, one- and two-photon detuning are the same as in the experiment. However, in the model, we also have some fitting parameters, like relaxation and dephasing rates, $\gamma$ and $\gamma_{deph}$. These mostly affect the amplitude of the gain profile, and, since they can't be determined experimentally, we choose their values from the range of values typically used in similar calculations [131] to obtain the best agreement with the experimentally measured gains. Rabi frequencies of the pump and the probe are calculated with the equation (2.52). One can notice the difference in the pump power set in the experiment, and the power, i.e. pump Rabi for which the calculated results in the following section are obtained. This discrepancy lies in the fact that the model assumes flat-top profile of the pump intensity, while in the experiment it is Gaussian. In order to mimic the experimental condition more accurately, we lower down the pump intensity i.e. pump Rabi value in the model.

*Dependence of the probe and conjugate gain with Doppler effect included*

As it was already mentioned, our motivation for this study of parametric gains by FWM in Potassium was a notion found in earlier papers on relation between gain, a classical property, and squeezing, a quantum property of FWM (as presented in the next Chapter. Also, it was found both experimentally and theoretically, in Rb and Cs [81,110], that for a good levels of squeezing it is necessary to reduce the probe absorption in the vapour cell and have similar and modest gains of both probe and conjugate.

It was found in works in Rb and Cs that relative intensity squeezing has maximum at the same value of the pump detuning where the probe gain has its maximum [81,110]. However, too large gain can result in amplification of probe seed noise noise. It was demonstrated for Rb and Cs, that typically the strongest squeezing is for Δ near the edge of the Doppler broaden line, when gains are at a maximum, and probe transmission at about 90% [81]. Hence, while exploring the parameters space for the optimal values, while testing our model, we were focused on obtaining such results for gains and probe transmission.

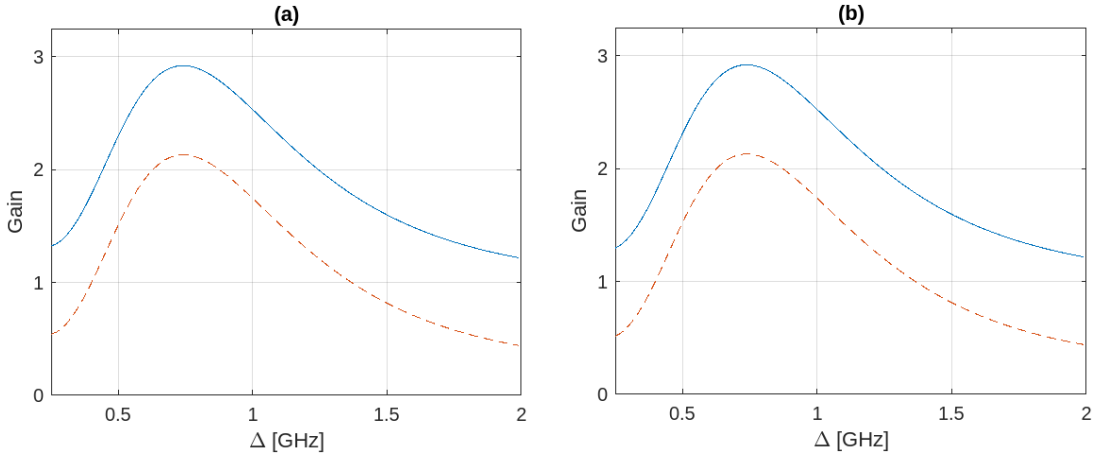


Figure 3.13 Calculated gains of the probe and conjugate as a function of one-photon detuning for different Doppler averaging. (a) $n = 3$, $\Delta_{D,1}= 0$, $\Delta_{D,2}= -0.25$ GHz, $\Delta_{D,3}= 0.25$ GHz, $N_1 = \frac{1.1}{3}N_c$, $N_2 = N_3 = \frac{0.9}{3}N_c$, (b) $n = 7$, $\Delta_{D,1}= 0$, $\Delta_{D,2}= -0.1$ GHz, $\Delta_{D,3}= 0.1$ GHz, $\Delta_{D,4}= -0.2$ GHz, $\Delta_{D,5}= 0.2$ GHz, $\Delta_{D,6}= -0.3$ GHz, $\Delta_{D,5}= 0.3$ GHz, $N_1 = \frac{1.2}{7}N_c$, $N_2 = N_3 = \frac{1.1}{7}N_c$, $N_4 = N_5 = \frac{0.975}{7}N_c$, $N_6 = N_7 = \frac{0.825}{7}N_c$. Other parameters in the calculus are $\Delta = 1$ GHz, $\delta = -0.5$ MHz, $N = 1 \times 10^{12}$ cm$^{-3}$, $\Omega_d = 1.95$ GHz, $\Omega_p = 22.5$ MHz, $\gamma = 5 \times 10^5$ Hz.

In our model, we have included the Doppler effect. However, inclusion of Doppler requires significant computational power for the modeling to be carried out. So, when making a choice on a number of atom velocity groups $n$, one has to find a compromise in order not to lose on the accuracy with a too low $n$, on the one hand, and making calculus too complicated with $n$ that is too high, on the other. Also, adjusting the frequency detuning between the different groups of the atoms, so as the atomic densities in respective atom groups, have to be carried out carefully. We have spent considerable amount of time testing our model with respect to these statements. Also, we were interested in which way the inclusion of Doppler will change the gains and probe transmission that our model predicts, compared to the ones when Doppler effect is neglected. At this stage of our study, we have tried to simplify the calculation with a smaller number $n$, while still obtaining good enough accuracy. On the Figure 3.13 we present the results for calculated probe and conjugate gains as a function of one-photon detuning, for different Doppler averaging, i.e. different number of atom groups. The results are obtained for (a) $n = 3$, with Doppler shifts $\Delta_{D,1}= 0$, $\Delta_{D,2}= -0.25$ GHz,

$\Delta_{D,3}$= 0.25 GHz, and respective atom densities $N_1 = \frac{1.1}{3}N_c$, $N_2 = N_3 = \frac{0.9}{3}N_c$, (b) $n = 7$, $\Delta_{D,1}$= 0, $\Delta_{D,2}$= −0.1 GHz, $\Delta_{D,3}$= 0.1 GHz, $\Delta_{D,4}$= −0.2 GHz, $\Delta_{D,5}$= 0.2 GHz, $\Delta_{D,6}$= −0.3 GHz, $\Delta_{D,5}$= 0.3 GHz, $N_1 = \frac{1.2}{7}N_c$, $N_2 = N_3 = \frac{1.1}{7}N_c$, $N_4 = N_5 = \frac{0.975}{7}N_c$, $N_6 = N_7 = \frac{0.825}{7}N_c$. Surprisingly, the differences in the obtained gain profiles are only slight.

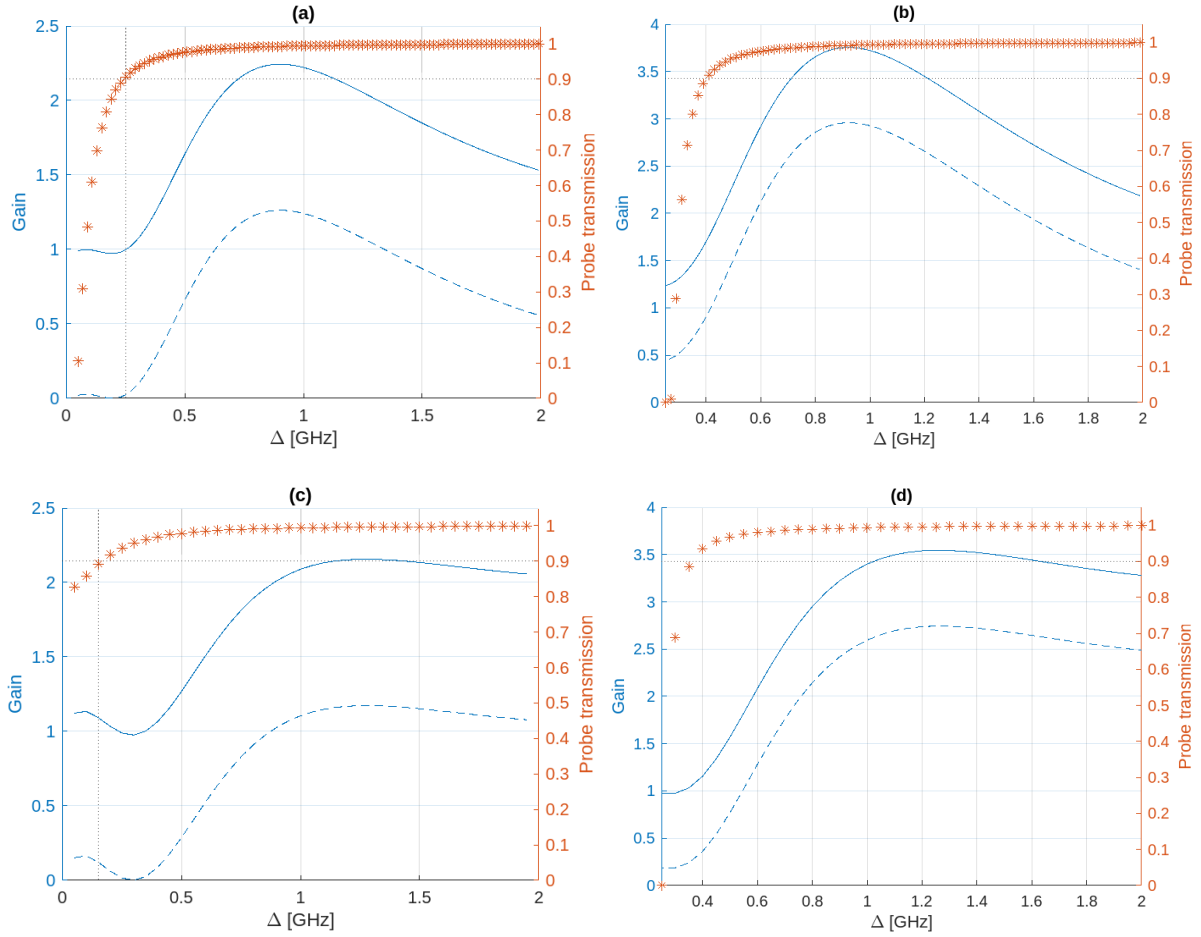


Figure 3.14 Calculated gains of the probe (blue dashed line) and the conjugate (blue thick line) and probe transmission versus one-photon detuning: (a),(c) without Doppler averaging; (b),(d) with Doppler averaging. (a),(c) $\delta = -0.5$ MHz, $N = 1 \times 10^{12}$ cm$^{-3}$, $\theta = 2.8$ mrad, $\gamma = 10^5$ Hz, $\gamma_{deph} = 0$. (b),(d) $\delta = -0.5$ MHz, $N = 1 \times 10^{12}$ cm$^{-3}$, $\theta = 1.8$ mrad, $\gamma = 10^3$ Hz, $\gamma_{deph} = 0$. $\Omega_d = 1.95$ GHz, $\Omega_p = 22.5$ MHz.

In the context of the previously mentioned experimental conditions desirable for obtaining squeezed light, we have performed thorough analysis in the search of system parameters that will give such gains and probe transmission in potassium. In Figure 3.14, results of the gains and transmission calculated for the two sets of parameters values, with and without Doppler averaging, are presented. In the first example, Figure 3.14 (a), $\delta = -0.5$ MHz, $N = 1 \times 10^{12}$ cm$^{-3}$, $\theta = 2.8$ mrad, $\gamma = 10^5$ Hz, $\gamma_{deph} = 0$. Results in Figure 3.14 (b) are obtained for different $\theta = 1.8$ mrad, and $\gamma = 10^3$ Hz. From these results, we gain an important insight into the requirements of the model that we employ to mimic the behavior of the FWM in potassium correctly. Namely, one can observe that in the case when Doppler broadening is neglected, the desired transmission of the probe is obtained even for the low Δ, at 250 MHz in case (a) and even lower 150 MHz in case (b). However, if one includes Doppler averaging, the transmission of 90% are obtained at higher one-photon detuning, above 500 MHz. Hence, when we turn to the quantum study of the light and

modeling of FWM in the context of the squeezing, we will have to go back to discussing and inclusion of the Doppler broadening in the modeling. At the point, since we are only interested in the gain profile, we choose to neglect the Doppler in the results to follow.

In the published works with both Rb [81] and Cs [110], good level of squeezing are often measured for positive values of two-photon probe detuning and temperatures around 110 $^{o}$C. With our model we were able to confirm that moderate and similar levels of the gains of the probe and conjugate can be obtained for atom density $N = 1.5 \times 10^{12}$ cm$^{-3}$ (110 $^{o}$C) and $\delta = 2$ MHz. According to these predictions, it should be possible to generate squeezed light in potassium for $\Delta \approx 0.7$ GHz, for this set of experimental parameters. This gives us a starting point for the further studies.

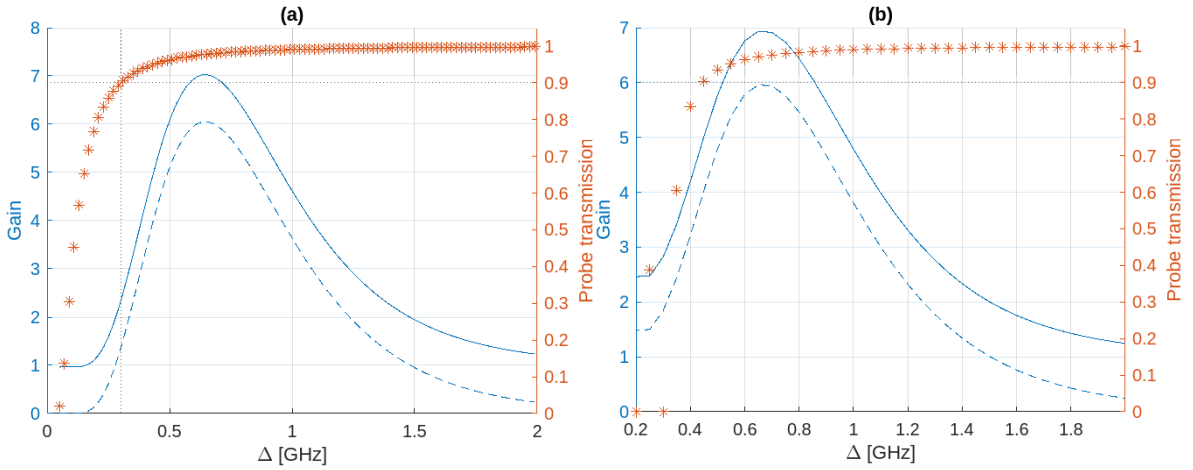


Figure 3.15 Calculated gains of the probe (blue dashed line) and the conjugate (blue thick line) and probe transmission versus one-photon detuning: (a) without Doppler averaging; (b) with Doppler averaging. $\delta = 2$ MHz, $N = 1.5 \times 10^{12}$ cm$^{-3}$, $\theta = 6$ mrad, $\gamma = 10^5$ Hz, $\gamma_{deph} = 0$, $\Omega_d = 1.95$ GHz, $\Omega_p = 22.5$ MHz.

*Dependence of gains on the angle between the pump and the probe*

The importance of the phase-matching was already pointed out. It is directly related to the angle between the pump and the probe, $\theta$. The angle that satisfies the phase-matching condition defers depending on the values of the other parameters of the system. This has been demonstrated on the Figure 3.16 and Figure 3.17. Gains of the probe and the conjugate are calculated as a function of angle $\theta$. These gain profiles are influenced by the index of refraction at the probe frequency, which is determined by the pump power, atom density and laser detuning. In the following, we only show the results for the conjugate, because the model gives very similar behaviour of gains of the probe and the conjugate.

In Figure 3.16, results obtained for different pump Rabi frequencies $\Omega_d$ are presented. They demonstrate that the FWM will result in different gain profiles at high and low pump power Rabi frequencies $\Omega_d$. Shown results are calculated obtained for $\Delta = 1$ GHz, and $\delta = -9.5$ MHz, probe Rabi frequency $\Omega_p = 22.5$ MHz, and atom density $N = 1 \times 10^{12}$ cm$^{-3}$. In (a) $\Omega_d = 3.25$ GHz (400 mW) and in (b) $\Omega_d = 1.95$ GHz (240 mW). Similar behaviour of the FWM gains as a function of angle we observe with the change of the temperature, i.e. atom density, Fig.ure 3.17. Results in Figure 3.17 are obtained for the same detunings, $\Delta$ and $\delta$, as the ones in the previous figure, the pump Rabi frequency was kept at $\Omega_d = 3.25$ GHz, while the atom density was changed from (a) $N = 1 \times 10^{11}$ cm$^{-3}$ to (b) $N = 1 \times 10^{12}$ cm$^{-3}$. As one can notice, for both higher density and higher

$\Omega_d$, FWM gains can be obtained in a narrow range of phase-matching angles $\theta$, and a gain maximum is away from the zero value of the angle. When the gain versus angle is a narrow peak as in Fig. 3.16(a), then $\Delta k_z$ varies for more than $2\pi$ over the propagated distance. When gain monotonically changes, as the angle increases from zero, $\Delta k_z$ changes only a little, less than $\pi/4$. Our model also predicts that when we lower the temperature or $\Omega_d$, the gain profile moves towards the smaller angles, with the gain maximum at the zero angle. This result, of a near zero optimal angle value, leads us to the conclusion that changes of the index of the refraction at the probe frequency are negligible. However, our model does not predict such changes of the pump during propagation through the atomic medium under FWM conditions. Due to the length of the intersection region of the pump and the probe of a few cm, so as the fact the both of the beams have finite cross section profiles, the phase matching condition can be satisfied in a wider range of the angles.

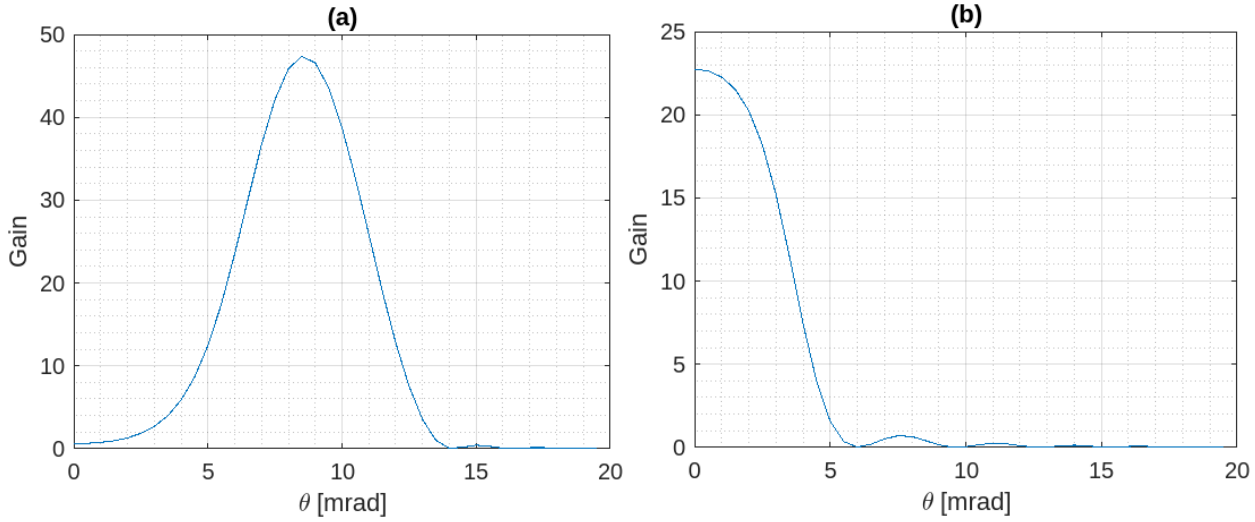


Figure 3.16 Calculated gain of the conjugate as a function of the angle $\theta$, for two pump powers: (a) $\Omega_d = 3.25$ GHz (400 mW), (b) $\Omega_d = 1.95$ GHz (240 mW), for $N = 1 \times 10^{12}$ cm$^{-3}$, $\Delta = 1$ GHz, $\delta = -9.5$ MHz, $\Omega_p = 22.5$ MHz, $\gamma = 10^2$Hz, and $\gamma_{deph} = 3 \times 10^4$Hz.

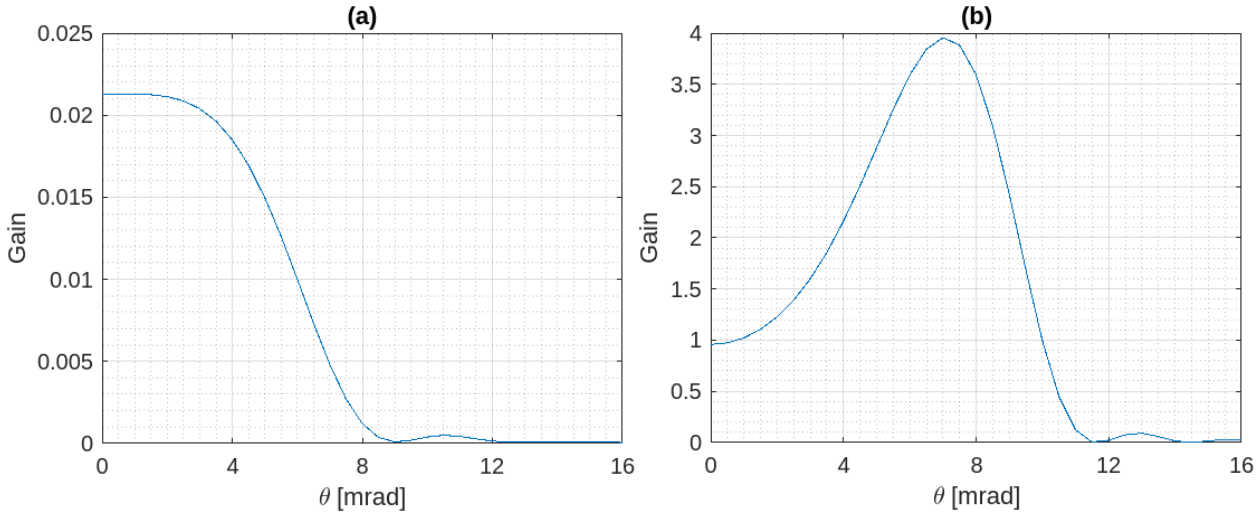


Figure 3.17 Calculated gain of the conjugate beam as a function of the angle $\theta$, for two values of the potassium density: (a) $N = 1 \times 10^{11}$cm$^{-3}$ and (b) $N = 1 \times 10^{12}$ cm$^{-3}$, for $\Omega_d = 6.47$ GHz (800 mW), $\Delta = 1$ GHz, $\delta = -9.5$ MHz, $\Omega_p = 22.5$ MHz, $\gamma = 10^5$Hz, and $\gamma_{deph} = 0$ Hz.

In Figure 3.18, experimental results of the probe and conjugate are shown. They are measured at the cell temperature of 130 $^{o}$C ($N = 5.5 \times 10^{12}$ cm$^{-3}$), and are in agreement with the theoretical predictions, Figure 3.16(b). The smallest value of the angle between the pump and the probe we needed to well separate the probe and the conjugate behind the cell and infront of the balanced detector, was $\theta = 1.5$ mrad. One photon detuning was set to $\Delta = 0.96$ GHz and two-photon detuning was $\delta = -3.7$ MHz. Pump and probe powers were 370 mW and 25 $\mu$m, respectively.

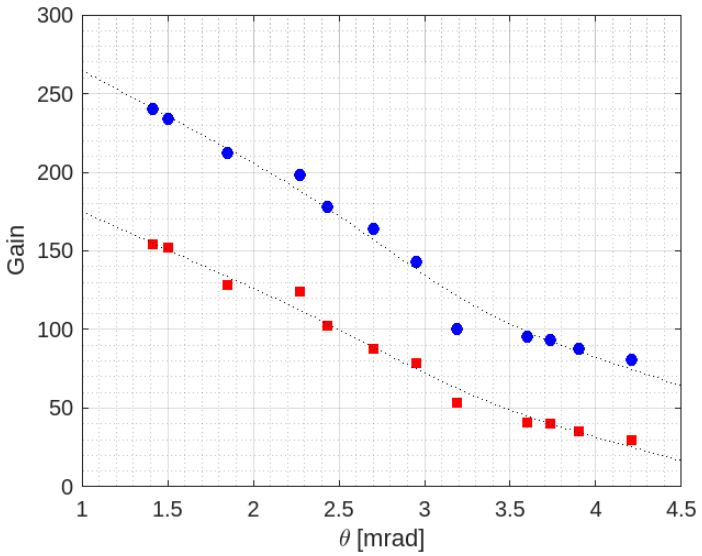


Figure 3.18 Experimental results of gains of the probe (blue pluses) and the conjugate (red stars) for $\Delta = 1$ GHz, $\delta = -3.7$ MHz, $N = 5.5 \times 10^{12}$ cm$^{-3}$ (130 $^{o}$C), $P_d = 370$ mW, and $P_p = 25$ $\mu$W.

*Dependence of gains on two-photon detuning*

Next, we investigate how the two-photon detuning affects the gain profiles. It has been already mention that in the model we have multiple fitting parameters. In Figure 3.19 is shown how relaxation rate to $\gamma$ changes the calculated results, for the same set of FWM parameters, $\Omega_d = 1.94$ GHz, $\Omega_p = 22.6$ MHz, $\theta = 6$ mrad, $N = 5.5 \times 10^{12}$ cm$^{-3}$ and $\Delta = 1$ GHz. It is interesting to note that it changes both the gains, and the width of the gain profiles. We have chosen the value of $\gamma$ for which the gain of the conjugate compares the best to the measured one.

We have made a comparison of the calculated and measured gains of the probe and conjugate as a function of $\delta$, for two different values od one-photon detuning, Figure 3.20. Shown results are for $\Delta = 1$ GHz, Figure 3.20 (a) and (b) and $\Delta = 1.35$ GHz, Figure 3.20 (c) and (d). For all the presented results the atom density was $N = 5.5 \times 10^{12}$ cm$^{-3}$. In the experiment, the angle between the pump and the probe was $\theta_{exp} = 5.5$ mrad, and pump and probe powers were 360 mW and 25 $\mu$W, respectively. In the model, we set the angle to be $\theta_{exp} = 6$ mrad, relaxation rate to $\gamma = 10^6$ Hz, while pump and probe Rabi frequencies were 1.94 GHz and 22.6 MHz, respectively. One can notice that typical profiles representing gains of the probe and conjugate as a function of $\delta$, both theoretical and experimental, are not symmetric around the gain maximum. The cause of this asymmetric shape of the lines could be found in the inhomogeneous differential Stark shift, since atoms in different areas of Gaussian beams experience different laser fields, and thus have a different AC Stark shift. The larger difference in the gain of the probe and the conjugate in the

experimental results, compared to the calculated, is probably due to the absorption of the probe photon, obtained by FWM, while is propagating towards the cell.

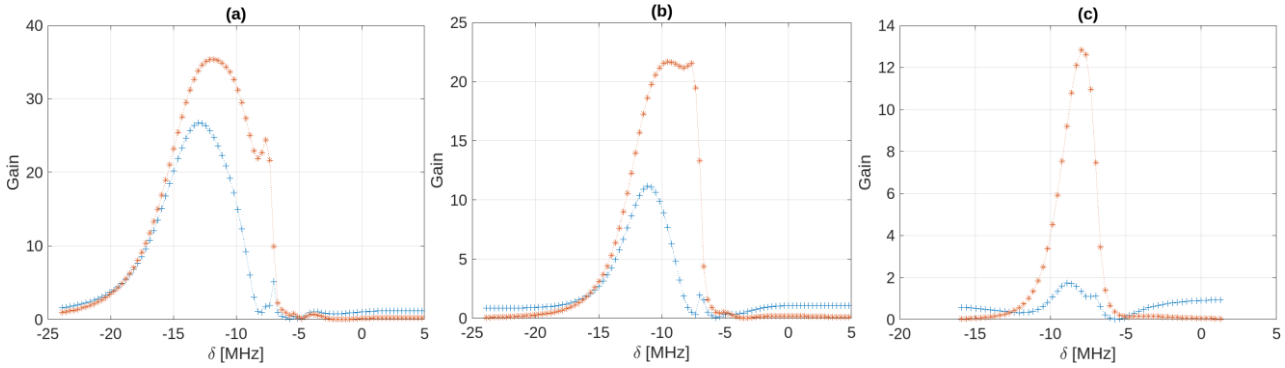


Figure 3.19 Calculated gain of the probe and the conjugate as a function of two-photon detuning, for different values of the relaxation rate (a) $\gamma = 10^6$, (b) $\gamma = 2 \times 10^6$ and (c) $\gamma = 5 \times 10^6$. The pump and probe Rabi frequencies are 1.94 GHz and 22.6 MHz, respectively. . Density $N = 5.5 \times 10^{12}$ cm$^{-3}$ (130 ºC), $\Delta = 1$GHz and $\theta = 6$ mrad.

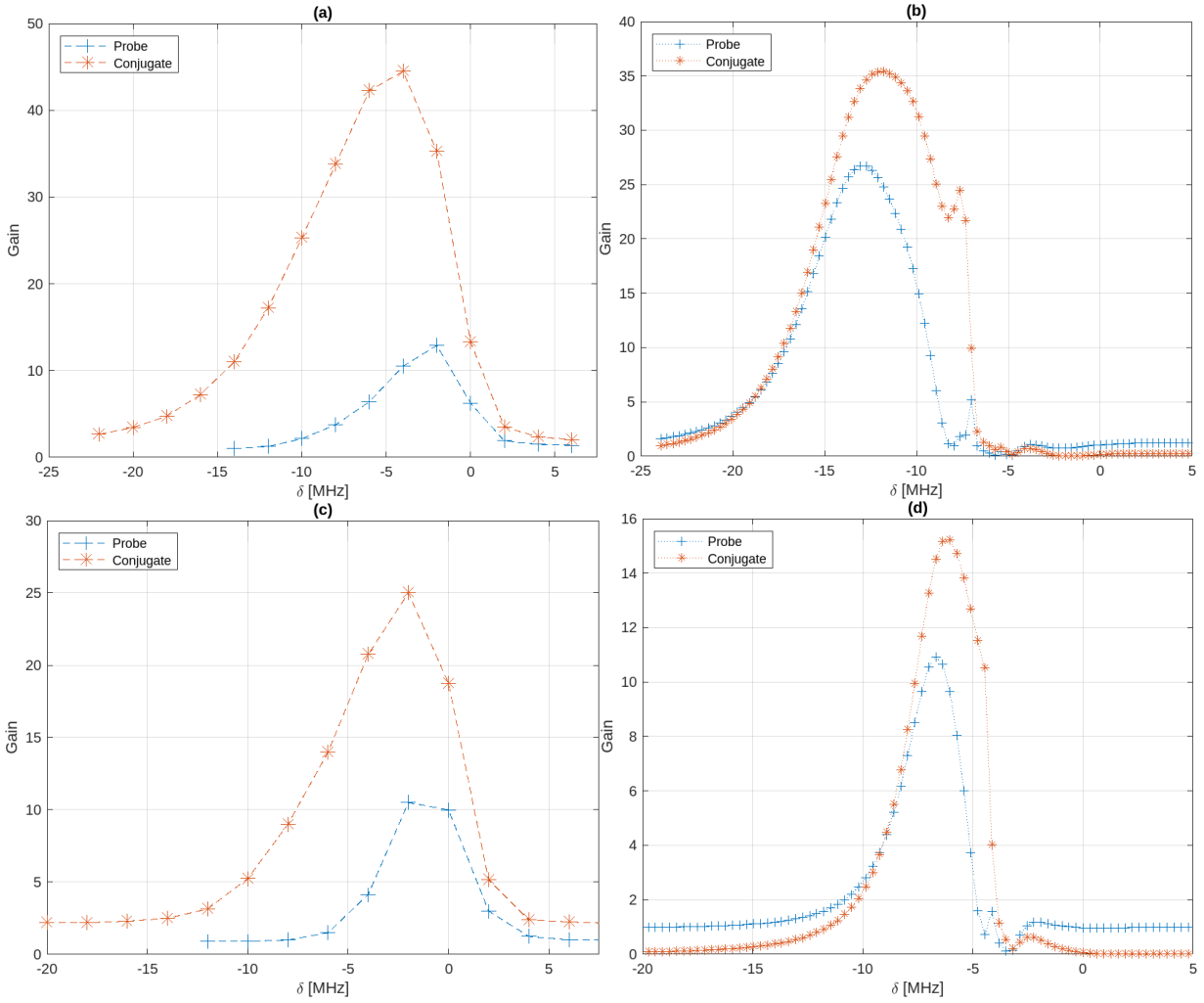


Figure 3.20 Gains of the probe and the conjugate as a function of two-photon detuning. (a), (c) Experimental results for the probe (blue pluses), and the conjugate (red stars). Pump and probe are 360 mW and 25 $\mu$W, respectively. (c),(d) Calculations of the probe (blue pluses) and conjugate (red stars) gains. The pump and probe Rabi frequencies are 1.94 GHz and 22.6 MHz, respectively. (a),(b) $\Delta = 1$GHz, (c),(d) $\Delta = 1.35$ GHz.

Density $N = 5.5 \times 10^{12}$ cm$^{-3}$ (130 °C), $\theta_{exp} = 5.5$ mrad in the experiment and $\theta_{cal} = 6$ mrad in the model. Calculations are done for $\gamma = 10^6$ Hz.

Since, our main goal in this part of the study was to gain the knowledge of how FWM gain changes with several system parameters, we performed the measurements at different cell temperatures, and for different angles between the pump and the probe. In Figure 3.20, measured gains versus $\delta$, for different one-photon detunings are shown. Maximums of gains are at $\delta_m$, different from zero and therefore shifted from two-photon resonance. However, it is evident from both Figures 3.20 and 3.21 that this optimal value of the two-photon detuning moves toward the resonance, $\delta = 0$, as we go further from the one-photon laser resonance. The results predicted by our model, in Figure 3.20(b) and (d) are in accordance with this conclusion. This shift is mainly due to differential Stark shift, $\delta_s$, because of the off-resonant pump. Hence, in the case when the $\Delta = 0.67$ GHz, as in Figure 3.21(a), we got $\delta_m \approx -10$ MHz, while for $\Delta = 1.45$ GHz, as in Figure 3.21(c), the gain maximum was shifted considerably to $\delta_m \approx -2.5$ MHz. For results in both Figures 3.20 and 3.21, $N = 5.5 \times 10^{12}$ cm$^{-3}$ (130 °C), $\theta = 4$ mrad, and pump and probe powers are 360 mW and 25 $\mu$W, respectively. The maximum of the gain curve may not coincide with the FWM resonance because of Raman absorption at the resonance. We have also investigated how $\delta_m$ varies with cell temperature, when $\Delta$ was kept fixed. In Figure 3.22 this was shown for cell temperatures from 110 °C to 150 °C, ($1.54 \times 10^{12}$ - $1.75 \times 10^{13}$ cm$^{-3}$), for $\theta = 3$ mrad. Pump and probe intensities were as in the previous case. Evidently, $\delta_m$ remains the same for different atom densities. As commented before, at the higher temperature for which we had FWM, the probe absorption is even more dominant, which gives rise to the difference between the gain of the probe and conjugate. Comparing with the results in Figure 3.22, we can notice that there is also an optimal temperature for obtaining maximal gain, for a fixed set of other experimental parameters. In this example, temperature of ~130 °C has shown to be the best choice.

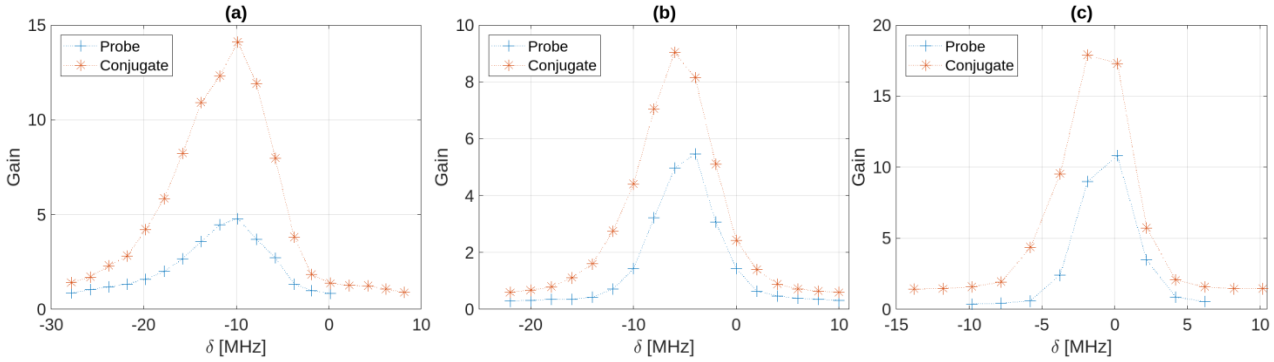


Figure 3.21 Measured gain of the probe and conjugate versus $\delta$ for three values of one-photon detuning. (a) $\Delta = 670$ MHz, (b) $\Delta = 890$ MHz and (c) $\Delta = 1450$ MHz. $N = 5.5 \times 10^{12}$ cm$^{-3}$ (130 °C), $\theta = 4$ mrad, $P_d = 360$ mW, and $P_p = 25$ $\mu$W.

*Dependence of gains on one-photon pump detuning*

What makes Potassium atom specific, compared to all other alkali metals, it is the largest Doppler broadening and the smallest HFS. Width of the Doppler broadening is important information to consider since in a hot alkali vapours it determines the range of one-photon pump detuning $\Delta$ for which we can obtain effective four-wave mixing. In the work with Rb and Cs, it has been demonstrated that, usually, laser frequency has to be detuned to the edges of Doppler profile in order to obtain high gains needed for good levels of squeezing [81,110,138].

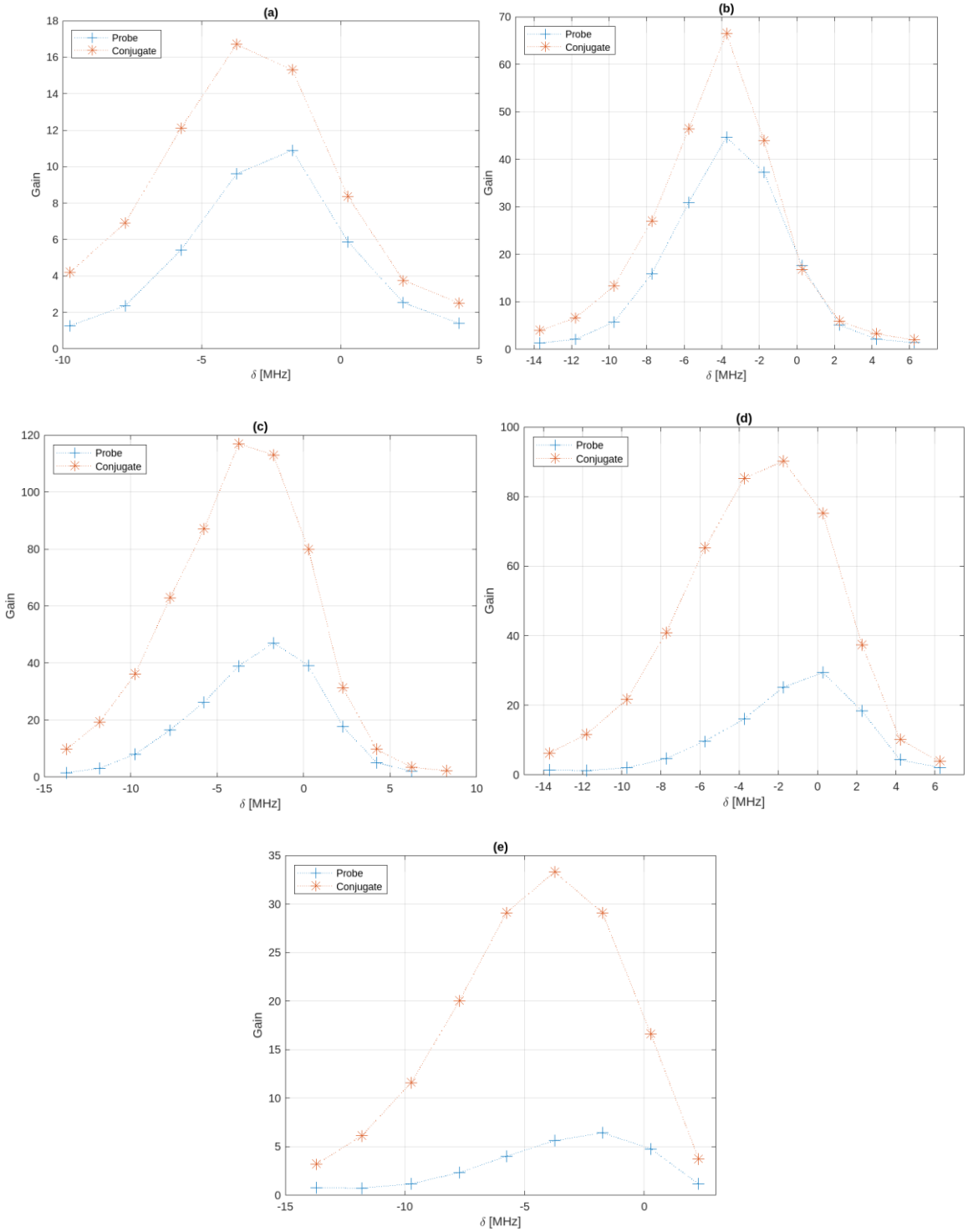


Figure 3.22 Experimental results of gains of the probe and the conjugate for five K cell temperatures (a) 110 $^{o}$C, (b) 120 $^{o}$C, (c) 130 $^{o}$C, (d) 140 $^{o}$C, (e) 150 $^{o}$C. $\Delta$= 1 GHz, $\theta = 3$ mrad, $P_d = 360$ mW, and $P_p = 25\ \mu$W.

In Figure 3.23, we present calculated and measured results for the probe and conjugate gains as a function of $\Delta$, for different value of $\delta$. Presented results are for the vapour density $N = 5.5 \times 10^{12}$ cm$^{-3}$ (130 $^{o}$C). As in the case when we studied dependence on $\delta$, change of $\Delta$ resulted in asymmetric gain profiles. The most important information we gained from these plots is the fact that optimal value of one-photon detuning, $\Delta_m$, for which maximal gain is obtained, shifts towards the lower values as we move away from the two-photon resonance. This is evident from both experimental and theoretical results. Also, as expected, for the higher gains, the pump laser has to

be detuned beyond the Doppler broadening, in order for absorption to be minimised. The broader gain profiles in the experiment, compared to the calculated ones, can be explained by the fact that the model does not consider hyperfine splitting of the excited level. Since we operate with the hot medium, where Doppler shift is present, there will be atoms resonant with all allowed hyperfine transitions between ground and excited levels, contributing the FWM process. We also observed how the results of our experiment will change with the change of the angle $\theta$, Figure 3.24. Gains at the three different δ are shown in Figure 3.24, (a) $\delta = 0$ MHz, (b) $\delta = -4$ MHz, (c) $\delta = -8$ MHz. Optimal $\Delta_m$ remains the same when we changed the angle from 5.5 mrad to 4 mrad. However, the shift in the frequency for a different $\delta$ is still present, even more pronounced compared to the case when $\theta = 5.5$ mrad.

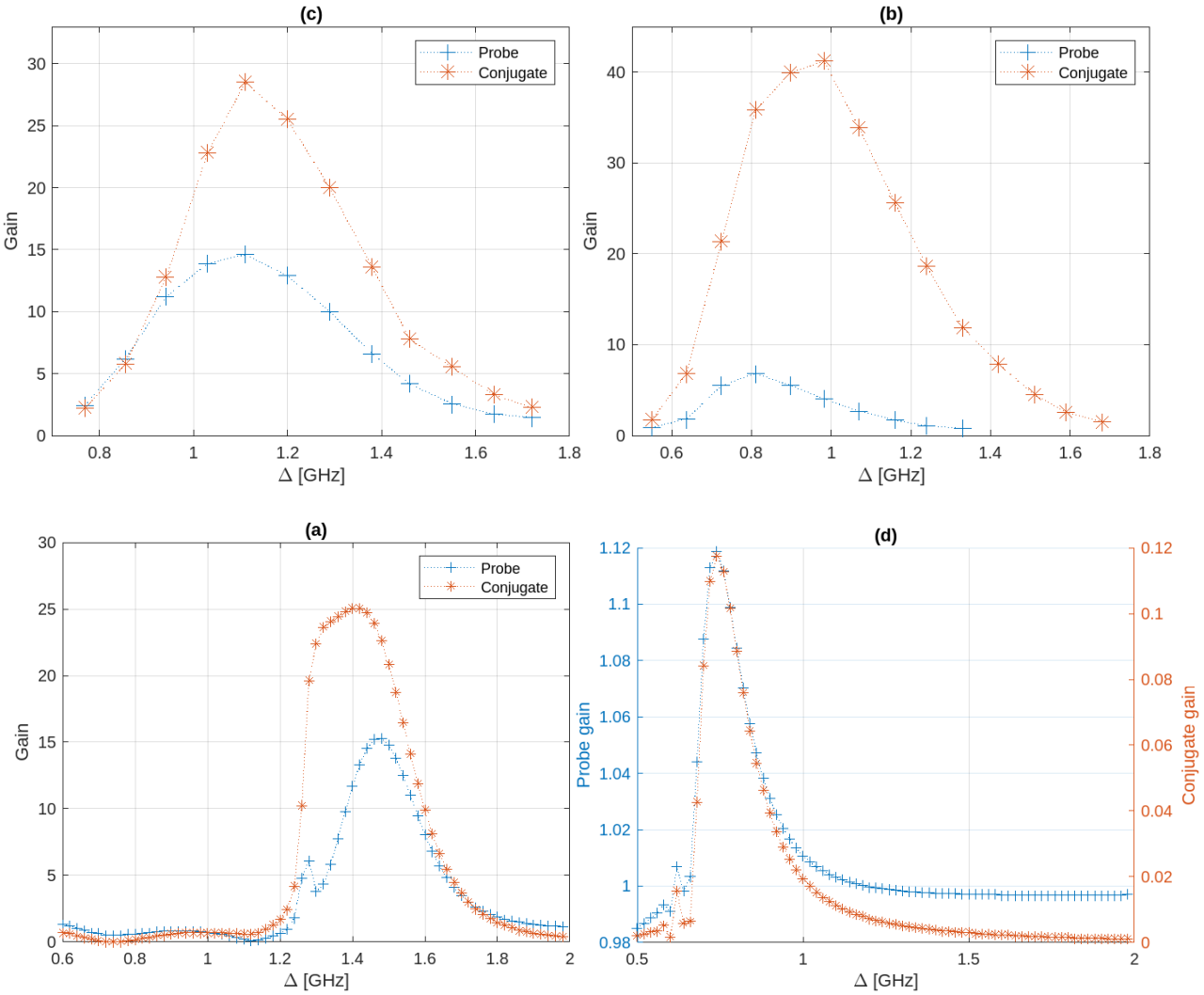


Figure 3.23 Gains of the probe and the conjugate as a function of one-photon detuning. (a), (b) Experimental results for the probe (blue pluses), and the conjugate (red stars). (a) $\delta = 0$ MHz, (b) $\delta = -8$ MHz. $\theta_{exp} = 5.5$ mrad, $N = 5.5 \times 10^{12}$ cm$^{-3}$ (130 °C). Pump and probe are 360 mW and 25 $\mu$W, respectively. (c),(d) Calculations of the probe (blue pluses) and conjugate (red stars) gains. (c) $\delta = -4$ MHz, (b) $\delta = -10$ MHz. The pump and probe Rabi frequencies are 1.94 GHz and 22.6 MHz, respectively. Calculations are done for $\gamma = 10^6$ Hz, $\theta_{cal} = 6$ mrad, $N = 5 \times 10^{12}$ cm$^{-3}$.

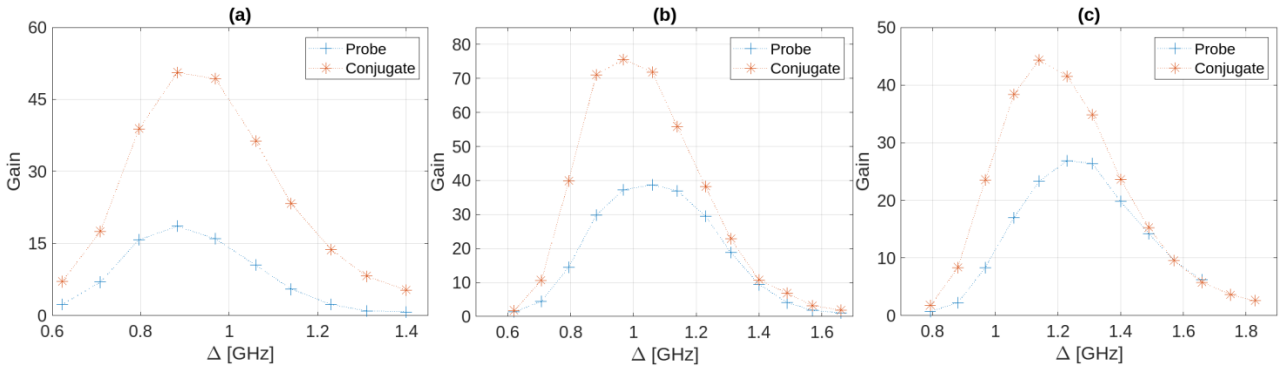


Figure 3.24 Experimental results of gains of the probe and the conjugate for three different two-photon detunings. (a) $\delta = -8$ MHz, (b) $\delta = -4$ MHz, (c) $\delta = 0$ MHz. $N = 5.5 \times 10^{12}$ cm$^{-3}$ (130 $^{o}$C), $\theta = 4$ mrad, $P_d = 360$ mW, and $P_p = 25\ \mu$W.

*Dependence of gains on the probe power*

In order to minimize the noise and obtain good squeezing level, it is also essential to minimize the power of seed laser. Note that FWM is possible, under all other parameters optimized, even without the seed, the vacuum filed was sufficient. Hence, we examined how the probe power affects the efficiency of the FWM process in potassium vapor. As demonstrated by both experimental and theoretical results in Figure 3.25, the lower the probe seed power, the higher the gain of the beams. This is in accordance with the previously stated fact that a strong pump can generate side modes or twin photons, even without the probe seed at the input, [129]. In the experiment, gains as high as 558 and 325 for the conjugate and probe respectively, were measured.

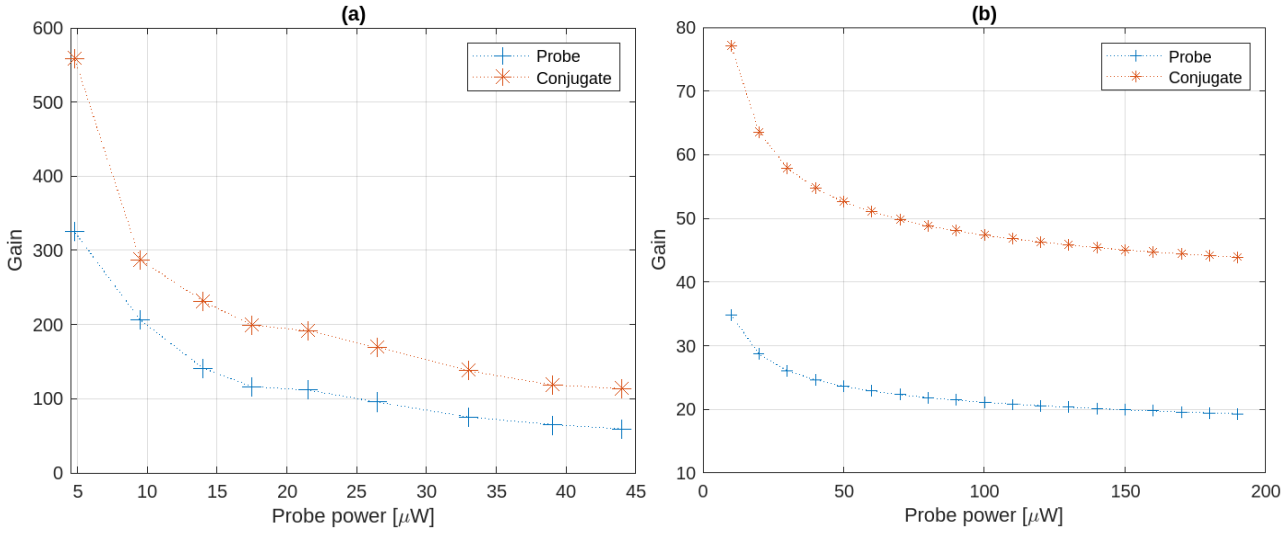


Figure 3.25 Gains of the probe and the conjugate as a function of the probe power. (a) Experimental results for $\Delta = 1$ GHz, $\delta = -4$ MHz. $N = 5.5 \times 10^{12}$ cm$^{-3}$ (130 $^{o}$C), $\theta = 3$ mrad, $P_d = 360$ mW, and $P_p = 25\ \mu$W. (b) Calculated results for $\Delta = 1.25$ GHz, $\delta = -4$ MHz. $N = 5 \times 10^{12}$ cm$^{-3}$, $\theta = 3$ mrad, $\Omega_d = 1.94$ GHz, $\Omega_p = 22.6$ MHz, $\gamma = 10^6$.

In summary, from theoretical and experimental results, performed for FWM in potassium, we have obtained important information on behaviour of probe and conjugate gains and on various

system parameters. Obtained knowledge is precious; since there are no similar investigations in this alkali vapour, and it turns it is fundamental for optimal parameters for relative intensity squeezing, presented in the next chapter.

# Part II

# Study of the relative intensity squeezing by Four Wave Mixing in Potassium vapour

# 4. Quantum states of light

In this part of the thesis we turn to the fully quantum study of four wave mixing in K. We shift our focus to the generation of relative intensity squeezing by the means of FWM. Again, our study of this topic is based on both theoretical and experimental approaches.

In this chapter we introduce the concept of quantum description of the light and new non-classical state of optical field, called squeezed light. A brief explanation of the noise reduction due to light squeezing is given. The simple description of a two-mode squeezing, relevant for our study, is presented as a function of the obtained gain in the active medium.

## 4.1. Quantum description of the light field

For quantum-mechanical treatment it is useful to introduce bosonic creation and annihilation operators for photons, $\hat{a}^\dagger$ and $\hat{a}$ [121]. These operators commutate, hence they obey the following relation:

$$[\hat{a}, \hat{a}^\dagger] = \hat{a}\hat{a}^\dagger - \hat{a}^\dagger\hat{a} = 1. \tag{4.1}$$

In this notation, Hamiltonian of an electromagnetic field EMF defined for $n$ modes of the EMF is given by:

$$\hat{H} = \sum_n \hbar\omega_n \left(\hat{a}_n{}^\dagger \hat{a}_n + \frac{1}{2}\right), \tag{4.2}$$

where $\hbar\omega_n$ is the photon energy and $\hbar\omega_n/2$ is the zero-energy of the vacuum state.

Analogous to the classical filed description, in quantum optics we can describe the field with an operator [121]:

$$\hat{E}(t) = \mathcal{E}_0\left(\hat{a}e^{-i\omega t} + \hat{a}^\dagger e^{i\omega t}\right). \tag{4.3}$$

It is convenient to present $\hat{E}$ in terms of quadrature operators $\hat{X}$ and $\hat{Y}$, referred to as cosine and sine components of signal with slowly varying envelope:

$$\hat{E}(t) = 2\mathcal{E}_0\left(\hat{X}\cos(\omega t) + \hat{Y}\sin(\omega t)\right). \tag{4.4}$$

In the last equation, $\mathcal{E}_0 = \sqrt{\hbar\omega/2\epsilon_0 V}$, with $\omega$ as the angular frequency of the field, V is the volume, and $\epsilon_0$ is the permittivity of free space. Quadrature operators $\hat{X}$ and $\hat{Y}$ are real and imaginary parts of the complex amplitude of the field, defined in terms of the creation and annihilation operators $\hat{a}^\dagger$ and $\hat{a}$ by:

$$\hat{X} = \frac{\hat{a}^\dagger + \hat{a}}{2}, \tag{4.5}$$

$$\hat{Y} = \frac{\hat{a} - \hat{a}^{\dagger}}{2i}. \tag{4.6}$$

The importance of this description is the fact that these operators are Hermitian, hence, they are physically observable quantities, and their eigenvalues are determined such that:

$$\hat{X}|X\rangle = X|X\rangle, \tag{4.7}$$

$$\hat{Y}|Y\rangle = Y|Y\rangle. \tag{4.8}$$

They also obey commutation relation $\left[\hat{X}, \hat{Y}\right] = \frac{i}{2}$. The variance of the quadrature operator is defined as:

$$\langle\left(\Delta\hat{X}\right)^2\rangle = \langle\hat{X}^2\rangle - \langle\hat{X}\rangle^2. \tag{4.9}$$

Then, the standard deviation is

$$\Delta\hat{X} = \sqrt{\Delta\hat{X}^2}. \tag{4.10}$$

By the Heisenberg uncertainty relation, uncertainties of the two defined variables must satisfy

$$\Delta\hat{X}\Delta\hat{Y} \geq \frac{1}{4}. \tag{4.11}$$

When, in the last equation, equality holds and the uncertainty of both quadratures are equal, $\Delta\hat{X} = \Delta\hat{Y} = \frac{1}{2}$, we say that the state of the light is at the quantum noise limit (QNL). With QNL, the minimal noise level of classical system is defined.

## 4.2. States of the light

*Fock state*

The eigenstates for the Hamiltonian defined by Equation (4.2) are called Fock states or number states [121]. What is characteristic for this state is that it describes the photon number state without fluctuation. We can define the number operator as [121]:

$$\hat{n} = \hat{a}^{\dagger}\hat{a}. \tag{4.12}$$

Fock states are corresponding eigenstates and we can write:

$$\hat{n}|n\rangle = \hat{a}^{\dagger}\hat{a}|n\rangle = n|n\rangle. \tag{4.13}$$

The Fock states are orthogonal, from which follows:

$$\langle n|m\rangle = \delta_{nm}, \tag{4.14}$$

and their eigenstates form canonical basis for Hilbert space. Creation and annihilation operators acting upon the number state lead to:

$$\hat{a}|n\rangle = \sqrt{n}|n-1\rangle, \tag{4.15}$$
$$\hat{a}^{\dagger}|n\rangle = \sqrt{n+1}|n+1\rangle. \tag{4.16}$$

*Vacuum state*

The term "vacuum state" has been already mentioned in the manuscript. This state is of great interest when studying and explaining many effects in research area of quantum optics.

Denoted by $|0\rangle$, this is a state without photons, which, contra-intuitively, has a non-zero energy $\hbar\omega/2$. For this state, $\langle\hat{X}\rangle = \langle\hat{Y}\rangle = 0$, however, fluctuations are still present, i.e. noise. When describing quantum states of light, it is convenient to present them on the phase diagrams, as is commonly done in the literature [131]. The described vacuum state is schematically presented on the Figure 4.1(a).

*Cherent state*

Phase diagram of coherent state is given in Figure 4.1(b). One can notice that it is actually displaced vacuum state. It is often used as the quantum description analogous to the classical state. In the close approximation, with the coherent state we describe the laser output light, that is usually quantum noise limited, and obeys the Poissonian photon statistics [131]. Coherent state depicted by $|\alpha\rangle$, with a complex amplitude $\alpha = |\alpha|e^{i\varphi}$ and phase angle $\varphi$, Figure 4.1(b), is the eigenstate of the annihilation operator, such that:

$$a|\alpha\rangle = \alpha|\alpha\rangle. \tag{4.17}$$

Coherent state can also be described with:

$$|\alpha\rangle = \hat{D}|0\rangle = e^{(\alpha\hat{a}^{\dagger} - \alpha^{*}\hat{a})}|0\rangle. \tag{4.18}$$

Here, $\hat{D}$ is a displacement operator [139], that satisfies $\hat{D}(-\alpha) = \hat{D}(\alpha)^{-1}$, $\hat{D}(\alpha)^{\dagger}\hat{a}\hat{D}(\alpha) = \hat{a} + \alpha$ and $\hat{D}(\alpha)^{\dagger}\hat{a}^{\dagger}\hat{D}(\alpha) = \hat{a}^{\dagger} + \alpha^{*}$. Sometimes it is convenient to rewrite the coherent state in terms of number states:

$$|\alpha\rangle = e^{-\frac{|\alpha|^2}{2}} \sum_{n=1}^{\infty} \frac{\alpha^n}{\sqrt{n!}}|n\rangle. \tag{4.19}$$

When number operator $\hat{n}$ is applied to the coherent state, one can obtain the expectation value of the number of photons in the respective state:

$$\langle\alpha|\hat{n}|\alpha\rangle = \langle\alpha|\hat{a}^{\dagger}\hat{a}|\alpha\rangle = \alpha^{*}\alpha\langle\alpha|\alpha\rangle = |\alpha|^2. \tag{4.20}$$

In addition, variance of the number of photon is defined as:

$$(\Delta n)^2 = \langle\alpha|\hat{n}^2|\alpha\rangle - \langle\alpha|\hat{n}|\alpha\rangle^2 = |\alpha|^2. \tag{4.21}$$

For the coherent state, uncertainties of quadrature operators satisfy the Heisenberg equality, i.e. the minimum uncertainty relation, hence:

$$\Delta\hat{X}\Delta\hat{Y} = \frac{1}{4}. \tag{4.22}$$

If we take a look at a phasor diagram on Figure 4.1(b), we can notice that the state uncertainty presentation is circular, with the quadrature uncertainties $\Delta\hat{X} = \Delta\hat{Y} = \frac{1}{2}$. The variances of the operators that describe the noise in the system are then:

$$\langle(\Delta\hat{X})^2\rangle = \langle(\Delta\hat{Y})^2\rangle = \frac{1}{4}. \tag{4.23}$$

This noise presents the classical limit that cannot be overcomed by any classical means.

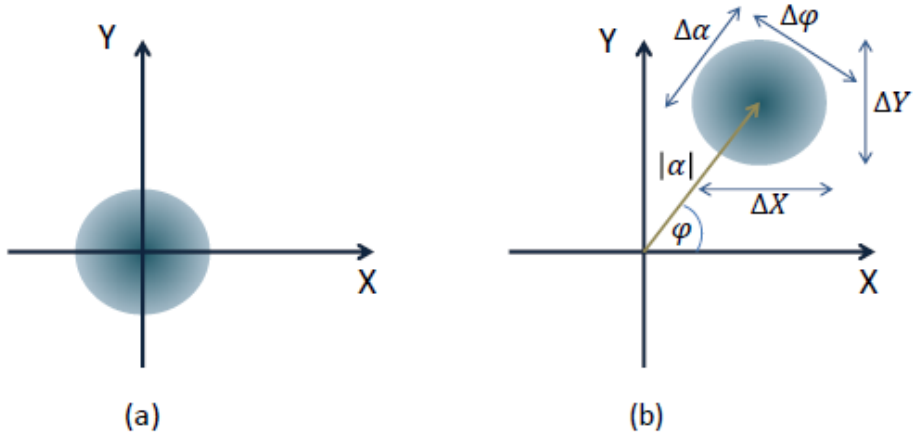


Figure 4.1 Phasor diagram presentation of (a) vacuum state, (b) coherent state of light. The grey arrow presents the amplitude $|\alpha|$. For the uncertainty area, $\Delta|\alpha|$ and $\Delta\varphi$ are defined as the amplitude and phase uncertainties, respectively.

*Squeezed state*

The uncertainty area presented the Figure 4.1, cannot be reduced. However, there are ways of reducing the uncertainty in one of the quadratures, by unequal uncertainty distribution, i.e. reducing the uncertainty in one of the quadratures at the expense of its increment in the orthogonal quadrature, as presented in Figure 4.2. These states, with the one of the quadratures uncertainties smaller compared to that of the coherent state, are called squeezed states of light [121]. Heisenberg uncertainty is still satisfied. However, now we have:

$$\langle(\Delta\hat{X})^2\rangle < \frac{1}{4}, \langle(\Delta\hat{Y})^2\rangle > \frac{1}{4}, \tag{4.24}$$

or

$$\langle(\Delta\hat{X})^2\rangle > \frac{1}{4}, \langle(\Delta\hat{Y})^2\rangle < \frac{1}{4}. \tag{4.25}$$

In quantum-mechanical formalism, squeezed state can be obtained when unitary squeezing operator $\hat{S}$ acts on the coherent state:

$$|\alpha, \zeta\rangle = \hat{S}(\zeta)|\alpha\rangle = \hat{D}(\alpha)\hat{S}(\zeta)|0\rangle. \tag{4.26}$$

Here, $\hat{D}(\alpha)$ is previously defined displacement operator, squeezing operator is $\hat{S}(\zeta) = e^{\frac{1}{2}(\zeta^* \hat{a}^2 - \zeta \hat{a}^{\dagger 2})}$, with $\zeta = se^{i\theta}$. $s$ is a squeeze factor and $\theta$ is squeezing angle, as schematically presented in Figure 4.2. It should be noted from the definition of squeezing operator, that this is a two-photon process, we have annihilation ($\hat{a}^2$) or creation ($\hat{a}^{\dagger 2}$) of two photons. Squeezing operator satisfies $\hat{S}^{-1}(\zeta) = \hat{S}^{\dagger}(\zeta)$. When it is applied to creation and annihilation operators, in the Heisenberg picture, one obtains:

$$\hat{S}^{\dagger}(\zeta)\hat{a}\hat{S}(\zeta) = \hat{a}\cosh s - \hat{a}^{\dagger} e^{i\theta}\sinh s, \tag{4.27}$$

$$\hat{S}^{\dagger}(\zeta)\hat{a}^{\dagger}\hat{S}(\zeta) = \hat{a}^{\dagger}\cosh s - \hat{a}\, e^{-i\theta}\sinh s. \tag{4.28}$$

The expectation value of the number of the photons in squeezed state is calculated by:

$$\langle\alpha|\hat{S}^{\dagger}\hat{n}\hat{S}|\alpha\rangle = \langle\alpha|\hat{S}^{\dagger}\hat{a}^{\dagger}\hat{a}\hat{S}|\alpha\rangle = |\alpha|^2 + \sinh^2 s. \tag{4.29}$$

If we compare Equation (4.29) to the Equation (4.20), describing the expectation value of the photons number in the coherent state, we can notice an additional term that is dependent on the squeeze factor.

Phase $\varphi$ is defined with respect to the reference determined by our choice of coordinate system frame. Hence, we can set $X/Y$ quadrature frame such that $\varphi = 0$. In that case, reduction of the noise in $X$ and $Y$ quadratures will be interpreted as a reduction of phase and amplitude noise, respectively. When squeezing operator is applied to the field quadrature operators, we get:

$$\hat{S}^{\dagger}(\zeta)\hat{X}\hat{S}(\zeta) = \frac{\hat{a}^{\dagger} + \hat{a}}{2}\cosh s - \frac{\hat{a}^{\dagger}e^{-i\theta} + \hat{a}e^{i\theta}}{2}\sinh s, \tag{4.30}$$

$$\hat{S}^{\dagger}(\zeta)\hat{Y}\hat{S}(\zeta) = \frac{\hat{a} - \hat{a}^{\dagger}}{2i}\cosh s - \frac{\hat{a}^{\dagger}e^{-i\theta} - \hat{a}e^{i\theta}}{2i}\sinh s. \tag{4.31}$$

If, in addition, we assume that $\theta = 0$, for the quadrature variances that are modified by the squeezing operator, we can obtain:

$$\langle\left(\Delta\hat{X}\right)^2\rangle = e^{-2s}, \tag{4.32}$$

$$\langle\left(\Delta\hat{Y}\right)^2\rangle = e^{2s}. \tag{4.33}$$

Thus, the phase noise decreases below the coherent state phase noise level (quantum noise limit), while, on the other hand, amplitude noise increases. So far, there have been different experimental demonstrations of squeezed vacuum states, and squeezed state in individual quadratures (amplitude or phase squeezed light). These squeezed states of light are often referred to *single-mode squeezed light*.

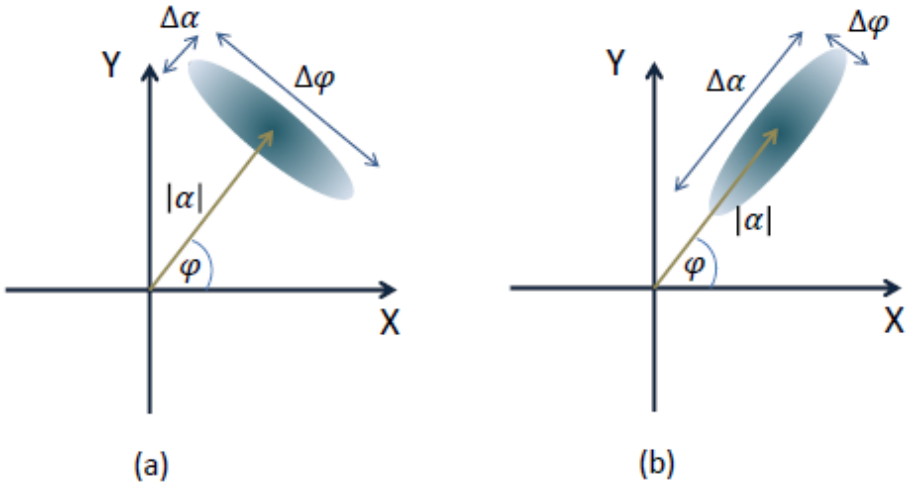


Figure 4.2 Phasor presentation of (a) amplitude squeezed light, and (b) phase squeezed light.

## 4.3. Two-mode squeezed state

In this work, we are focused on so called *two-mode squeezed states of light* [104]. In this case, the noise reduction that is explored occurs between two different modes of the electromagnetic field. What is interesting with these states is that their individual quadratures are not squeezed, but actually noisier. However, they exhibit squeezing in their sum or difference of respective quadratures due to the correlations between the modes.

We introduce two modes of the EMF, described with their quadratures:

$$\hat{E}_1(\boldsymbol{r},t) = 2\mathcal{E}_{\mathbf{0}}(\hat{X}_1\cos(\omega t) + \hat{Y}_1\sin(\omega t)) \tag{4.34}$$

$$\hat{E}_2(\boldsymbol{r},t) = 2\mathcal{E}_{\mathbf{0}}(\hat{X}_2\cos(\omega t) + \hat{Y}_2\sin(\omega t)) \tag{4.35}$$

Similarly, as for the single-mode squeezed light, we can define two-mode squeezing operator:

$$\hat{S}_2(\zeta) = e^{(\zeta^*\hat{a}\hat{b} - \zeta\hat{a}^\dagger\hat{b}^\dagger)}. \tag{4.36}$$

Here, we have two modes $a$ and $b$, with corresponding creation and annihilation operators defined for each mode. Two-mode squeezed state is then described by:

$$|\alpha,\beta,\zeta\rangle = \hat{S}_2(\zeta)|\alpha,\beta\rangle = \hat{S}_2(\zeta)\hat{D}(\alpha)\hat{D}(\beta)|0,0\rangle = e^{\frac{1}{2}(\zeta^*\hat{a}\hat{b} - \zeta\hat{a}^\dagger\hat{b}^\dagger)}e^{(\alpha\hat{a}^\dagger - \alpha^*\hat{a})}e^{(\beta\hat{b}^\dagger - \beta^*\hat{b})}|0,0\rangle, \tag{4.37}$$

where the displacement operators $\hat{D}(\alpha)$ and $\hat{D}(\beta)$ are applied on the vacuum state for each mode.

When squeezing operator acts on the annihilation operators, we obtain:

$$\hat{S}_2^\dagger(\zeta)\hat{a}\hat{S}_2(\zeta) = \hat{a}\cosh s - \hat{b}^\dagger e^{i\theta}\sinh s, \tag{4.38}$$

$$\hat{S}_2^\dagger(\zeta)\hat{b}\hat{S}_2(\zeta) = \hat{b}\cosh s - \hat{a}^\dagger e^{i\theta}\sinh s. \tag{4.39}$$

For this type of squeezing process, between the two fields modes, we define the so-called joint quadratures:

$$\hat{X}_{-} = \frac{1}{\sqrt{2}}\left(\hat{X}_1 - \hat{X}_2\right), \tag{4.40}$$

$$\hat{X}_{+} = \frac{1}{\sqrt{2}}\left(\hat{X}_1 + \hat{X}_2\right), \tag{4.41}$$

$$\hat{Y}_{-} = \frac{1}{\sqrt{2}}\left(\hat{Y}_1 - \hat{Y}_2\right), \tag{4.42}$$

$$\hat{Y}_{+} = \frac{1}{\sqrt{2}}\left(\hat{Y}_1 + \hat{Y}_2\right). \tag{4.43}$$

For them, it applies that $\left[\hat{X}_{\pm}, \hat{Y}_{\pm}\right] = \frac{i}{2}$ and $\left[\hat{X}_{\pm}, \hat{Y}_{\mp}\right] = 0$. In this description, joint quadratures can be squeezed simultaneously. Now we have that $\langle\hat{X}_{\pm}\rangle\langle\hat{Y}_{\pm}\rangle = \frac{1}{4}$. When one applies the two-mode squeezing operator and assumes that for both modes $\varphi = 0$ and $\theta = 0$, for the joint operators' variances, it is obtained:

$$\langle\left(\Delta\hat{X}_{\pm}\right)^2\rangle = e^{\pm 2s}, \tag{4.44}$$

$$\langle\left(\Delta\hat{Y}_{\pm}\right)^2\rangle = e^{\mp 2s}. \tag{4.45}$$

Hence, we can obtain noise reduction in the joint quadratures, as presented schematically in Figure 4.3.

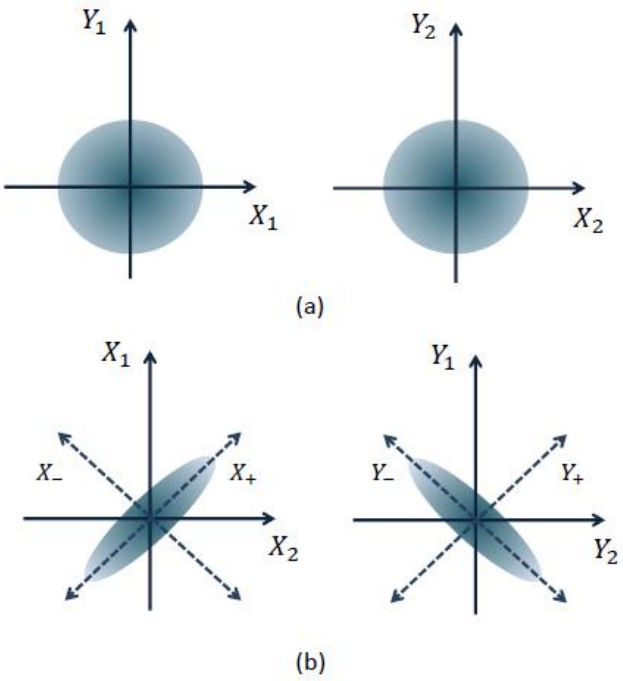


Figure 4.3 Phasor diagram for two-mode squeezed state. (a) Quadratures of output mode $\hat{a}$ and mode $\hat{b}$. (b) Joined quadratures demonstrating noise reduction.

*Ideal two-mode squeezer – the effect of the gain*

FWM is convenient for the generation of two-mode squeezed state, as it was demonstrated [81,82,110,111], since it simultaneously produces two correlated photons, probe and conjugate. In the experimental study we obtain the information on the relative intensity squeezing level by measuring the intensity difference between two detected modes. It is important to define the measurable quantities in the theoretical picture, but also to relate the gain and the respective squeezing level. The intensity and the noise of the measured signal can be compared to the theoretically determined mean photon number and its variance. Hence, we define the expected values of the number operators for two-mode states, $\hat{n}_a$ and $\hat{n}_b$ :

$$\langle \hat{n}_a \rangle = |\alpha|^2 \cosh^2 s + \sinh^2 s = |\alpha|^2 G, \tag{4.46}$$

$$\langle \hat{n}_b \rangle = (|\alpha|^2 + 1) \sinh^2 s = |\alpha|^2 (G - 1). \tag{4.47}$$

Here, $\hat{n}_a$ and $\hat{n}_b$ are number operators for the probe and conjugate, respectively. Since for the conjugate we have vacuum field at the entrance to the K vapor, it was assumed that $|\beta| = 0$, while for the bright seeded probe we have $|\alpha|^2 \gg 1$. The gain coefficient is $G \equiv \cosh^2 s$.

Next, the variances, i.e. noise on the output probe and conjugate, are described by:

$$\langle (\Delta \hat{n}_a)^2 \rangle = |\alpha|^2 \cosh^2 s \, (\cosh^2 s + \sinh^2 s) + \cosh^2 s \sinh^2 s, \tag{4.48}$$

$$\langle (\Delta \hat{n}_b)^2 \rangle = |\alpha|^2 \sinh^2 s \, (\cosh^2 s + \sinh^2 s) + \cosh^2 s \sinh^2 s. \tag{4.49}$$

With the assumption of the bright probe seed and previously defined gain, we get:

$$\langle (\Delta \hat{n}_a)^2 \rangle = |\alpha|^2 G (2G - 1), \tag{4.50}$$

$$\langle (\Delta \hat{n}_b)^2 \rangle = |\alpha|^2 (G - 1)(2G - 1). \tag{4.51}$$

Now, we can calculate the noise of the signal difference:

$$\langle \Delta(\hat{n}_a - \hat{n}_b)^2 \rangle = \langle (\Delta \hat{n}_a)^2 \rangle + \langle (\Delta \hat{n}_b)^2 \rangle - 2 \operatorname{cov}(\hat{n}_a, \hat{n}_b) = \langle (\Delta \hat{n}_a)^2 \rangle + \langle (\Delta \hat{n}_b)^2 \rangle - 2(\langle \hat{n}_a \hat{n}_b \rangle - \langle \hat{n}_a \rangle \langle \hat{n}_b \rangle). \tag{4.52}$$

To quantify the squeezing level, we need to determine the noise ratio between the output FWM state and that of the coherent one with the same power. The noise reduction factor (NRF) is given by:

$$NRF = \frac{\langle \Delta(\hat{n}_a - \hat{n}_b)^2 \rangle}{\langle \hat{n}_a + \hat{n}_b \rangle} = \frac{1}{2G - 1}. \tag{4.53}$$

Often, the results are reporter in the logarithmic units (dB), as a value of intensity difference squeezing (IDS):

$$IDS = -10 \log(2G - 1). \tag{4.54}$$

In the case of an ideal amplifier, in the absence of the absorption in the FWM medium, and neglecting the beam losses in the detection, after the mixing process, expectation value of the IDS can be modelled by the Equation (4.54). It is evident that it is directly associated with the gain in the medium, and it show us that as the gain increases we can expect for the squeezing level to increase due to the correlations in the fluctuations imparted on the probe and conjuate beams. However, under the realistic conditions, increase of squeezing with parametric gain of FWM is limited to gain values when probe absorption starts to overcome FWM mixing.

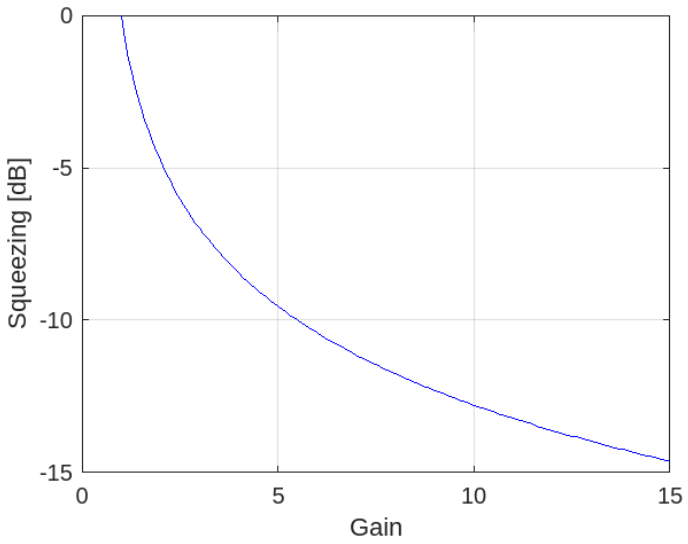


Figure 4.4 Expected IDS of an ideal FWM amplifier as a function of the gain in the medium.

# 5. Theoretical study of relative intensity squeezing by FWM in K

Within this chapter we present a study of two-mode squeezing by FWM from the theoretical perspective. This includes introducing and discussing different types of models that can be used for description of relative intensity squeezing by four-wave mixing. First, two phenomenological models, which are most commonly used in the work published so far, are described and explained. One of them introduces losses that are present in the detection on the correlated beams, after the mixing, while with the other model, we are able to include in the calculus the losses due to the absorption in the medium too. The expected levels of squeezing utilizing these models are shown and discussed. Although in some cases they have proven to be good enough for modelling and predicting the squeezing levels in systems of interest [81,110], one cannot expect that the predicted squeezing utilizing these models always match with what is expected, since, as it will be explained, they treat system as an ideal two-mode squeezer, only with losses that couple in the vacuum.

In the atomic systems, there are other competing processes, beside gain and absorption, that can lead to the excess noise, and should be included into the model to predict its behaviour realistically. To that end, we have developed microscopic model based on the Heisenberg-Langevin formalism, with more detailed description of light-atom interaction. With this model we are able to predict the behaviour and evolution of both atomic medium and the beams traveling and interacting along the active area, and calculate the gains and the squeezing. Such microscopic model has been developed and described for the cold atoms [134], but, to the best of our knowledge, there is no published work on this topic for hot atoms. We have extended the work from [134] to include the Doppler broadening and frequency detuning due to the motion of the atoms, relaxation processes in hot alkali and the transit time of the atoms through the interaction area. Also, since the model doesn't take into the account the angle between the pump and the probe, but assumes the complete overlap of laterally flat intensity beams, the model's pump Rabi frequency $\Omega$ has to be adjusted from values calculated from the formula relating laser intensity and its corresponding $\Omega$. The predicted gains and squeezing are presented and analysed for a different sets of system parameters.

## 5.1. Phenomenological approach – model of operators

As mentioned, the phenomenological model includes losses and, under such conditions, predicts level of squeezing as a function of the gain of the probe beam produced by FWM in the active medium. Two improvements on the Equation (4.53) that relates the gain and squeezing are presented in this section.

### 5.1.1. Beam-splitter model

As it has been explained, Equation (4.53) is only applicable for the modelling of an ideal FWM process, when no losses are present in the system. This is not the case in the real systems.

The first correction that is made is the inclusion of the effects of optical losses on the probe and conjugate after the mixing process occurs. This is modelled by the action of the beam-splitter (BS), as previously done in [81,138], schematically presented in the Figure 5.1. The direct detections of the probe and the conjugate are replaced by an ideal quadrature detection with fictitious BS, with probe/conjugate on the one port and the empty second input port. The vacuum modes on the empty port contribute to the output of the BS, inducing the losses in the transmitted probe/conjugate beam. For the resulting output modes of the beam splitter we can write:

$$\hat{a}_t = \sqrt{\eta_a}\hat{a}_{in} + \sqrt{1-\eta_a}\hat{a}_{vac}, \tag{5.1}$$

$$\hat{b}_t = \sqrt{\eta_b}\hat{b}_{in} + \sqrt{1-\eta_b}\hat{b}_{vac}. \tag{5.2}$$

Here, $\eta_a$ and $\eta_b$ are transmissions for the probe and conjugate, respectively, while $\hat{a}_{vac}$ and $\hat{b}_{vac}$ are vacuum modes fluctuations coupled via the BS, inducing the losses, that are superimposed with the probe and conjugate input modes. The transmission efficiencies are product of two terms that quantify transmission losses and the efficiency of the photo-detector in the experiments, $\eta_{a(b)} = \eta_{a(b),L} \times \eta_{a(b),Q}$.

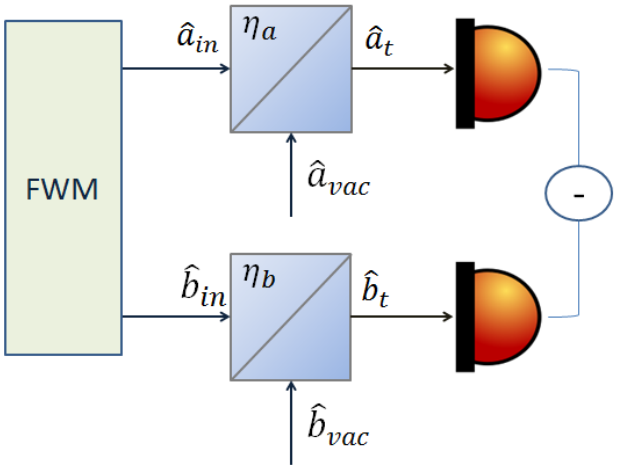


Figure 5.1 Schematic presentation of BS model implemented on the squeezing by FWM process.

State of the system with losses is described by:

$$|\alpha,\beta\rangle = \hat{O}_{BS,a}\hat{O}_{BS,b}\hat{S}_{a,b}(\zeta)|\alpha,\beta\rangle = \hat{S}_{a,b}(\zeta)\hat{D}(\alpha)|0\rangle_a|0\rangle_b|0\rangle_{a,vac}|0\rangle_{b,vac}, \tag{5.3}$$

where we use the same mathematical description and notation as in Chapter 4.3. $\hat{O}_{BS,a}$ and $\hat{O}_{BS,b}$ are the operators describing the action of a beam-splitter on the probe and conjugate modes, such that:

$$\hat{a}_t = \hat{O}^{\dagger}_{BS,a}\hat{a}_{in}\hat{O}_{BS,a}, \tag{5.4}$$

$$\hat{b}_t = \hat{O}^{\dagger}_{BS,b}\hat{b}_{in}\hat{O}_{BS,b}. \tag{5.5}$$

Displacement and squeezing operators in Equation (5.3) are as previously defined for the ideal two-mode system. Similarly, as in ideal case, photon numbers and variances can be calculated from

$$\langle \hat{n}_a \rangle_{TL} = \eta_a \langle \hat{n}_a \rangle, \tag{5.6}$$

$$\langle \hat{n}_b \rangle_{TL} = \eta_b \langle \hat{n}_b \rangle, \tag{5.7}$$

$$\langle \hat{n}_a \hat{n}_b \rangle_{TL} = \eta_a \eta_b \langle \hat{n}_a \hat{n}_b \rangle, \tag{5.8}$$

$$\langle (\Delta \hat{n}_a)^2 \rangle_{TL} = {\eta_a}^2 \langle (\Delta \hat{n}_a)^2 \rangle + \eta_a (1 - \eta_a) \langle \hat{n}_a \rangle, \tag{5.9}$$

$$\langle (\Delta \hat{n}_b)^2 \rangle_{TL} = {\eta_b}^2 \langle (\Delta \hat{n}_b)^2 \rangle + \eta_b (1 - \eta_b) \langle \hat{n}_b \rangle, \tag{5.10}$$

Index $TL$ refers to the case when transmission losses are included. Relations are presented as a function of respective photon numbers and variances, calculated when losses were neglected.

Finally, the noise on the signal difference is calculated by:

$$\langle \Delta(\hat{n}_a - \hat{n}_b) \rangle^2 = \langle (\Delta \hat{n}_a)^2 \rangle + \langle (\Delta \hat{n}_b)^2 \rangle - 2 \operatorname{cov}(\hat{n}_a, \hat{n}_b). \tag{5.11}$$

With the same assumption, as in the previous Chapter, if only the seed is at the input ($|\beta| = 0$ ) and of a bright probe at the exit from cell ($|\alpha|^2 \gg 1$), and after some algebra, the following relation for the relative noise figure can be obtained:

$$NRF_{TL} = 1 + \frac{2(G-1)(G(\eta_a - \eta_b)^2 - \eta_b^2)}{G\eta_a + (G-1)\eta_b}. \tag{5.12}$$

Previous equation indicates that in addition to the probe mixing gain, the balanced transmissions of the probe and conjugate, from the cell to the detectors, are just as important for the effective noise reduction. In Figure 5.2 the results for different values of losses, but equal on the probe and conjugate $\eta = \eta_a = \eta_b$, are presented. In that case, Equation (5.12) can be simplified to:

$$NRF_{TL} = (1 - \eta) + \frac{\eta}{2G - 1}. \tag{5.13}$$

The effect of unbalanced powers of the probe and conjugate at the detection point is demonstrated on the Figure 5.3. Presented squeezing levels are calculated in the case when probe and conjugate undergone various losses after the mixing process, changing probe transmission $\eta_a$ for a fixed $\eta_b = 0.85$. It is evident that the bigger the difference in transmission, the smaller is the expected squeezing. This can be understand by the increased amount of uncorrelated noise in the probe and conjugate at the BS output, due to the randomness of the loss process. It is also interesting to note, that the optimal conditions are obtained for a slight difference in the probe and conjugate transmission, when $\eta_a < \eta_b$. This is the result of a presence of the seeded probe photons at the output of BS, with no corresponded correlated thin photon.

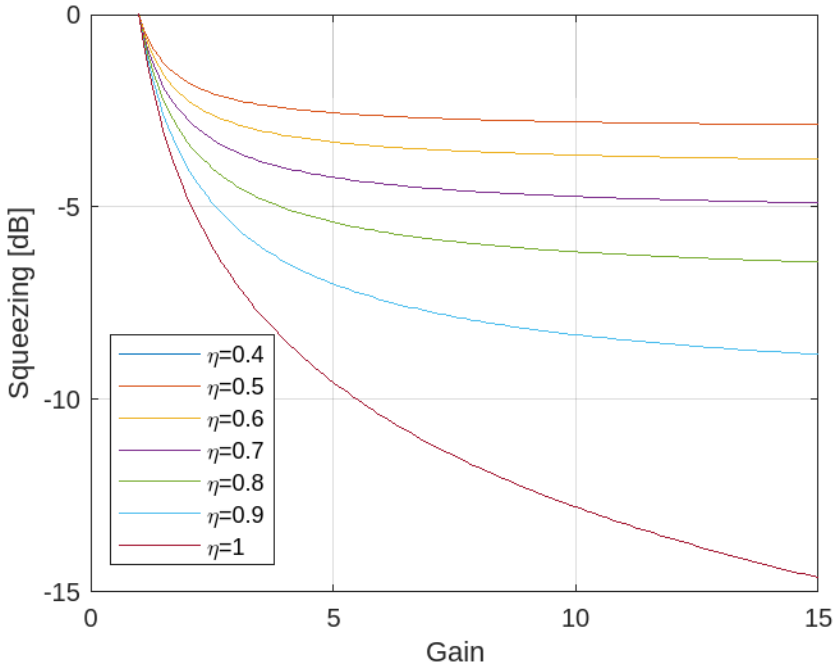


Figure 5.2 Calculated squeezing as a function of probe gain for equal losses on the probe and conjugate mode.

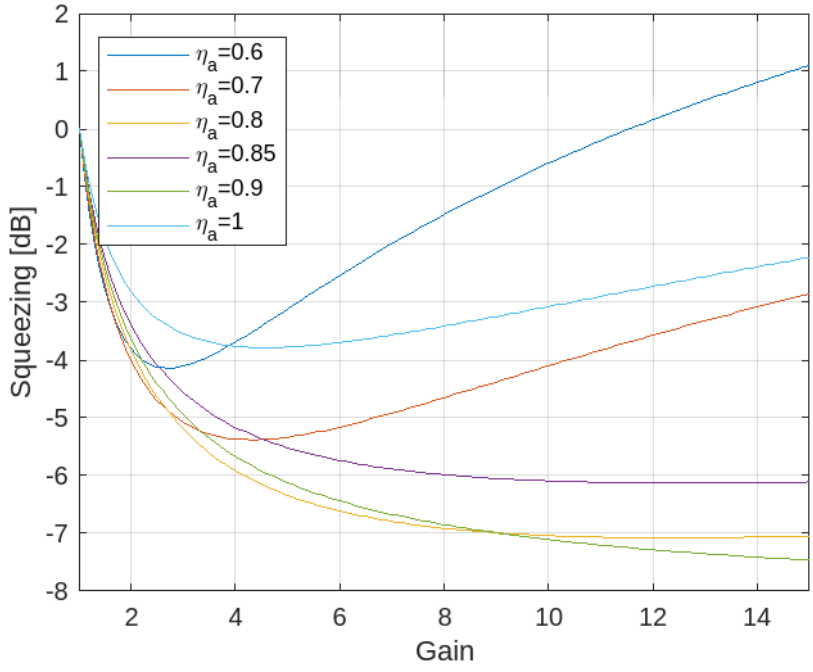


Figure 5.3 Calculated squeezing as a function of probe gain for different probe losses, when $\eta_b = 0.85$.

### 5.1.2. Intrinsic gain/loss model

In the studied systems, optical losses occur as a result of many different processes. In the previous section, only those related to the detection were considered. However, there are other effects, like absorption and spontaneous emission, happening inside the medium that impose limits on the squeezing in the vapour cell. One of the models that include these processes has been described in [138]. In this section, we resume the analytical interleaved gain/loss model developed by Jasperse et al [138]. We give brief overview of the theoretical method, and present most relevant steps and mathematical descriptions, necessary for its implementation in our study of squeezing by FWM in K vapour.

One step further in making the BS model more realistic, is taking into the account the competition between the gains and losses due to the absorption throughout the active medium. This is done by introducing a large number of the interleaved stages onto which the medium was divided along the paths of the twin beams. At every stage, besides the generated beam amplification, the losses were introduced on both probe and conjugate, through the vacuum port, as previously, by the action of a beam-splitter, Figure 5.4. For every stage the output operators are defined as follows:

$$\hat{a}_{n+1} = t_a\left(\hat{a}_n \cosh s + \hat{b}_n^{\dagger} \sinh s\right) + \sqrt{1 - t_a^2}\,\hat{a}_{vac,n+1}, \tag{5.14}$$

$$\hat{b}_{n+1} = t_b\left(\hat{a}_n \sinh s + \hat{b}_n^{\dagger} \cosh s\right) + \sqrt{1 - t_b^2}\,\hat{b}_{vac,n+1}^{\dagger}. \tag{5.15}$$

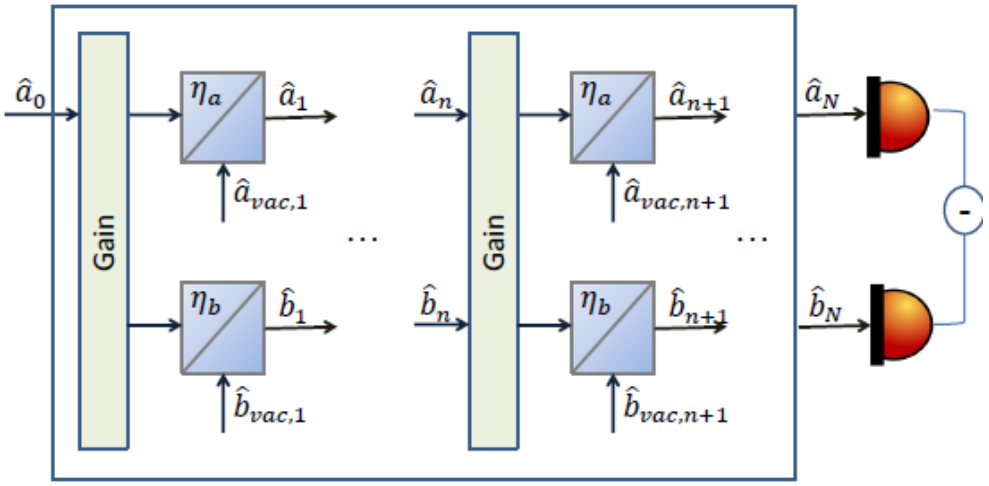


Figure 5.4 Schematic description of an interleaved gain/loss model.

Here, $N$ is the number of the interleaved segments, $s = S/N$, where the overall squeezing parameter is dependent on the intrinsic mixing gain by $G = \cosh^2 S$, and $t_a = T_a^{1/2N}$ and $t_b = T_b^{1/2N}$ as a function of the probe and conjugate transmissions in the absence of squeezing, respectively. For the input field operators, $\hat{a}_0$ and $\hat{b}_0$, output beams are described by:

$$\begin{bmatrix} \hat{a}_N \\ \hat{b}_N^{\dagger} \end{bmatrix} = \mathrm{M}^N \begin{bmatrix} \hat{a}_0 \\ \hat{b}_0^{\dagger} \end{bmatrix} + \sum_{i=1}^{N} \mathrm{M}^{N-1} \begin{bmatrix} \sqrt{1 - t_a^2}\,\hat{a}_{vac,i} \\ \sqrt{1 - t_b^2}\,\hat{b}_{vac,n+1}^{\dagger} \end{bmatrix}, \tag{5.16}$$

with

$$M = \begin{bmatrix} t_a \cosh s & t_a \sinh s \\ t_b \sinh s & t_b \cosh s \end{bmatrix}. \tag{5.17}$$

After implying some statistical and mathematical identities, one can obtain an analytical expression for the variance of the signal difference:

$$\langle \Delta(\hat{n}_a - \hat{n}_b) \rangle^2 = [\alpha_1 \quad -\beta_1]\{e^{2M_0} + X\} \begin{bmatrix} \alpha_1 \\ -\beta_1 \end{bmatrix} \langle \hat{n}_0 \rangle, \tag{5.18}$$

where

$$M_0 = \begin{bmatrix} \frac{\log T_a}{2} & S \\ S & \frac{\log T_b}{2} \end{bmatrix}, \tag{5.19}$$

$$\begin{bmatrix} \alpha_1 \\ -\beta_1 \end{bmatrix} = \begin{bmatrix} 1 & 0 \\ 0 & -1 \end{bmatrix} e^{M_0} \begin{bmatrix} 1 \\ 0 \end{bmatrix}, \tag{5.20}$$

and

$$X = \frac{1}{N} \sum_{i=1}^{N-1} \mathrm{M}^i T \mathrm{M}^i, \tag{5.21}$$

with $T = \begin{bmatrix} -\log T_a & 0 \\ 0 & -\log T_b \end{bmatrix}$, $M$ simplified to the form $M = 1 + \frac{1}{N} M_0 + O\left(\frac{1}{N^2}\right)$, for the large $N$, and $\langle \hat{n}_0 \rangle = \langle \hat{a}_0^\dagger \hat{a}_0 \rangle$.

After adding the effect of the detection losses, after the mixing, Equation (5.18) transforms to:

$$\langle \Delta(\hat{n}_a - \hat{n}_b) \rangle^2 = [\alpha_1 \quad -\beta_1]\{L(e^{2M_0} + X)L + (1 - L)L\} \begin{bmatrix} \alpha_1 \\ -\beta_1 \end{bmatrix} \langle \hat{n}_0 \rangle, \tag{5.22}$$

where $L = \begin{bmatrix} \eta_a & 0 \\ 0 & \eta_b \end{bmatrix}$.

This model has drawn our attention especially for its possibility to relate the experimentally measured gains of the probe and conjugate to the coefficients in the model:

$$G_a = \frac{\langle \hat{n}_a \rangle}{\langle \hat{n}_0 \rangle} = \eta_a \alpha_1^2, \tag{5.23}$$

$$G_b = \frac{\langle \hat{n}_b \rangle}{\langle \hat{n}_0 \rangle} = \eta_b \alpha_2^2, \tag{5.24}$$

where $G_a$and $G_b$ are measured/effective probe and conjugate gains, respectively, while $\begin{bmatrix} \alpha_1 \\ \alpha_2 \end{bmatrix} = e^{M_0} \begin{bmatrix} 1 \\ 0 \end{bmatrix}$. For the sum of the photon numbers for the detected probe and conjugate one gets:

$$\langle \hat{n}_a \rangle + \langle \hat{n}_b \rangle = (\eta_a \alpha_1^2 + \eta_b \alpha_2^2) \langle \hat{n}_0 \rangle. \tag{5.25}$$

The noise reduction factor is described by:

$$NRF_L = 1 - \eta \frac{2S\sinh^2\zeta}{\zeta\cosh(2\zeta+\chi)} + \eta\sqrt{T_a}\frac{S\log^2(T_a)\sinh^4\zeta}{2\zeta^3\cosh(2\zeta+\chi)}. \quad (5.26)$$

Here, $\zeta = \frac{1}{4}\sqrt{16S^2 + \log^2(T_a)}$ and $\tanh\chi = \frac{\log T_a - \log T_b}{4\zeta}$. In the Equation (5.26), it was assumed that $T_b = 1$. The neglection of the conjugate absorption is supported by the fact the conjugate is far detuned from the resonance.

In Figure 5.5 the expected level of squeezing are shown as a function of intrinsic mixing gain $G$ and probe transmission. For the larger gains and high probe transmission, large squeezing levels are predicted. On the other hand, for the higher amplification of the gain present in the medium, when probe absorption is dominant, squeezing level drops. Then, the optimal gain is at the lower values.

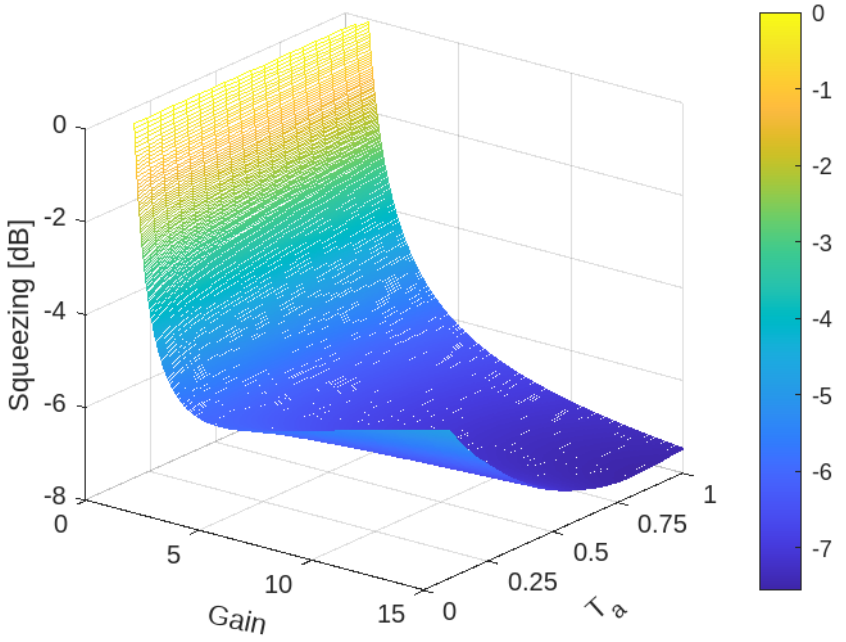


Figure 5.5 Expected squeezing for different values of probe transmission and intrinsic probe gain, when $\eta = \eta_a = \eta_b = 0.85$.

Both absorption and the strength of the mixing are characteristics of the FWM process in the alkali vapours. Hence, with the last equation we should be able to estimate effects of the FWM parameters on squeezing levels and tailor their values for the optimization. Also, assuming no optical losses behind the active medium by setting $\eta = \eta_a = \eta_b = 1$, one can estimate the ultimate squeezing expected from the FWM for particular set of system parameters. In the following Chapter, we will employ the described models to calculate the squeezing as a function of the measured gains and losses, both inside the cell and the ones caused by the detection elements, and compared obtained levels with the experimental ones.

## 5.2. Microscopic Heisenberg-Langevin model for hot vapours

In this section we introduce a microscopic model that we have developed, which can give us a more comprehensive picture of the behavior of the FWM system for two-mode squeezed light. The model presented in this section is the extension of the work done for the cold atomic system [134].

### 5.2.1. Heisenberg-Langevin model

The probe and conjugate fields, in terms of quantum operators of creation and annihilation, are described with:

$$\hat{E}_a(z,t) = \mathcal{E}_a(\hat{a}(z,t)e^{i(k_a z-\omega_a t)} + \hat{a}^\dagger(z,t)e^{-i(k_a z-\omega_a t)}. \tag{5.27}$$

$$\hat{E}_b(z,t) = \mathcal{E}_b(\hat{b}(z,t)e^{i(k_b z-\omega_b t)} + \hat{b}^\dagger(z,t)e^{-i(k_b z-\omega_b t)} \tag{5.28}$$

where $\mathcal{E}_{a(b)} = \sqrt{\frac{\hbar\omega_{a(b)}}{2\epsilon_0 V}}$ are electric fields of the single photons in the respective beams with frequencies $\omega_{a(b)}$, and $V$ is the volume. For a double-Λ system from the Figure 5.6, we define the interaction Hamiltonian, governing the light-atom interaction, by:

$$\hat{H}_{int} = -\frac{\hbar N}{L}\int_0^L (HFS + \Delta + \delta)\tilde{\sigma}_{44} + \Delta\,\tilde{\sigma}_{33} + \delta\tilde{\sigma}_{22} + \left(g_a\hat{a}(z,t)\tilde{\sigma}_{32} + g_b\hat{b}(z,t)\tilde{\sigma}_{41} + \frac{\Omega}{2}(\tilde{\sigma}_{31} + \tilde{\sigma}_{42}) + H.c.\right)dz \tag{5.29}$$

Here, $g_a = \frac{d_{32}\mathcal{E}_a}{\hbar}$ and $g_b = \frac{d_{41}\mathcal{E}_b}{\hbar}$ are coupling constants of the probe and conjugate with respective atomic transitions, the pump Rabi frequency is $\Omega = \frac{2dE}{\hbar}$, with interaction dipole $d$ and the electric filed $E$, and $N$ is the number of the atoms in volume $V$. It is assumed that $d_{13} = d_{24} = d$ and that there are no pump depletion, when traveling through the medium. As in the semiclassical description, $\tilde{\sigma}_{ii}$ $(i = 1,2,3,4)$ is the level population, while $\tilde{\sigma}_{ij}$ are coherences, in a slowly varying approximation.

In the Heisenberg picture, the evolution of this atomic system is described by the set of Heisenber-Langevin equations:

$$\left(\frac{\partial}{\partial t} + \gamma_{nm}\right)\hat{\sigma}_{nm} = \frac{i}{\hbar}\left[\hat{H}_{int}, \hat{\sigma}_{nm}\right] + \hat{R}_{nm} + \hat{F}_{nm}, \tag{5.30}$$

where the $\gamma_{nm}$ denotes sum of all of the dephasing rates, $\hat{R}_{nm}$ is spontaneous emission and $\hat{F}_{nm}$ is the Langevin operator, necessary for a quantum description of FWM process, that enables us to introduce the fluctuations in the mathematical description of the system. In the approximation, assuming that the probe power is much weaker than the pump, i.e. $\Omega_a \ll \Omega_p = \Omega$, we obtain the set of coupled differential equations:

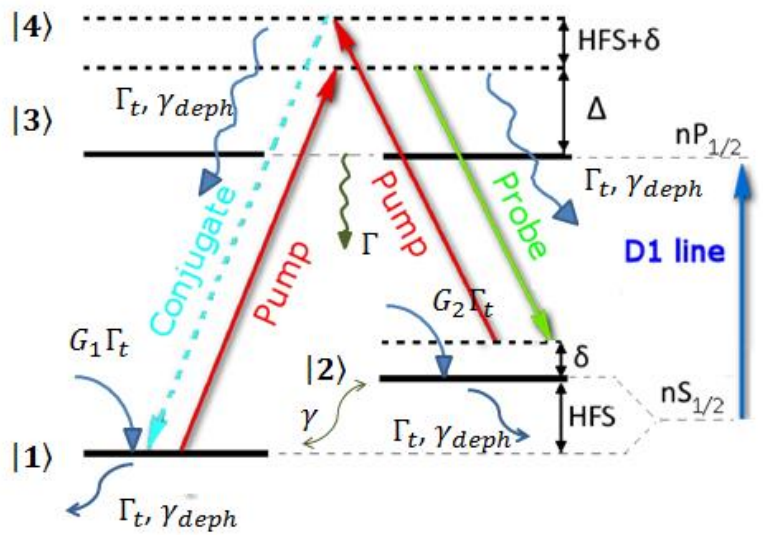


Figure 5.6 Double Λ atomic level scheme with depicted dephasing and decay rates. $\Gamma$ – total spontaneous emission from the excited states, $\Gamma_t$ – transit rate, $G_i\Gamma_t$ – filling rate of the state $|i\rangle$, $\gamma_i$ – relaxation rates from the excited states.

$$\frac{\partial}{\partial t}\tilde{\sigma}_{11} = -i\left(g_b\hat{b}\tilde{\sigma}_{41} - g_b^*\hat{b}^\dagger\tilde{\sigma}_{14} + \frac{\Omega}{2}(\tilde{\sigma}_{31} - \tilde{\sigma}_{13})\right) + \frac{\Gamma}{2}(\tilde{\sigma}_{33} + \tilde{\sigma}_{44}) - (\gamma_{deph} + \Gamma_t)\tilde{\sigma}_{11} + G_1\Gamma_t + \tilde{f}_{11}$$

$$\frac{\partial}{\partial t}\tilde{\sigma}_{22} = -i\left(g_a\hat{a}\tilde{\sigma}_{32} - g_a^*\hat{a}^\dagger\tilde{\sigma}_{23} + \frac{\Omega}{2}(\tilde{\sigma}_{42} - \tilde{\sigma}_{24})\right) + \frac{\Gamma}{2}(\tilde{\sigma}_{33} + \tilde{\sigma}_{44}) - (\gamma_{deph} + \Gamma_t)\tilde{\sigma}_{22} + G_2\Gamma_t + \tilde{f}_{22}$$

$$\frac{\partial}{\partial t}\tilde{\sigma}_{33} = -i\left(g_a^*\hat{a}^\dagger\tilde{\sigma}_{23} - g_a\hat{a}\tilde{\sigma}_{32} + \frac{\Omega}{2}(\tilde{\sigma}_{13} - \tilde{\sigma}_{31})\right) - (\gamma_3 + \gamma_{deph} + \Gamma_t)\tilde{\sigma}_{33} + \tilde{f}_{33}$$

$$\frac{\partial}{\partial t}\tilde{\sigma}_{44} = -i\left(g_b^*\hat{b}^\dagger\tilde{\sigma}_{14} - g_b\hat{b}\tilde{\sigma}_{41} + \frac{\Omega}{2}(\tilde{\sigma}_{24} - \tilde{\sigma}_{42})\right) - (\gamma_4 + \gamma_{deph} + \Gamma_t)\tilde{\sigma}_{44} + \tilde{f}_{44}$$

$$\frac{\partial}{\partial t}\tilde{\sigma}_{31} = -i\left(g_a^*\hat{a}^\dagger\tilde{\sigma}_{21} - g_b^*\hat{b}^\dagger\tilde{\sigma}_{34} + \frac{\Omega}{2}(\tilde{\sigma}_{11} - \tilde{\sigma}_{33})\right) - \left(\frac{\Gamma}{2} + i\Delta + \gamma_{deph} + \Gamma_t\right)\tilde{\sigma}_{31} + \tilde{f}_{31}$$

$$\frac{\partial}{\partial t}\tilde{\sigma}_{42} = -i\left(g_b^*\hat{b}^\dagger\tilde{\sigma}_{12} - g_a^*\hat{a}^\dagger\tilde{\sigma}_{43} + \frac{\Omega}{2}(\tilde{\sigma}_{22} - \tilde{\sigma}_{44})\right) - \left(\frac{\Gamma}{2} + i(\Delta + \mathrm{HFS}) + \gamma_{deph} + \Gamma_t\right)\tilde{\sigma}_{42} + \tilde{f}_{42},$$

(5.31) – (5.36)

and $\tilde{\sigma}_{44} = 1 - (\tilde{\sigma}_{11} + \tilde{\sigma}_{22} + \tilde{\sigma}_{33})$. We note that different relaxation and dephasing mechanisms are included in the model. $\Gamma$ is the spontaneous decay rate, $\gamma_{deph}$ is a dephasing rate due to the collisions, $\gamma_3 = \gamma_4 = \Gamma$ are relaxation rates from the excited levels. We also consider and include the transit rate that limits the interaction time. For the beam with Gaussian intensity distribution it can be expressed as a function of the beam radius and mean velocity. The mean distance that atom pass, without colliding with another atom is calculated by [141]:

$$\bar{d} = \frac{2}{w_0}\int_{-w_0/2}^{w_0/2}\sqrt{{w_0}^2 - x^2}\,dx = \pi\frac{w_0}{4}. \qquad (5.37)$$

The transit rate is now defined by:

$$\Gamma_t = \frac{\bar{u}}{\bar{d}} = \frac{1}{w_0}\sqrt{\frac{8k_B T}{m\pi}}, \tag{5.38}$$

where $m$ is the atomic mass of potassium. The filling rates of the ground sublevels are depicted with $G_1\Gamma_t$ and $G_2\Gamma_t$, where $G_i = \frac{g_i}{g_1+g_2}$ are the ground state degeneracies.

After some period of time, long enough compared to the occurring processes, system reaches the steady-state. At that point $\frac{\partial}{\partial t}\tilde{\sigma}_{ij} = 0$ and we can easily obtain the steady state solution in analytical form. Set of the Equation $(5.31) - (5.36)$ can be transformed into the matrix form:

$$\left(i[1]\frac{\partial}{\partial t} + [M_0]\right)[S_0] = [R_0] + i[F_0], \tag{5.39}$$

with

$$[M_0] = \begin{bmatrix} i\frac{\Gamma}{2}+i\Gamma_t & i\frac{\Gamma}{2} & 0 & -\frac{\Omega}{2} & \frac{\Omega}{2} & 0 & 0 \\ i\frac{\Gamma}{2} & i\frac{\Gamma}{2}+i\Gamma_t & 0 & 0 & 0 & -\frac{\Omega}{2} & \frac{\Omega}{2} \\ 0 & 0 & i\Gamma + \mathrm{i}\Gamma_t & \frac{\Omega}{2} & -\frac{\Omega}{2} & 0 & 0 \\ -\frac{\Omega}{2} & 0 & \frac{\Omega}{2} & -\Delta + i\frac{\Gamma}{2} + i\gamma_{deph} + i\Gamma_t & 0 & 0 & 0 \\ \frac{\Omega}{2} & 0 & -\frac{\Omega}{2} & 0 & \Delta + i\frac{\Gamma}{2} + i\gamma_{deph} + i\Gamma_t & 0 & 0 \\ -\frac{\Omega}{2} & -\Omega & -\frac{\Omega}{2} & 0 & 0 & -\Delta - \mathrm{HFS} + i\frac{\Gamma}{2} + i\gamma_{deph} + i\Gamma_t & 0 \\ \frac{\Omega}{2} & \Omega & \frac{\Omega}{2} & 0 & 0 & 0 & \Delta + \mathrm{HFS} + i\frac{\Gamma}{2} + i\gamma_{deph} + i\Gamma_t \end{bmatrix}$$

$$[S_0] = \begin{bmatrix} \tilde{\sigma}_{11} \\ \tilde{\sigma}_{22} \\ \tilde{\sigma}_{33} \\ \tilde{\sigma}_{31} \\ \tilde{\sigma}_{13} \\ \tilde{\sigma}_{42} \\ \tilde{\sigma}_{24} \end{bmatrix} \qquad [R_0] = \begin{bmatrix} i\Gamma + \mathrm{i}2\mathrm{G}_1\Gamma_t \\ i\Gamma + \mathrm{i}2\mathrm{G}_2\Gamma_t \\ 0 \\ 0 \\ 0 \\ -\Omega \\ \Omega \end{bmatrix} \qquad [F_0] = \begin{bmatrix} \tilde{f}_{11} \\ \tilde{f}_{22} \\ \tilde{f}_{33} \\ \tilde{f}_{31} \\ \tilde{f}_{13} \\ \tilde{f}_{42} \\ \tilde{f}_{24} \end{bmatrix}$$

The matrices $[M_0]$ and $[R_0]$ depend on decay rates, atomic level structure, pump Rabi frequency and one-photon detuning, $[S_0]$ contains the atomic operators $\tilde{\sigma}_{ij}$, while elements of $[F_0]$ are Langevine noise terms, that satisfy:

$$\langle \hat{\tilde{F}}_{nm}(z,t)\rangle = 0 \tag{5.40}$$

$$\langle \tilde{f}_{nm}(z,t)\tilde{f}_{n'm'}(z',t')\rangle = 2D_{nm,n'm'}\delta(t-t')\delta(z-z'). \tag{5.41}$$

In the last relation $D_{nm,n'm'}$ is the diffusion coefficient that can be calculated with the use of generalized Einstein relation. In the steady-state, the level populations and coherences can be calculated by:

$$[S_0] = [M_0]^{-1}[R_0] \tag{5.42}$$

In Figure 5.7 we can see in which way level populations in potassium are affected by the one-photon detuning, (a), and pump Rabi frequency, (b).

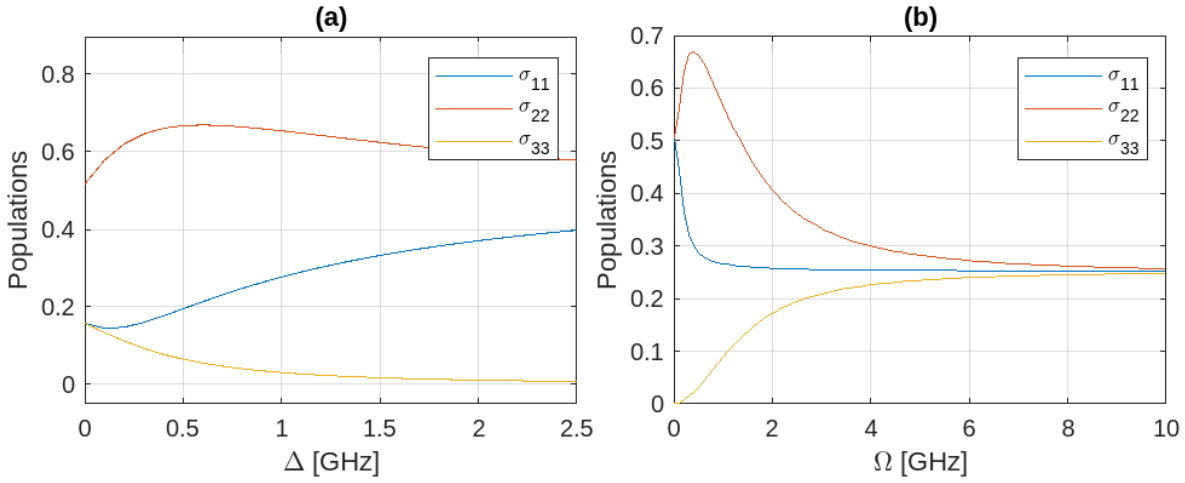


Figure 5.7 Population of the atomic states as a function of (a) one photon detuning for $\Omega =$ 0.5 GHz, (b) $\Delta = 1$ GHz. $\Gamma = 6$ MHz, $\Gamma_t = 7.6 * 10^5$ Hz, $\gamma_{deph} = 0.5 * 10^4$ Hz.

In the first approximation, the evolution of the coherences $\tilde{\sigma}_{23}$, $\tilde{\sigma}_{41}$, $\tilde{\sigma}_{43}$, $\tilde{\sigma}_{21}$ is described by

$$\frac{\partial}{\partial t}\tilde{\sigma}_{23} = \left(\delta - \Delta - \mathrm{i}\left(\frac{\Gamma}{2} + \gamma_{deph} + \Gamma_t\right)\right)\tilde{\sigma}_{23} - \frac{\Omega}{2}(\tilde{\sigma}_{21} - \tilde{\sigma}_{43}) + g_a\hat{a}(\tilde{\sigma}_{33} - \tilde{\sigma}_{22}) + i\tilde{f}_{23}$$

$$\frac{\partial}{\partial t}\tilde{\sigma}_{41} = \left(\delta + \Delta + \mathrm{HFS} - \mathrm{i}\left(\frac{\Gamma}{2} + \gamma_{deph} + \Gamma_t\right)\right)\tilde{\sigma}_{41} - \frac{\Omega}{2}(\tilde{\sigma}_{43} - \tilde{\sigma}_{21}) - g_b\hat{b}^{\dagger}(\tilde{\sigma}_{44} - \tilde{\sigma}_{11}) + i\tilde{f}_{41}$$

$$\frac{\partial}{\partial t}\tilde{\sigma}_{43} = \left(\delta + \mathrm{HFS} - \mathrm{i}\left(\Gamma + \gamma_{deph} + \Gamma_t\right)\right)\tilde{\sigma}_{43} - \frac{\Omega}{2}(\tilde{\sigma}_{41} - \tilde{\sigma}_{23}) - g_b\hat{b}^{\dagger}\tilde{\sigma}_{13} + g_a\hat{a}\tilde{\sigma}_{42} + i\tilde{f}_{43}$$

$$\frac{\partial}{\partial t}\tilde{\sigma}_{21} = \left(\delta - \mathrm{i}(\gamma_{12} + \gamma_{deph} + \Gamma_t)\right)\tilde{\sigma}_{21} - \frac{\Omega}{2}(\tilde{\sigma}_{23} - \tilde{\sigma}_{41}) - g_b\hat{b}^{\dagger}\tilde{\sigma}_{24} + g_a\hat{a}\tilde{\sigma}_{31} + i\tilde{f}_{21}$$

$$(5.43) - (5.46)$$

Again, system of equations (5.43)-(5.46) can be presented in the simplified matrix form:

$$\left(i[1]\frac{\partial}{\partial t} + [M_1]\right)[S_1(z,t)] = g[R_1]\left[\hat{O}(z,t)\right] + i[F_1(z,t)], \tag{5.47}$$

where

$$[M_1] = \begin{bmatrix} \mathrm{i}\left(\frac{\Gamma}{2}+\gamma_{deph}+\Gamma_t\right)+\Delta-\delta & 0 & -\frac{\Omega}{2} & \frac{\Omega}{2} \\ 0 & \mathrm{i}\left(\frac{\Gamma}{2}+\gamma_{deph}+\Gamma_t\right)-(\Delta+\delta+HFS) & \frac{\Omega}{2} & -\frac{\Omega}{2} \\ -\frac{\Omega}{2} & \frac{\Omega}{2} & \mathrm{i}(\Gamma+\gamma_{deph}+\Gamma_t)-\delta-HFS & 0 \\ \frac{\Omega}{2} & -\frac{\Omega}{2} & 0 & \mathrm{i}(\gamma_{12}+\Gamma_t+\gamma_{deph})-\delta \end{bmatrix}$$

$$[S_1(z,t)] = \begin{bmatrix} \tilde{\sigma}_{23}(z,t) \\ \tilde{\sigma}_{41}(z,t) \\ \tilde{\sigma}_{43}(z,t) \\ \tilde{\sigma}_{21}(z,t) \end{bmatrix} \qquad [R_1] = \begin{bmatrix} \tilde{\sigma}_{33}-\tilde{\sigma}_{22} & 0 \\ 0 & \tilde{\sigma}_{11}-\tilde{\sigma}_{44} \\ -\tilde{\sigma}_{42} & \tilde{\sigma}_{13} \\ \tilde{\sigma}_{31} & -\tilde{\sigma}_{24} \end{bmatrix}$$

$$[F_1(z,t)] = \begin{bmatrix} \tilde{f}_{23}(z,t) \\ \tilde{f}_{41}(z,t) \\ \tilde{f}_{43}(z,t) \\ \tilde{f}_{21}(z,t) \end{bmatrix} \qquad \left[\hat{O}(z,t)\right] = \begin{bmatrix} \hat{a}(z,t) \\ \hat{b}^{\dagger}(z,t) \end{bmatrix}$$

For the simulation of the fields' propagation through the medium and their temporal evolution, we employ the following Maxwell-Langevin equations:

$$\left(\frac{\partial}{\partial t}+c\frac{\partial}{\partial z}\right)\hat{a}(z,t) = ig\mathbb{N}\tilde{\sigma}_{23}(z,t), \tag{5.48}$$

$$\left(\frac{\partial}{\partial t}+c\frac{\partial}{\partial z}\right)\hat{b}^{\dagger}(z,t) = -ig\mathbb{N}\tilde{\sigma}_{41}(z,t). \tag{5.49}$$

Here, $\mathbb{N}$ is the atomic density. It has been assumed that the ideal phase-matching condition is satisfied, $\Delta k = 0$, and $g_a = g_b = g$. If we define operator matrix:

$$\left[\hat{O}(z,t)\right] = \begin{bmatrix} \hat{a}^{\dagger}(z,\omega) \\ \hat{b}(z,\omega) \end{bmatrix}, \tag{5.50}$$

equations (5.48)-(5.49) can be written in a matrix form as:

$$\left(\frac{\partial}{\partial t}+c\frac{\partial}{\partial z}\right)\left[\hat{O}(z,t)\right] = igN[T][S_1(z,t)], \tag{5.51}$$

Where $[T] = \begin{bmatrix} 1 & 0 & 0 & 0 \\ 0 & -1 & 0 & 0 \end{bmatrix}$.

We are interested in finding a solution for a measurable quantity, the gain. In order to obtain it, Equation (5.51) is solved in Fourier space. In addition, time derivative $\frac{\partial}{\partial t}$ can be neglected compared to $c\frac{\partial}{\partial z}$, under studied condition. If we define

$$[M_1'(\omega)] = \omega[1] + [M_1], \tag{5.52}$$

and after substitution in Equation (5.47), we get:

$$[M_1'(\omega)][S_1(z,\omega)] = g[R_1]\left[\hat{O}(z,\omega)\right] + i[F_1(z,\omega)], \tag{5.53}$$

with a following solution:

$$[S_1(z,\omega)] = g[M_1'(\omega)]^{-1}[R_1]\left[\hat{O}(z,\omega)\right] + i[M_1'(\omega)]^{-1}[F_1(z,\omega)]. \tag{5.54}$$

Fourier transformation of Equation (5.51) gets a form of linear non-homogenous differential equation of the first order:

$$\frac{\partial}{\partial t}\left[\hat{O}(z,\omega)\right] = [M(\omega)]\left[\hat{O}(z,\omega)\right] + [M_F][F_1(z,\omega)], \tag{5.55}$$

with

$$[M(\omega)] = i\frac{g^2N}{c}[T][M_1'(\omega)]^{-1}[R_1], \tag{5.56}$$

$$[M_F(\omega)] = -\frac{gN}{c}[T][M_1'(\omega)]^{-1}. \tag{5.57}$$

We employ the variation of constants method to obtain the solution. First, we assume the solution of the homogeneous part in a following form:

$$\left[\hat{O}_h(z,\omega)\right] = \sum_{n=0}^{\infty}\frac{z^n}{n!}\left[\hat{C}_n\right], \tag{5.58}$$

and obtain:

$$\left[\hat{O}_h(z,\omega))\right] = \sum_{n=0}^{\infty}\frac{z^n}{n!}[M(\omega))]^n\left[\hat{C}_0\right] = e^{z[M(\omega))]}\left[\hat{C}_0\right]. \tag{5.59}$$

Next, after substituting (5.58) in Equation (5.55), one gets:

$$\begin{aligned}\frac{\partial}{\partial z}\left[\hat{O}(z,\omega)\right] &= [M(\omega)]e^{z[M(\omega)]}\left[\hat{C}_0\right] + e^{z[M(\omega)]}\frac{\partial}{\partial z}\left[\hat{C}_0\right] = \\ &= [M(\omega)]e^{z[M(\omega)]}\left[\hat{C}_0\right] + [M_F(\omega)][F_1(z,\omega)],\end{aligned} \tag{5.60}$$

From the last equation it follows:

$$\frac{\partial}{\partial z}\left[\hat{C}_0\right] = e^{-z[M(\omega)]}[M_F(\omega)][F_1(z,\omega)]. \tag{5.61}$$

After the integration over the propagation distance:

$$\left[\hat{C}_0(L)\right] - \left[\hat{C}_0(0)\right] = \int_0^L e^{-z[M(w)]}[M_F(w)][F_1(z,w)]dz \tag{5.62}$$

Finally, we obtain the equation for output fields, after the mixing process within active medium of length $L$, as a function of the input fields operator:

$$\left[\hat{O}(L,\omega)\right] = e^{[M(\omega)]L}\left(\left[\hat{O}(0,\omega)\right] + L\int_0^1 e^{-[M(\omega)]Lz}[M_F(\omega)]\,[F_1(z,\omega)]dz\right). \tag{5.63}$$

*Calculating FWM gains*

Now, we are able to calculate the average values of the operators, needed for calculating the gains of the probe and conjugate beams:

$$G_a = \frac{\langle \hat{a}^\dagger(L)\hat{a}(L)\rangle}{\langle \hat{a}^\dagger(0)\hat{a}(0)\rangle} = \frac{|\alpha_{out}|^2}{|\alpha_{in}|^2}, \tag{5.64}$$

$$G_b = \frac{\langle \hat{b}^\dagger(L)\hat{b}(L)\rangle}{\langle \hat{a}^\dagger(0)\hat{a}(0)\rangle} = \frac{|\beta_{out}|^2}{|\alpha_{in}|^2}. \tag{5.65}$$

For $\omega = 0$ we have:

$$\left[\langle \hat{O}(L,0)\rangle\right] = e^{[M(0)]L}\left[\langle \hat{O}(0,0)\rangle\right] = \begin{bmatrix} A(0) & B(0) \\ C(0) & D(0) \end{bmatrix}\left[\langle \hat{O}(0,0)\rangle\right], \tag{5.66}$$

Which, in combination with equations (5.64)-(5.65), leads to:

$$G_a = |A(0)|^2, \tag{5.67}$$

$$G_b = |C(0)|^2. \tag{5.68}$$

*Calculating the squeezing level*

The main objective of this part of our study is to develop a model that can give us estimation of squeezing under a different system parameters. Hence, from the average values, we now shift our attention to the fluctuations in mathematical description of the system. Probe operator, by the linearization, can take the form of a sum:

$$\hat{a} = \langle \hat{a}\rangle + \delta\hat{a}. \tag{5.69}$$

The photon noise spectrum is defined as the Fourier transform of the autocorrelation function [142]:

$$S_I(\omega) = \int C(\tau)e^{i\omega\tau}d\tau. \tag{5.70}$$

Autocorrelation function of the intensity is [142]:

$$C(t,t') = \langle I(t)I(t')\rangle - \langle I(t)\rangle\langle I(t')\rangle = \langle \delta I(t)\delta I(t')\rangle, \tag{5.71}$$

for

$$\delta I(t) = I(t) - \langle I(t)\rangle. \tag{5.72}$$

In the stationary systems, noise is dependent on $\tau = t - t'$. For the further calculus it is useful to use the dependence of the noise density on the Fourier transform of the intensity fluctuation. Hence, we can write the following relation:

$$S_I(\omega)2\pi\delta(\omega + \omega') = \langle \delta I(\omega)\delta I(\omega')\rangle. \tag{5.73}$$

Now we can follow the approach described in details in [143], in order to determine the noise spectral density of the individual beams coming out of the interaction area, described in terms of the known system parameters. As previously stated, the spectrum of an operator can be calculated as a Fourier transform of its autocorrelation function:

$$\hat{a}(\omega) = \int_{-\infty}^{\infty} \hat{a}(t) e^{i\omega t} dt, \tag{5.74}$$

$$\hat{a}^{\dagger}(\omega) = \int_{-\infty}^{\infty} \hat{a}^{\dagger}(t) e^{i\omega t} dt. \tag{5.75}$$

Now, the noise spectrum of the probe beam can be defined as:

$$S_{\hat{n}_a}(\omega) 2\pi\delta(\omega + \omega') = \langle \delta n_a(\omega) \delta n_a^{\dagger}(\omega) \rangle = |\alpha|^2 \langle \delta \hat{X}_{\varphi}(\omega) \delta \hat{X}_{\varphi}^{\dagger}(\omega) \rangle. \tag{5.76}$$

Here, fluctuations of the photon number operator $\hat{n}_a$ are:

$$\delta \hat{n}_a = |\alpha| \delta \hat{a} e^{-i\varphi} + |\alpha| \delta \hat{a}^{\dagger} e^{i\varphi} = |\alpha| \delta \hat{X}_{\varphi}, \tag{5.77}$$

where $\delta \hat{X}_{\varphi} = \delta \hat{a} e^{-i\varphi} + \delta \hat{a}^{\dagger} e^{i\varphi}$, and the complex field amplitude is described by $|\alpha| e^{i\varphi}$, as in Chapter 4.

Fluctuations on the output beams, by previously obtained result in Equation (5.63), are defined by:

$$\left[\delta \hat{O}(L, \omega)\right] = \begin{bmatrix} \delta \hat{a}(L, \omega) \\ \delta \hat{b}^{\dagger}(L, \omega) \end{bmatrix} = \begin{bmatrix} A(\omega) & B(\omega) \\ C(\omega) & D(\omega) \end{bmatrix} \left( \left[\delta \hat{O}(0, \omega)\right] + \left[F(L, \omega)\right] \right), \tag{5.78}$$

$$\left[\delta \hat{O}^{\dagger}(L, \omega)\right] = \begin{bmatrix} \delta \hat{a}^{\dagger}(L, \omega) \\ \delta \hat{b}(L, \omega) \end{bmatrix} = \begin{bmatrix} A^*(-\omega) & B^*(-\omega) \\ C^*(-\omega) & D^*(-\omega) \end{bmatrix} \left( \left[\delta \hat{O}^{\dagger}(0, \omega)\right] + \left[F^{\dagger}(L, \omega)\right] \right). \tag{5.79}$$

For the first term on the right side we have:

$$\begin{bmatrix} A(\omega) & B(\omega) \\ C(\omega) & D(\omega) \end{bmatrix} = e^{[M(\omega)]L}, \tag{5.80}$$

while for Langevin noise terms is:

$$\left[F(L, \omega)\right] = \begin{bmatrix} F_a(L, \omega) \\ F_{b^{\dagger}}(L, \omega) \end{bmatrix} = L \int_0^1 e^{-[M(\omega)]Lz} \left[M_F(\omega)\right] \left[F_1(z, \omega)\right] dz \tag{5.81}$$

$$\left[F^{\dagger}(L, \omega)\right] = \begin{bmatrix} F_{a^{\dagger}}(L, \omega) \\ F_b(L, \omega) \end{bmatrix} = L \int_0^1 e^{-[M^*(-\omega)]Lz} \left[M_F^*(-\omega)\right] \left[F_1^{\dagger}(z, \omega)\right] dz \tag{5.82}$$

After the substitution in Equation (5.76), one can get an expression for the noise spectra in the beam as a function of system parameters defined by atomic structure and interacting beams properties, on the one hand, and Langevine terms, on the other:

$$
\begin{aligned}
&S_{\hat{n}_a}(\omega)2\pi\delta(\omega+\omega') \\
&\quad = |\alpha|^2 \langle \Big[A(\omega)(\delta\hat{a}(0,\omega)+F_a(L,\omega))e^{-i\theta} + B(\omega)\left(\delta\hat{b}^\dagger(0,\omega)+F_{b^\dagger}(L,\omega)\right)e^{-i\theta} \\
&\quad + A^*(-\omega)\left(\delta\hat{a}^\dagger(0,\omega)+F_{a^\dagger}(L,\omega)\right)e^{i\theta} + B^*(-\omega)\left(\delta\hat{b}(0,\omega)+F_b(L,\omega)\right)e^{i\theta}\Big] \\
&\quad \times \Big[A^*(-\omega')\left(\delta\hat{a}^\dagger(0,\omega')+F_{a^\dagger}(L,\omega')\right)e^{i\theta} + B^*(-\omega')\left(\delta\hat{b}(0,\omega')+F_b(L,\omega')\right)e^{i\theta} \\
&\quad + A(\omega')(\delta\hat{a}(0,\omega')+F_a(L,\omega'))e^{-i\theta} + B(\omega')\left(\delta\hat{b}^\dagger(0,\omega')+F_{b^\dagger}(L,\omega')\right)e^{-i\theta}\Big]\rangle.
\end{aligned}
\tag{5.83}
$$

Implementing the symmetric order of the operator, and presenting the Langevine noise spectrum in terms of the diffusion coefficients $D_{nm}$, after some algebra the following simplified expression for the signal noise spectrum can be obtained [143]:

$$
\begin{aligned}
S_{n_a}(\omega) = \frac{|\alpha|^2}{2}\Big(&|A(\omega)|^2\left(1+D_{aa^\dagger}(\omega,\omega)\right)+|A(-\omega)|^2\left(1+D_{a^\dagger a}(-\omega,-\omega)\right) \\
&+|B(\omega)|^2\left(1+D_{b^\dagger b}(\omega,\omega)\right)+|B(-\omega)|^2\left(1+D_{bb^\dagger}(-\omega,-\omega)\right)\Big).
\end{aligned}
\tag{5.84}
$$

Here, $D_{aa^\dagger}(\omega,\omega)$, $D_{a^\dagger a}$, $D_{b^\dagger b}$, $D_{bb^\dagger}$ are Langevin diffusion terms, defined by [134]:

$$
D_{aa^\dagger}(\omega,-\omega') = L^2[1 \quad 0|\int_0^1 \langle e^{-[M(\omega)]Lz}[M_F(\omega)][D]\ {}^t[M_F^*(-\omega')]e^{-\ {}^t[M^*(-\omega')]Lz}dz\rangle|1 \quad 0]
$$

$$
D_{a^\dagger a}(-\omega,\omega') = L^2[1 \quad 0|\int_0^1 \langle e^{-[M^*(-\omega)]Lz}[M_F^*(-\omega)][D]\ {}^t[M_F(\omega')]e^{-\ {}^t[M(\omega')]Lz}dz\rangle|1 \quad 0]
$$

$$
D_{bb^\dagger}(\omega,-\omega') = L^2[0 \quad 1|\int_0^1 \langle e^{-[M(\omega)]Lz}[M_F(\omega)][D]\ {}^t[M_F^*(-\omega')]e^{-\ {}^t[M^*(-\omega')]Lz}dz\rangle|0 \quad 1]
$$

$$
D_{b^\dagger b}(-\omega,\omega') = L^2[0 \quad 1|\int_0^1 \langle e^{-[M^*(-\omega)]Lz}[M_F^*(-\omega)][D]\ {}^t[M_F(\omega')]e^{-\ {}^t[M(\omega')]Lz}dz\rangle|0 \quad 1]
$$

$$
(5.85)-(5.88)
$$

with

$$
[D] = [D_1] + [D_2] \tag{5.89}
$$

for

$$
[D_1] = \frac{1}{2d}\begin{bmatrix}
\Gamma(\Gamma^2+4\Delta^2+2\Omega^2+8\Delta\mathrm{HFS}+4\mathrm{HFS}^2) & 0 & i\Gamma\Omega(\Gamma+2i(\Delta+\mathrm{HFS})) & 0 \\
0 & 0 & 0 & -i\Gamma\Omega(\Gamma-2i(\Delta+\mathrm{HFS})) \\
-i\Gamma\Omega(\Gamma-2i(\Delta+\mathrm{HFS})) & 0 & \Gamma\Omega^2 & 0 \\
0 & i\gamma\Omega(\Gamma+2i(\Delta+\mathrm{HFS})) & 0 & \Gamma\Omega^2+2\gamma(\Gamma^2+4\Delta^2+2\Omega^2+8\Delta\mathrm{HFS}+4\mathrm{HFS}^2)
\end{bmatrix},
$$

$$
[D_2] = \frac{1}{2d}\begin{bmatrix}
0 & 0 & 0 & -i\gamma\Omega(\Gamma-2i\Delta) \\
0 & \Gamma(\Gamma^2+4\Delta^2+2\Omega^2) & i\Gamma\Omega(\Gamma+2i\Delta) & 0 \\
0 & -i\Gamma\Omega(\Gamma-2i\Delta) & \Gamma\Omega^2 & 0 \\
i\gamma\Omega(\Gamma+2i\Delta) & 0 & 0 & \Gamma\Omega^2+2\gamma(\Gamma^2+4\Delta^2+\Omega^2)
\end{bmatrix},
$$

$$d = 2\Gamma^2 + 4\Omega^2 + 4\mathrm{HFS}^2 + 8\Delta^2 + 8\Delta\mathrm{HFS}.$$

Following the same approach as for a single beam, it is simple to calculate relative intensity difference noise by:

$$S_{n\_}(\omega)2\pi\delta(\omega+\omega') = \langle\delta\hat{n}\_(\omega)\delta\hat{n}\_^{\dagger}(\omega')\rangle, \tag{5.90}$$

where $\hat{n}\_ = \hat{n}_a - \hat{n}_b$ and $\delta\hat{n}\_(\omega) = |\alpha|\delta\hat{X}_{a,\varphi}(\omega) - |\beta|\delta\hat{X}_{b,\varphi}(\omega)$.

Final expression for the difference intensity noise spectrum is:

$$\begin{aligned} S_{n\_}(\omega) = {} & \frac{1}{2(|A(0)|^2 + |A(0)|^2)} \\ & \times \Big( |A(0)^* A(\omega) - C(0)^* C(\omega)|^2 \left(1 + D_{aa^\dagger}(\omega,\omega)\right) \\ & + |A(0)A(-\omega)^* - C(0)C(-\omega)^*|^2 \left(1 + D_{a^\dagger a}(-\omega,-\omega)\right) \\ & + |A(0)^* B(\omega) - C(0)^* D(\omega)|^2 \left(1 + D_{b^\dagger b}(\omega,\omega)\right) \\ & + |A(0)B(-\omega)^* - C(0)D(-\omega)^*|^2 \left(1 + D_{bb^\dagger}(-\omega,-\omega)\right)\Big). \end{aligned} \tag{5.91}$$

*Doppler effect on gain and squeezing by FWM*

As in the semiclassical study presented in the Past I, we are interested in the effect of the Doppler line broadening on the both gain and squeezing. As a consequence of the Doppler effect a frequency shift in the laser frequencies will be present, as explained in Chapter 3. We follow the similar procedure to include this effect in the quantum model. The atom are divided into groups each having different effective one-photon detuning $\Delta \rightarrow \Delta \pm \Delta_D = \Delta_v$. The equation (5.63) we now rewrite in the following form:

$$\left[\hat{O}(L,\omega)\right] = \left[\hat{O}(0,\omega)\right] e^{\sum_{atoms}[M(\omega,\Delta_v,\mathbb{N}_v)]L} = \left[\hat{O}(0,\omega)\right] exp \int_{-\infty}^{\infty} P(v)[M(\omega,\Delta_v)]Ldv. \tag{5.92}$$

Where $P(v)$ is the Maxwell-Boltzman distribution defined by Equation (2.11).

### 5.2.2. Results of the model – dependence of gains and squeezing on FWM parameters

Since this model takes into account different system parameter as variables, we can study the system response to their changes.

*Dependence on one-photon detuning Δ and Doppler averaging*

The comparison has been made between the results of the model for the cold atoms presented in [133], and the one in this thesis, and presented in Figure 5.8. Results published in [133] for Rb vapour, suggested that their model can predict the behaviour of the hot system in relatively

good manner. In this section we will question that and demonstrate that the effects of the model correction we introduced – relaxation processes, transit time of the atoms through the interaction area and Doppler effect. In Figure 5.8 (a),(b) we show the results of gains and squeezing obtained by the model from [133], as a function of one-photon detuning, for $\delta = 0$ MHz, $\Omega = 1.25$ GHz, $N_c = 10^{18}$ m$^{-3}$ and $L = 10$ mm. Differences in the gains and squeezing level between these results and the ones obtained by our model, Figure 5.8 (c),(d), are evident. In addition, slight shift of the optimal $\Delta$, for the maximal gain and best squeezing, is noticed. Even though model from [133] gives qualitatively sound results, our model is definitely a better choice if one wants to obtain more realistic results and predictions of the squeezer behaviour.

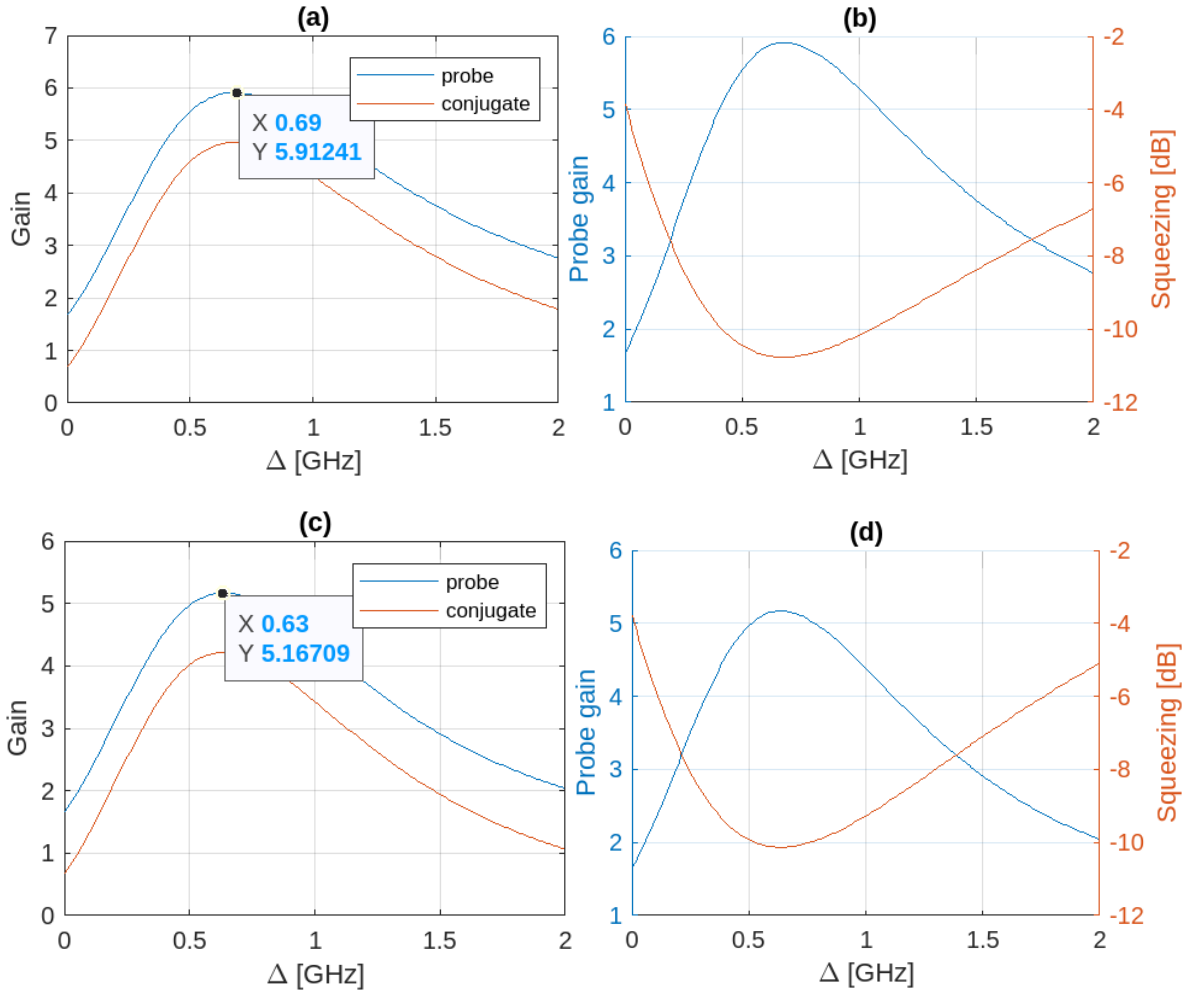


Figure 5.8 Calculated gains of the probe and conjugate (a),(c) and levels of squeezing (b),(d) as a function of $\Delta$. In the first row results are obtained by the model described in [133], while in the second row are the results from our model.

In the Figure 5.9 we show the behaviour of the modelled system as a function of $\Delta$ for two different values of the pump Rabi frequency. The gain profiles are consistent with the results obtained by the semi-classical numerical model, shown in Part I, and remind us that there are optimal value of the one-photon detuning, $\Delta_m$, for the maximal gain. Note that for these FWM parameters, the squeezing maxium also occurs at the same $\Delta_m$. This value shifts away from the resonance as we increase the pump Rabi frequency.

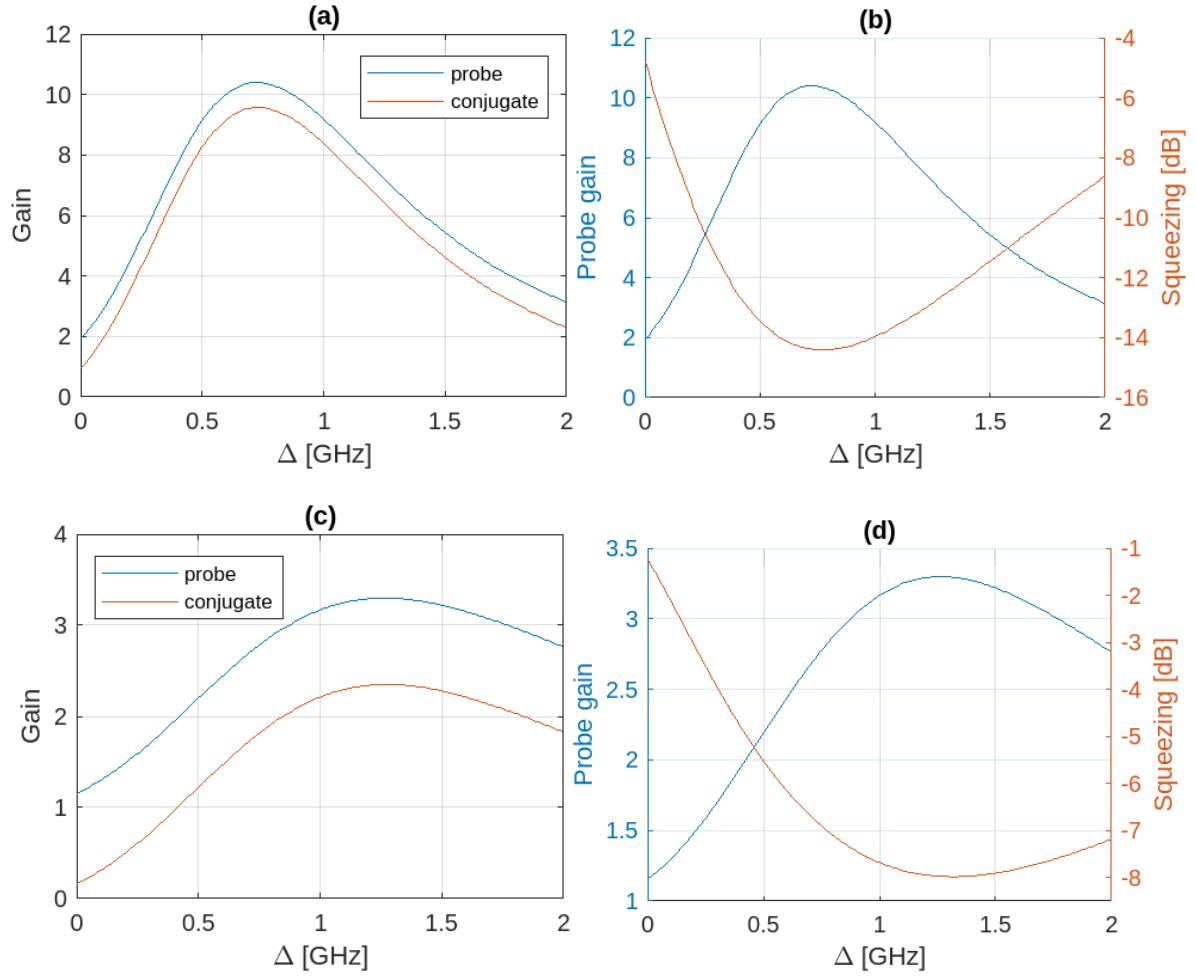


Figure 5.9 Calculated gains of the probe and conjugate (a),(c) and predicted levels of squeezing (b),(d) as a function of Δ. Results in (a) and (b) are for $\Omega = 1.25$ GHz, while the calculations presented in the bottom row are for $\Omega = 2$ GHz. Other parameters values are: $\delta = 4$ MHz, $N_c = 3 * 10^{18}$ cm$^{-3}$, $L = 10$ mm, $\Gamma = 6$ MHz, $\gamma_{deph} = 3.15 * 10^4$ Hz, $\Gamma_t = 7.6 * 10^5$ Hz.

*Dependence on pump Rabi frequency Ω*

Next, we explore the system behaviour as a function of the pump Rabi frequency, for different combinations of other FWM parameters. Results are presented in Figures 5.10 and 5.11. In Figure 5.10 the results are shown for two different one-photon detuning. For larger value of the laser detuning, higher Rabi frequencies, i.e. pump powers, are needed for the best efficiency of the mixing process. Higher amplifications of the beams are followed by the better relative intensity squeezing. If we compare the results from the Figure 5.10(a)(b) to the ones in the Figure 5.11(a)(b), we can notice that both squeezing and gain levels slightly drop as we move away from the two-photon resonance. Interesting are the results presented in the bottom row of Figure 5.11, for new, higher value of the density of the atoms. Here, the mismatch between the optimal Rabi frequencies for the maximal gain and best squeezing occurs. In all of the previously described cases, when these values of $\Omega_m$ for the gains and squeezing are aligned, probe gain is continuously higher than the gain of the conjugate, $G_a - G_b \approx 1$, as we scan the values of Δ and Ω. For the results presented in Figure 5.11(c)(d), this is not the case. The imbalance in the noise on the correlated twin beams will

shift the optimal values of, in this example, Rabi frequencies for the highest gain and squeezing with respect to each other.

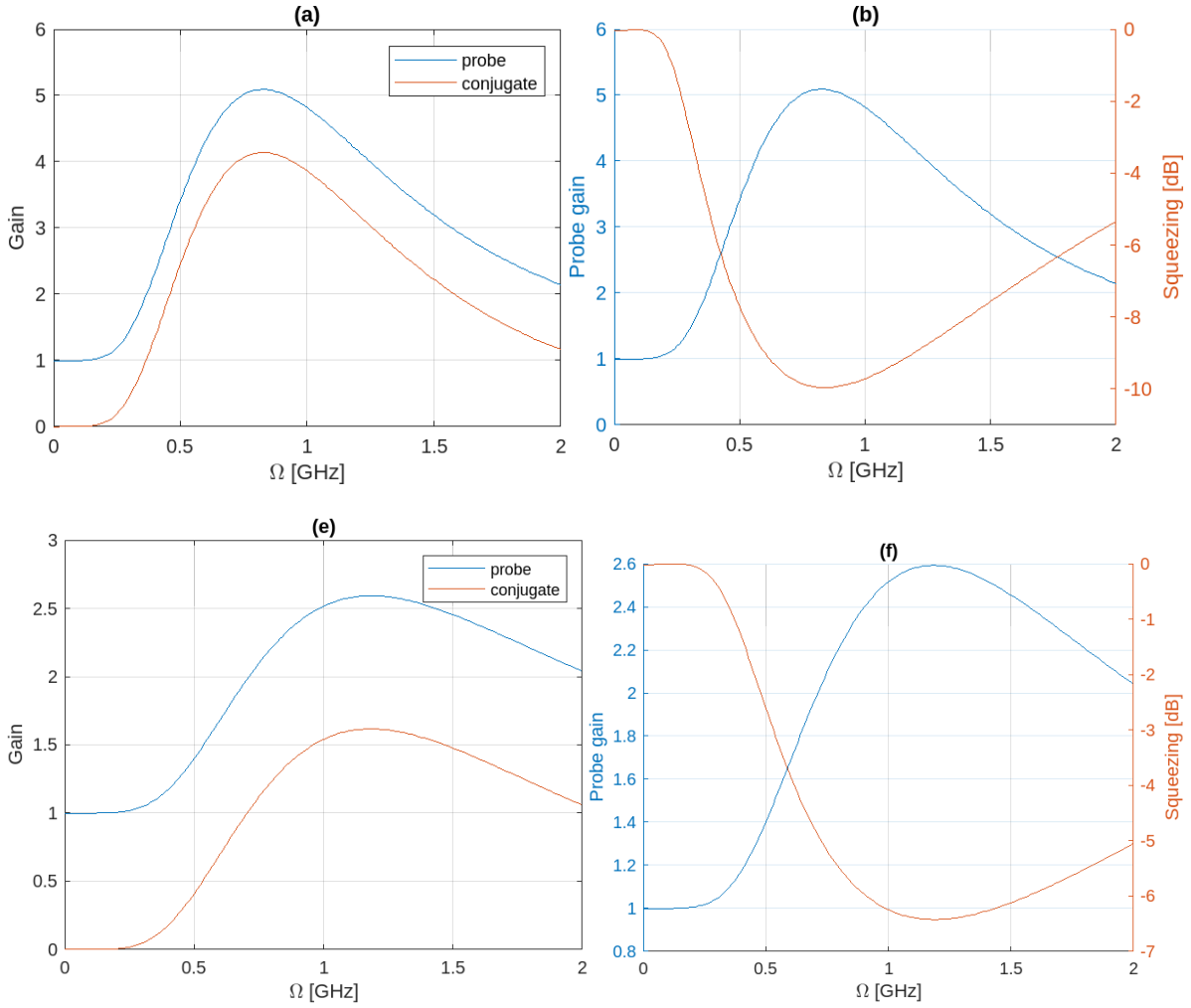


Figure 5.10 Calculated gains of the probe and conjugate (a),(c) and levels of squeezing (b),(d) as a function of Ω. Results in the first row are for $\Delta = 1$ GHz, while the calculations presented in the bottom row are for $\Delta = 1.5$ GHz. Other parameters values are: $\delta = 4$ MHz, $N_c = 1 * 10^{18}$ cm$^{-3}$, $L = 10$ mm, $\Gamma = 6$ MHz, $\gamma_{deph} = 0.5 * 10^4$ Hz, $\Gamma_t = 7.6 * 10^5$ Hz.

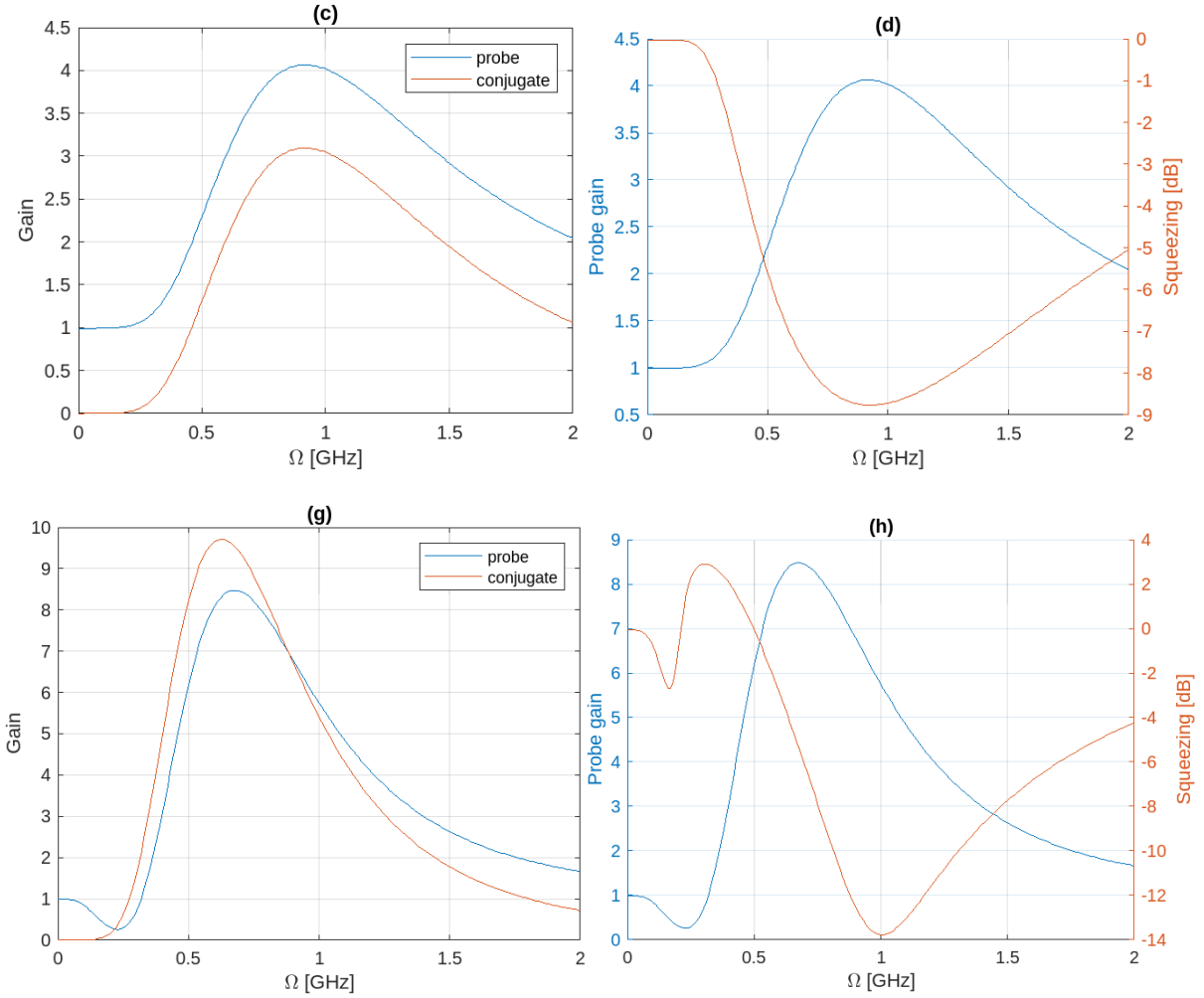


Figure 5.11 Calculated gains of the probe and conjugate (a),(c) and levels of squeezing (b),(d) as a function of $\Omega$. Results in the first row are for $\delta = 10$ MHz, $N_c = 1 * 10^{18}$ cm$^{-3}$, $\gamma_{deph} = 0.5 * 10^4$. For the second row $\delta = 10$ MHz, $N_c = 3 * 10^{18}$ cm$^{-3}$, $\gamma_{deph} = 5 * 10^6$. Other parameters values are: $\Delta = 1$ GHz, $L = 10$ mm, $\Gamma = 6$ MHz, Hz, $\Gamma_t = 7.6 * 10^5$ Hz.

*Dependence on two-photon detuning $\delta$*

During the classical study, we have learnt that two-photon probe detuning has great impact on the gain profiles. Now, we are also interested in the response of our system in terms of the obtainable squeezing levels. Calculated gains and squeezing as a function of $\delta$ are shown in Figure 5.12. These calculations are performed for the fixed pump Rabi frequency $\Omega = 1$ GHz, while we varied the one-photon detuning, for the first two rows $\Delta = 1.5$ GHz, and for the results in the third row it was $\Delta = 1$ GHz. For $\Delta = 1.5$ GHz, we have changed the atom density from $N_c = 1 * 10^{18}$ cm$^{-3}$, Figure 5.12 (a)(b), to $N_c = 3 * 10^{18}$, Figure 5.12 (c)(d). At higher potassium temperatures, higher gains, but also better squeezing levels, are obtained in the case when the probe is detuned more from the two-photon resonance. For the two lower rows, when $\Delta = 1$ GHz, and $N_c = 3 * 10^{18}$, there is no change in the optimal $\delta$ for the gain maximum. However, there is a noticeable shift of the value of $\delta$ for the most efficient squeezing with the change of the temperature. Again, the squeezing is best in the region of $\delta$ when probe gain is close or bigger than that of the conjugate.

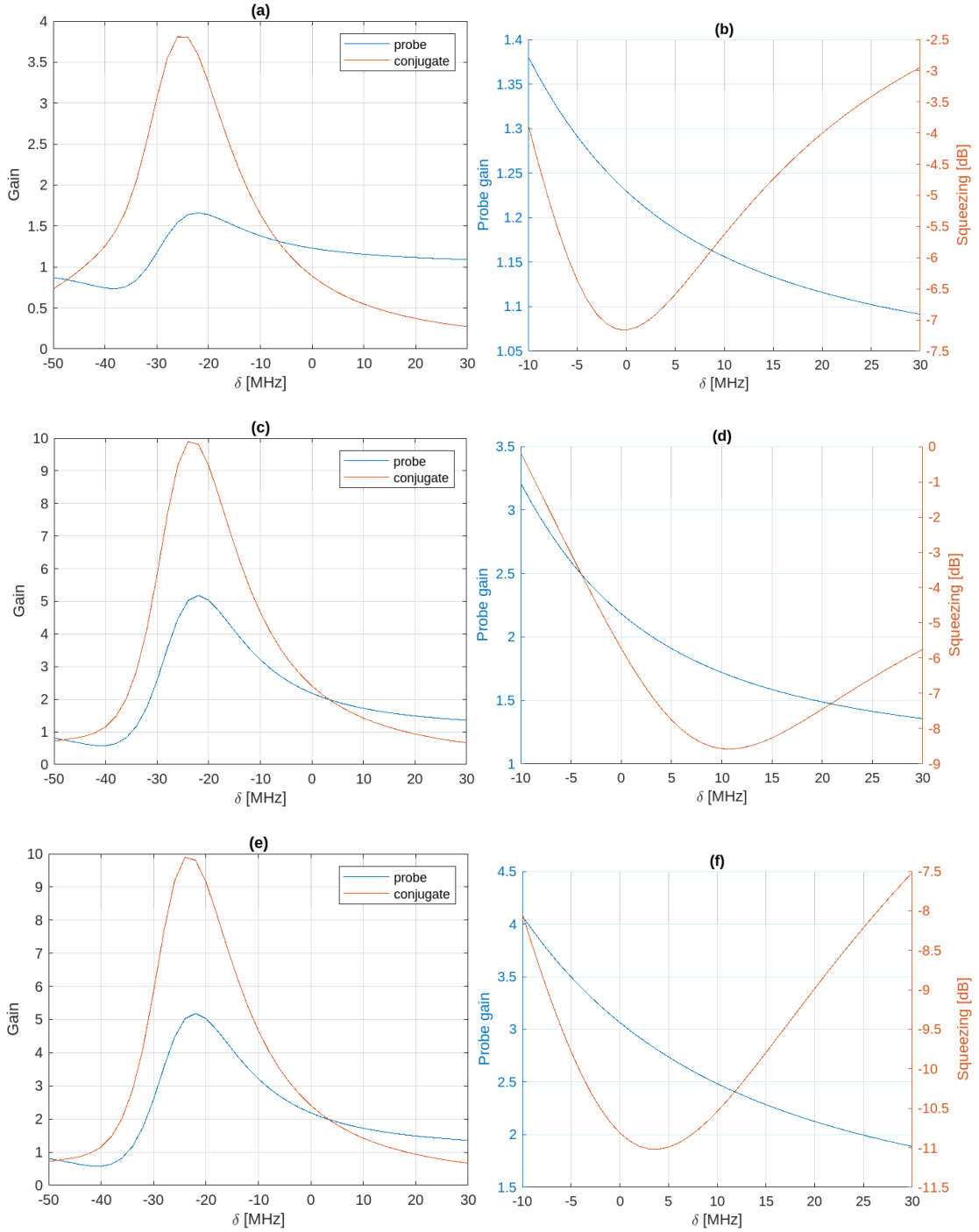


Figure 5.12 Calculated gains of the twin beams and the respective squeezing values for (a)(b) $\Delta = 1.5$ GHz, $\Omega = 1$ GHz, $N_c = 1 * 10^{18}$ cm$^{-3}$, (c)(d) $\Delta = 1.5$ GHz, $\Omega = 1$ GHz, $N_c = 3 * 10^{18}$ cm$^{-3}$, (e)(f) $\Delta = 1$ GHz, $\Omega = 1$ GHz, $N_c = 3 * 10^{18}$ cm$^{-3}$. Other parameters are $\gamma_{deph} = 1 * 10^7$, $L = 10$ mm, $\Gamma = 6$ MHz, Hz, $\Gamma_t = 7.6 * 10^5$ Hz

*Dependence on the potassium density $N_c$*

With the change of the potassium temperature, there is a striking change of values of the decay and dephasing mechanisms for agreement with experiment. In that context lies one of the importance of the theoretical work we have performed, since we have included adequate decay and dephasing rates in our model.

In Figure 5.13, results for the gains and squeezing as a function of atom density are presented. Interestingly, we can enhance the amplification process while rising up the temperature, however, for the best squeezing there is an optimal atom density. The results indicate that when we are detuned near the edges of the Doppler broadening of absorption line, the temperature has to be lower for the best squeezing. Even at this lower one-photon detuning, Figure 5.13(c)(d), the model suggests that good levels of squeezing can be obtained.

In summary, we have developed and tested new model for calculation of FMW gains and squeezing in hot alkali vapours. It is evident that there are lot of variables in the system affecting its behaviour and results of gains and squeezing, and that these relation are not always easy to predict and understand. To that end, our model is of the great assistance when one is in the search for the desired system response.

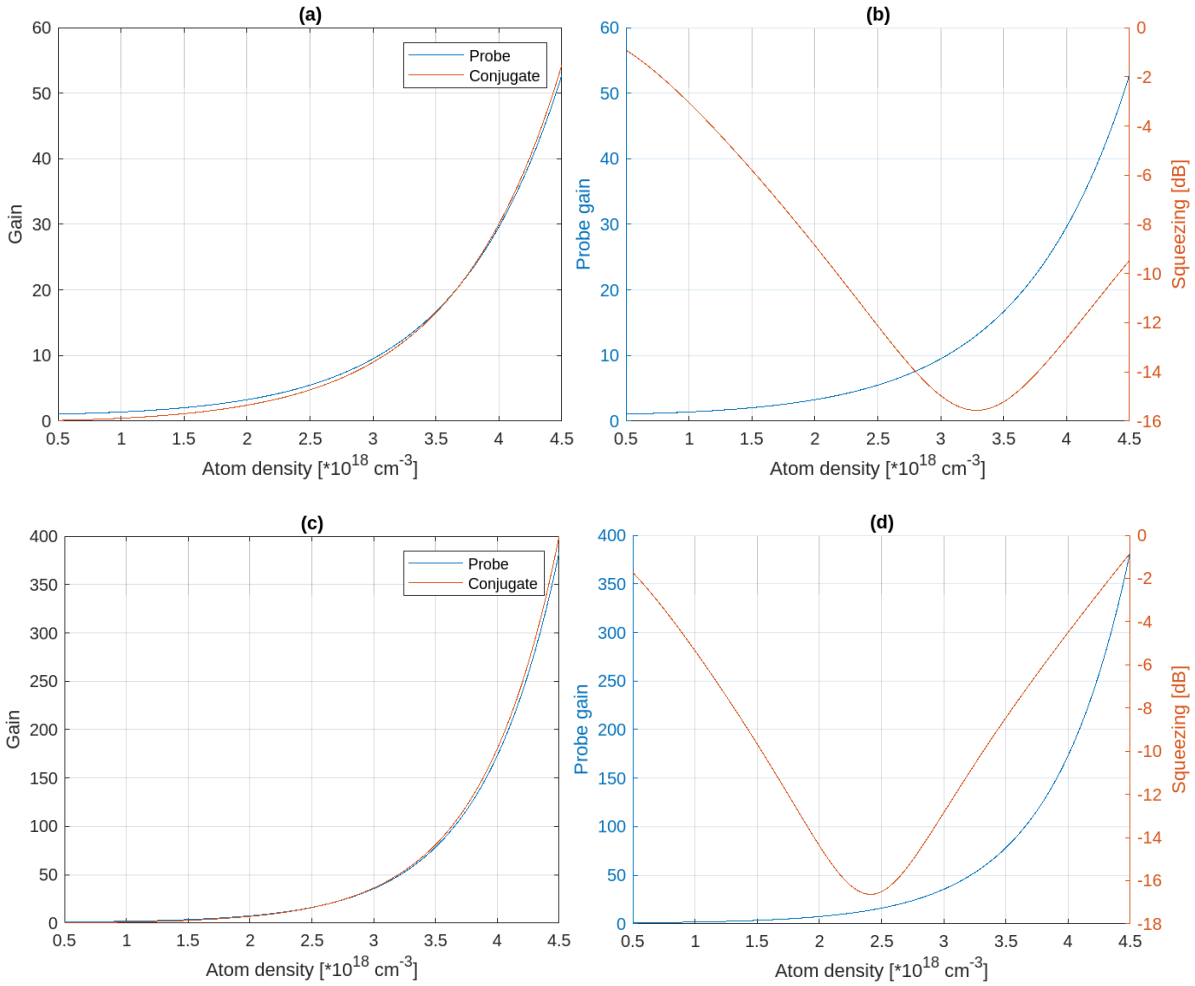


Figure 5.13 Calculated gains of the twin beams and the respective squeezing values as a function of atom density for (a)(b) $\Delta = 1.25$ GHz, and (c)(d) $\Delta = 0.6$ GHz. Other parameters are $\Omega = 1$ GHz, $\gamma_{deph} = 1 * 10^7$, $L = 10$ mm, $\Gamma = 6$ MHz, Hz, $\Gamma_t = 7.6 * 10^5$ Hz, $\gamma = 1 * 10^4$.

# 6. Experimental demonstration of the intensity difference squeezing by FWM in K

This chapter presents the results of the performed experimental study of two-mode relative intensity squeezing generated by the FWM in potassium vapour. In the first part, the upgrades and changes made on the experimental set-up employed in the classical study are described, followed by the characterization of the system in terms of the limitations imposed by the classical noise and ever-present losses in the detection. Finally, the obtained squeezing levels are shown and characterized as the function of the system parameters.

## 6.1. Experimental methods

### 6.1.1. Experimental set-up

The schematic of the experimental setup used to generate and measure the squeezing by FWM is shown in Figure 6.1. The first change we have made was in the laser system that we use. We wanted to have as much power as possible at the disposal, since high pump powers are needed to enhance the nonlinearity. Hence, we have changed the green pump laser employed for pumping Ti:Sa crystal of MBR laser with a 12 W VERDI G12 model, also at 532 nm. We were able to obtain up 750 mW of pump power, frequency stabilized at ~770 nm. The pump beam was sent through the set of lenses to obtain the beam diameter of 0.8 mm inside the cell. The probe was send thorough the single-mode polarization maintaining fibre in order to get better spatial profile and then with the telescope slightly focused with the waist of 0.5 mm at the intersection with the pump at the center of potassium cell. The probe and pump were orthogonally polarized, combined at Glan-Taylor (GT) polarizer. The phase-matching angle was set to 4 mrad. Another GT polarizer, placed after the cell, with the extinction ratio $10^5$: 1,, separates the beams, allowing only for the probe and the conjugate to pass to the detector. After the cell, the probe and the conjugate are sent to the balanced photodetector (Thorlabs PDB450A-AC), which subtract their respective photocurrents. It consists of two low noise diodes and transimpedance amplifier, Figure 6.2 [144]. With the two outputs (+/-) we can monitor the signals of the probe and conjugate individually. The gain of the amplification stage can be varied, which consequently limits the RF output bandwidth. Presented results were taken with the transimpedance gain of $10^5$ V/A that limits the bandwidth to 4 MHz. The signal difference is sent to the spectrum analyser (RSA607A Real-Time spectrum Analyser from Tektronix). All of the signal spectrums were recorded with the resolution bandwidth set to 3 kHz and video resolution of 30 Hz.

*New cell and the heating system*

The first squeezing was observed with the long uncoated Brewster cell, that was used in the study described in the Chapter 3. However, the results, in general, were poor, mainly due to the losses imposed on the beams in this system. Two problems with the potassium cell were realised, uncoated cell window, and the Brewster angled windows which significantly reduced the pump power. The measured gain profiles, Chapter 3, indicated a significant difference in the gain levels of the probe compared to the conjugate. As suggested by our model, this can lead to the low squeezing or no noise reduction at all. To address this problem, we replaced the cell in our experiment with the shorter one, 30 mm long, with flat antireflection (AR) coated windows, Figure 6.3 (a).

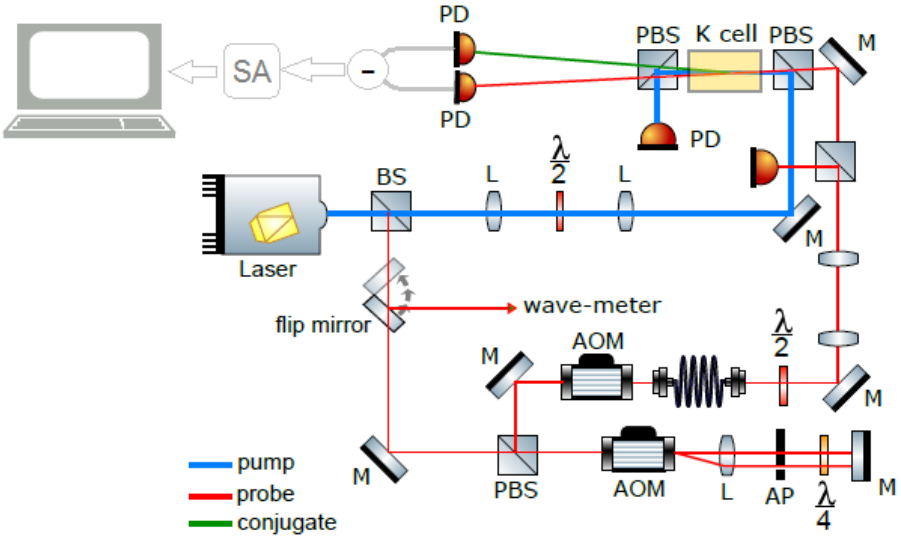


Figure 6.1 Slightly simplified schematic of the experimental set-up for relative-intensity squeezing by FWM in K. M - Mirror, L - Lens, PBS - Polarization beam splitter, AOM - Acousto-Optical Modulator, AP – Aperture, PD – Photodetector, SA- Spectrum analyser.

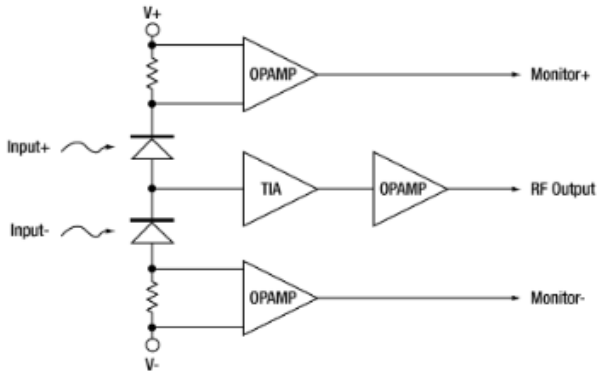


Figure 6.2 Functional block diagram of the balanced detector PDB450A-AC [144].

The initial measurements with the new cell revealed that the window transmission was getting lower over time due to deposition of potassium on the windows while cooling down the cell. Hence, we were in need of another design for the cell heating system. We kept the method of heating by the hot air, but find another way of heat distribution around the cell, in order to introduce different "cold point", away from the cell windows. The picture of a new design is shown in Figure 6.3(b). This time, hot air is being sent through the copper pipes mounted around the edges of the cell, making the middle of the wall the least heated spot during the cooling down process. The whole construction is again placed inside the isolating holder made of teflon. One of the thermistors, pt1000, is placed next the wall window, while the other is used to monitor the temperature of the copper plate holding the cell. For the temperature in the cell we recorded the mean value of the ones detected by these two thermistors.

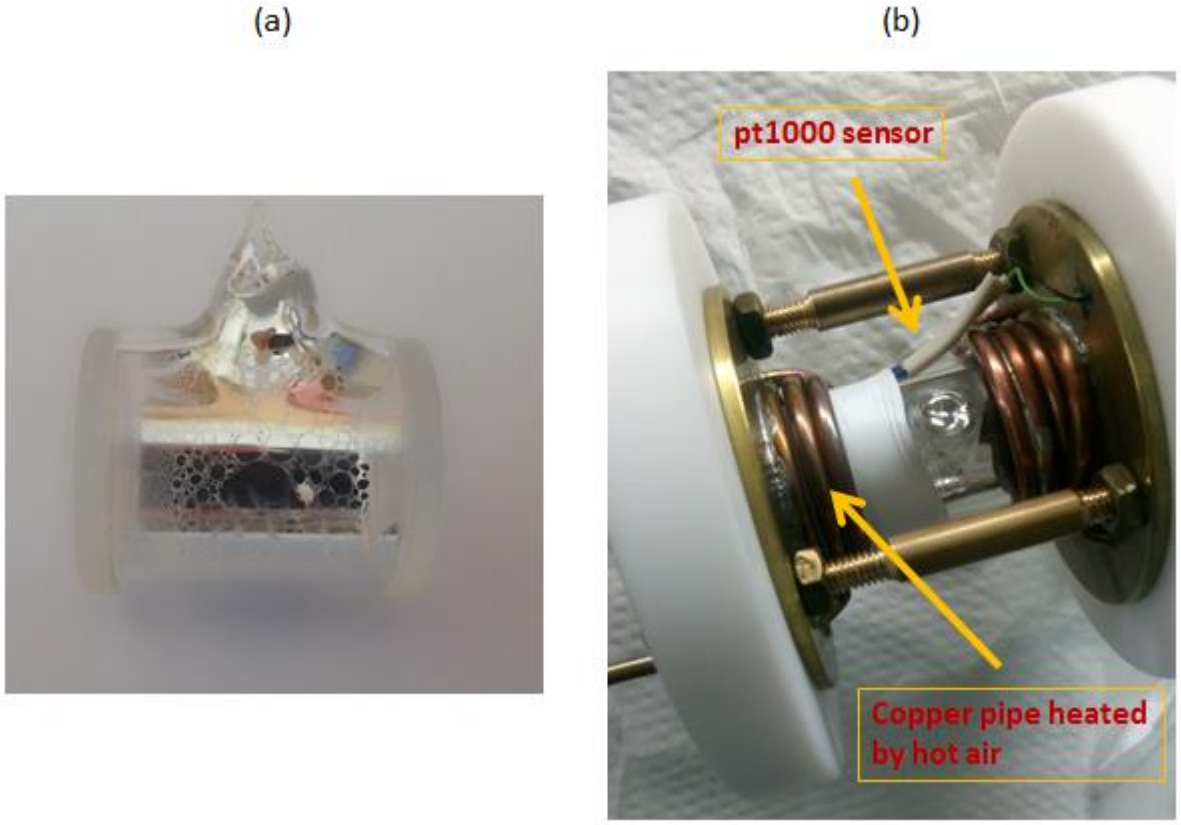


Figure 6.3 (a) Potassium cell with the flat AR coated windows. (b) New design of the cell heating.

### 6.1.2. Limitations of the system and SQL noise calibration

In order to determine the squeezing levels in our experiment, we have to compare the noise level of the probe and conjugate signals difference with the standard quantum limit (SQL). This reference noise level is defined by the shot noise of the coherent light source, the laser, used in the experiment. SQL is measured by the balanced homodyne detection. The probe seed beam is evenly split by $\lambda/2$ waveplate and polarizing beam splitter, and the obtained beams are sent to the balanced detector, as presented on the Figure 6.4(a). By balancing the powers of the beams reaching the detector, in the measured difference of the photocurrents, technical background noise and classical amplitude noise will cancel out. However, due to the quantum nature of the photons, quantum noise is still present. These recorded values quantify the SQL. In Figure 6.4(b) the results of the SQL calibration at 1.5 MHz, as a function of the total power, are presented. The electronic noise measured separately is subtracted from the measured signal difference.

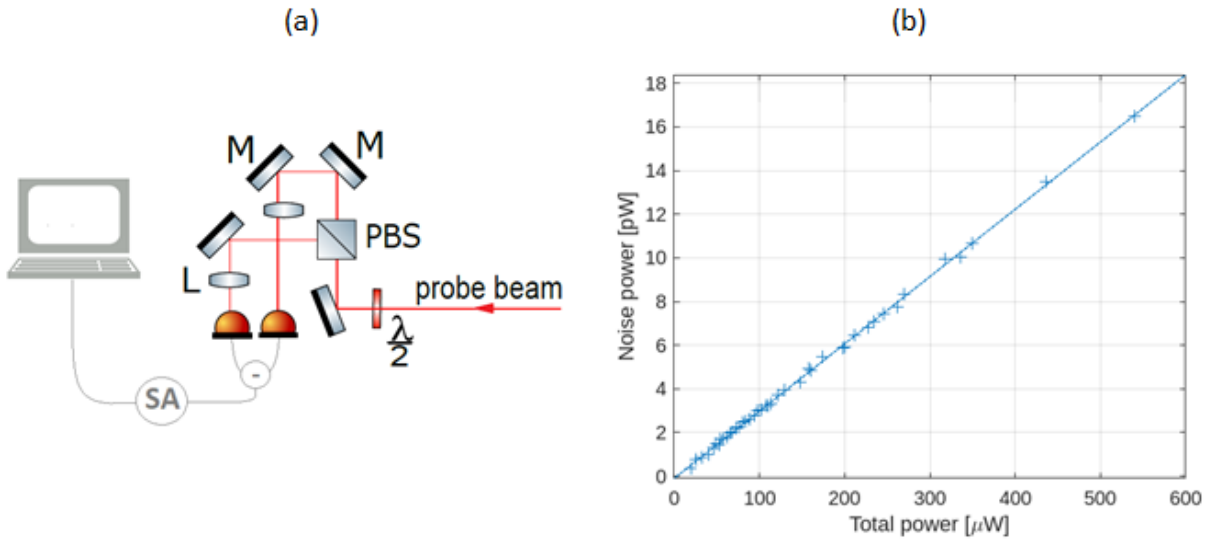


Figure 6.4 (a) Schematic of the setup used for SQL measurements. (b) SQL calibration @1.5 MHz as a function of total laser power, corrected for the electronic noise.

In Figure 6.5 the intensity noise spectrums of the probe seed, for the same seed power and different power of the VERDI, detected by the photodiode of the balanced detector, are presented. It can be noticed that the signal gets noisier at the frequencies below 1 MHz when we increase the power of VERDI, the source of both pump beam and seed probe in the experiment. This can be one of the limiting factors, if such operating conditions are needed, and one is focused on the lower frequency range. Since we could not find the way around this issue, the results that will be presented in this Chapter are measured at the frequencies above 1 MHz.

Important for reliable estimation of the level of relative intensity squeezing is the determination of optical and detection losses and their values. As previously noted, even though the losses induced by optical elements and by detection are unavoidable, it is vital that they are minimized. The cell windows are, as already mention, AR coated, resulting in the probe transmission of 0.98(5) per cell window. Losses of 0.08 are measured on the optics elements behind the cell, the beam splitter, the mirrors and the lenses. From the responsivity of 0.53 A/W, quantum efficiency of the balanced detector was estimated to be 0.85. This led to the total losses in detection of ~0.24. This value was later used to calculate expected levels of squeezing, utilizing phenomenological models explained in the previous chapter.

## 6.2. Results and discussion

In this section we present experimentally obtained results of the intensity difference squeezing by the FWM process in hot potassium vapour. We have investigated mechanisms of the noise reduction by considering dependence of squeezing on different FWM parameters, like one-photon detuning, two-photon probe detuning and vapour density. In addition, we compared the predicted levels of squeezing by the model of operators with the ones experimentally obtained.

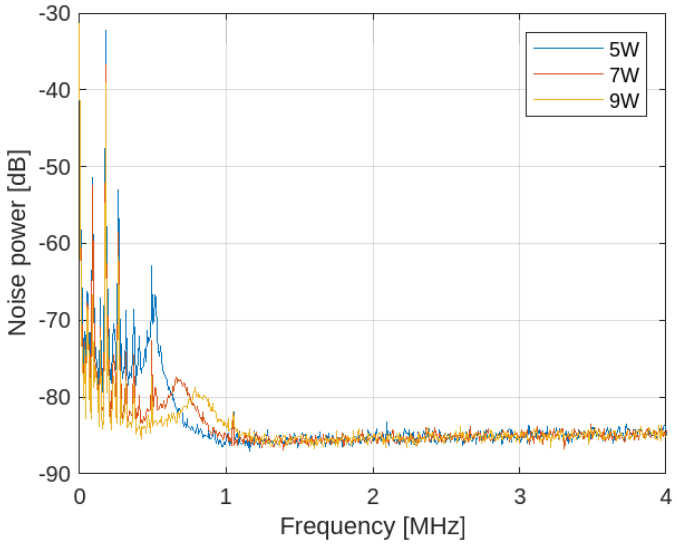


Figure 6.5 Measured noise intensity spectra of the probe seed for different powers of the VERDI.

The quantum correlation between the probe and conjugate beams is quantified by the noise spectra of the intensity difference, like the one presented in Figure 6.6. Figure shows the measured intensity noise of the individual beams, probe and conjugate, so as the intensity difference signal which is below the SQL. The plotted noise spectras are corrected for the electronic background noise and the pump leakage.

These results are obtained for $\Delta = 1.2$ GHz, $\delta = 6$ MHz, $T = 123\ ^{o}$C, and pump and probe powers of 750 and 6 $\mu$W, respectively. The measured gains of the probe and conjugate are 7.12 and 7,64, respectively. For this set of experimental parameters, squeezing is obtained in the frequency range between 0.9 MHz and 4.5 MHz, with the maximal value of -6.1 dB reached at 1.2 MHz. The squeezing bandwidth is defined on the lower frequency side by the system classical noise, as previously suggested, and on the high frequency by the RF output bandwidth of the detector, dependent on the output conversion gain. The contribution of the fraction of the pump reaching the detectors to the noise signal difference was determined by extrapolating SQL and probe-conjugate signal difference to zero power, and subtracting the former from the later. Note that the amount of the leaked pump noise is frequency dependent, and therefore it has to be evaluated at the frequency at which the results were reported. For the measurement results that follow, the pump power was kept at 700 mW, while the probe power was 6 $\mu$W. The values of squeezing are obtained from the noise spectra at the analysing frequency of 1.5 MHz. As it was suggested by the theoretical results, there is a strong mutual dependence of squeezing on all of the system parameters, hence, changing value of the one, requires the adjustments of the others for the maximal possible squeezing. Therefore, when investigating effects of experimental parameters, we change one at the time and measure the noise spectra of the difference between the probe and the conjugate. We test our system for a wide range of the variable parameters in order to obtain comprehensive and clearer picture of how these parameters affect noise reduction by FWM in K.

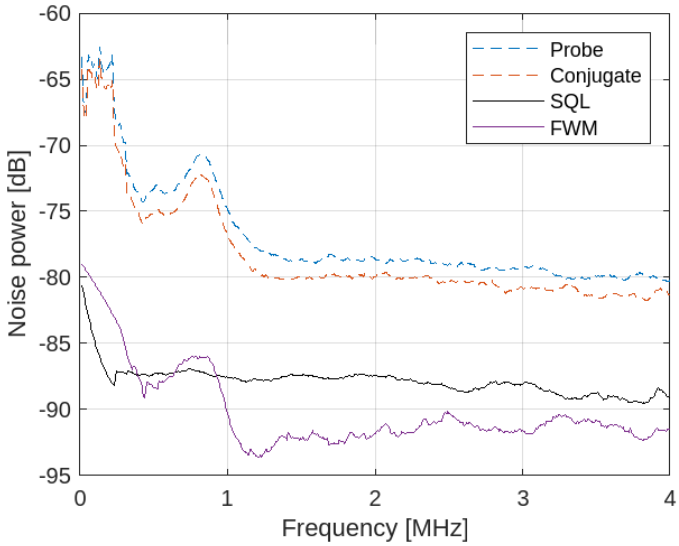


Figure 6.6 Measured spectral noise density for the probe-conjugate difference, the SQL, the probe and the conjugate, corrected for the pump leakage, at 123 $^{o}$C, for $\Delta$= 1.2 GHz, $\delta = 6$ MHz, $P_{pump} = 750$ mW, $P_{probe} = 6\ \mu$W.

*Dependence of gains and squeezing on one-photon pump detuning*

Figure 6.7 shows the squeezing dependence on the one-photon pump detuning $\Delta$, measured at three different cell temperatures. The two-photon probe-pump detuning was kept at $\delta = 0$ MHz. This choice of value for $\delta$ allowed the widest possible range of $\Delta$ at different temperatures for which the squeezing was observed. At 110 $^{o}$C, and potassium density of $1.52 * 10^{12}$ cm$^{-3}$, the best noise reduction is obtained at $\Delta = 0.75$ GHz, Figure 6.7(a). As the temperature increases to 114 $^{o}$C, Figure 6.7(b), and then to 118 $^{o}$C, Figure 6.7(c), the $\Delta$ for the maximum squeezing shifts to 0.95 GHz and 1.25 GHz, respectively. As the density increases, one photon detuning for the maximal squeezing has to be further detuned from the Doppler broaden absorption line, to reduce the probe and the conjugate absorption and scattering. Too large $\Delta$, on the other hand, means lower nonlinearity and reduced squeezing.

In Figure 6.7 the measured gains of the probe and conjugate are also presented. At lower temperature, of 110 $^{o}$C, the gain maximum and the maximum of noise reduction are obtained at the same value of the one-photon detuning. As temperature increases, maximum of squeezing also shifted to higher $\Delta$, and shifter therefore with respect to the gain maximum. These results are consistent with the microscopic model predictions, as presented in previous chapter. The model predicts the appearance of this frequency gap between the optimal parameter values for the gain and squeezing, when conjugate gain exceeds the probe gain, as it is the case for the results shown in Figure 6.7. One can also notice that for all vapour densities the maximal squeezing is at the similar and modest values of gains, around 3. Through this low probe and conjugate gains, the FWM system is, in fact, making the balance between too high absorption and associated noise amplification, at the higher gains, and too high seed probe power at the lower gains.

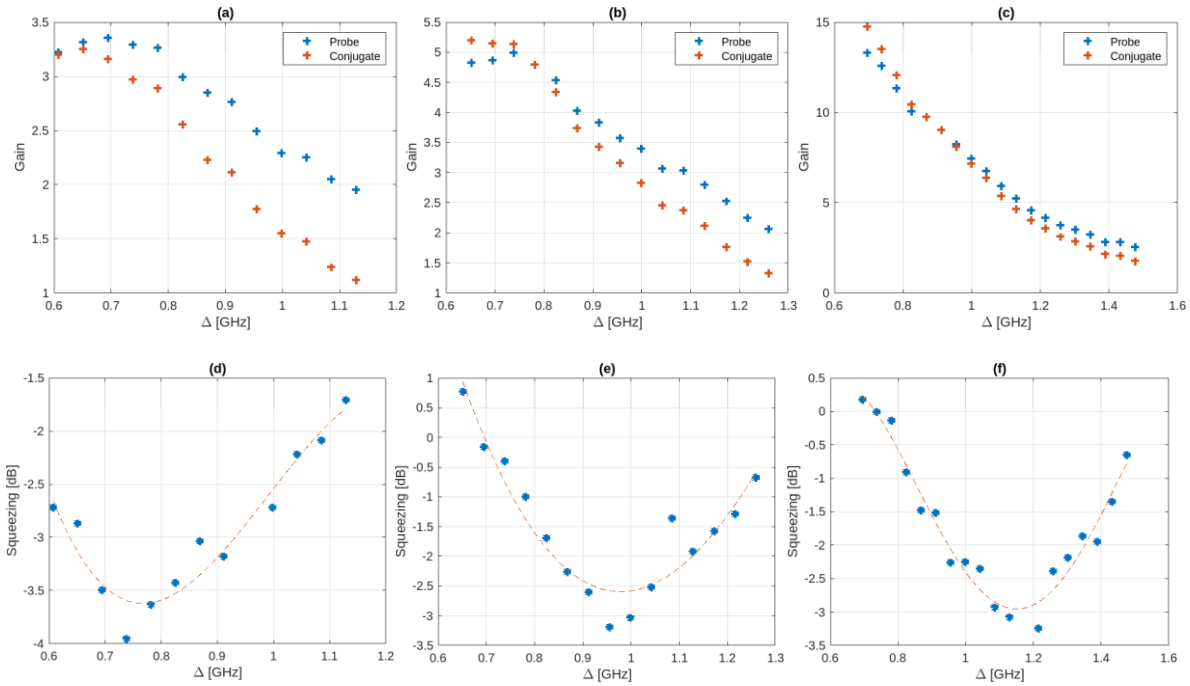


Figure 6.7 Gains of the probe and conjugate – top plots, and intensity difference squeezing – bottom plots, as a function of Δ at different cell temperatures (a) 110°C, (b) 114°C, (c) 118°C, for $\delta = 0\ MHz$, $P_{pump} = 700$ mW.

We were also interested in comparison of the behaviour of gains and squeezing levels in respect to FWM parameters, to those obtained with other alkali elements. The alignment of the gain and squeezing maximums observed in potassium at certain values of parameters was also observed in Rb [81,138] and Cs vapours [110]. The analytical interleaved gain-loss [138] and numerical [81] models also predicted quantum noise reduction with respect to the increase of gain. These models correctly show that the pump detuning affects classical and quantum properties in the same manner, when maximums for the gains and squeezing are at the same value of one-photon detuning. They correctly predict corrections of measured noise reduction when losses in twin beams transmission and detection are known. Then, squeezing resulted from FWM in the vapour can be predicted when detection efficiency is assumed to be $\eta = 1$. We have used these models, introduced in Chapter 5, in order to calculate squeezing as a function of one-photon detuning using the measured transmission losses and calculated detection efficiency. We have also employed the interleaved gain/loss model, as previously done by [81,82,110,138], to estimate the squeezing in an ideal case, with no losses in detection. Results obtained using the models from the Chapter 5 are presented in the Figure 6.8. The squeezing predicted by the model is stronger than our measured values. A couple of explanations can be found for this discrepancy. As suggested in [138] this could be due to the assumption in the model that the pump and the probe are fully overlapped in the entire cell, i.e. both gain and FWM coupling are considered uniform throughout the cell, which is not the case in the experiment. Also, losses on the probe and conjugate beams are similar at best, but are not equal. This comparison suggests that much larger squeezing in K is possible after adequate adjustments in the experiment, using different size of the cell and different phase matching angle between the pump and the probe. Calculated maximum of squeezing in the the ideal case with no losses in the transmission of twin beams after the cell and on the cell window, and for quantum efficiency η = 1 of the balanced detector, is -10.29 dB. This value for the intrinsic source squeezing is among the highest that this and similar models predicted for alkali atoms [81,82]. When gain and

squeezing maximums are at different Δ, phenomenological models do not agree with the experiment, not even qualitatively. Similarly, when maximum of noise reduction is shifted vis-à-vis maximum of twin beam gain, no agreement between the experiment and phenomenological model is found in [110].

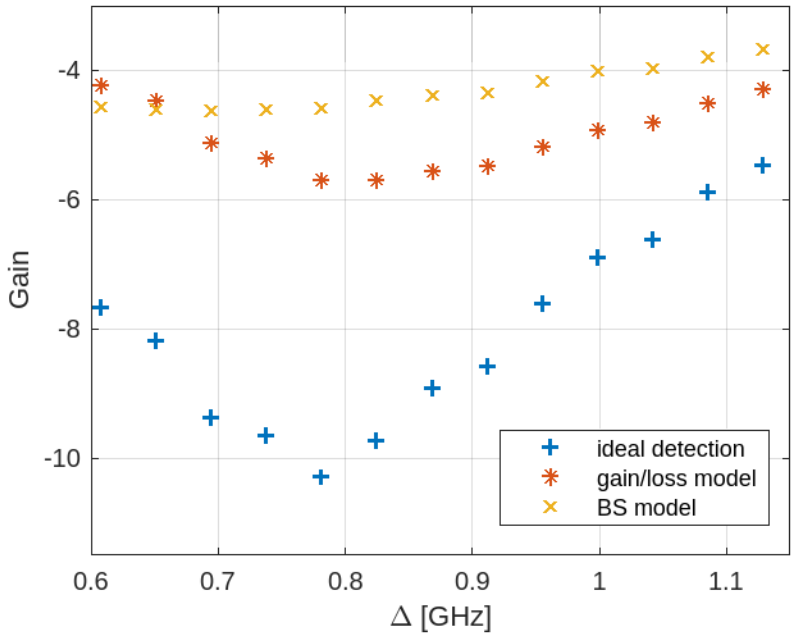


Figure 6.8 Squeezing vs one photon detuning - calculated results with detection losses and results for ideal detection by gain/loss model (blue pluses), under experimental conditions, with absorption and losses in detection (red circles), and with losses only in transmission by BS model (yellow circles), at 110°C, $\delta = 0\ MHz$, $P_{pump} = 700$ mW. $P_{probe} = 6\ \mu$W at 1.5 MHz. (b)

*Dependence of gains and squeezing on two-photon probe detuning*

FWM squeezing and gains of twin beams as a function of two-photon pump-probe detuning $\delta$, for two values of Δ, at temperature 121 °C are presented in Figure 6.9. The two-photon detuning for the maximum of squeezing is closer to the two-photon resonance, δ = 0, if Δ is higher, it is at ~10 MHz for Δ= 1.1 GHz, and at ~4 MHz when Δ= 1.3 GHz. Squeezing is only observed at the positive values of $\delta$, but away from the maximum of corresponding gain. This system behaviour agrees well with the model predictions, Figure 5.12. Also, note that for each Δ, the highest squeezing level is at the two-photon detuning at which the gains of twin beams are at low values, similar conclusion we draw from their dependences on one-photon detuning. Dependence on $\delta$, as dependence on Δ, places the highest levels of squeezing in the narrow range of respective detunings, where gains of twin beams are nearly equal and small.

The values for the highest level of measured squeezing vary both with the vapour density and Δ, as it was suggested by our model, Figure 5.12. This was demonstrated in Figure 6.10. Presented results are obtained at two different temperatures, 121 °C and 123 °C, for Δ= 0.85 GHz and Δ= 1.2 GHz, respectively. For these sets of experimental parameters, measured gains of the probe and conjugate are balanced and small where squeezing is at the maximum. It can be seen

from the Figure 6.9 and Figure 6.10 that for lower atom density the optimal conditions for noise reduction are obtained at smaller pump detuning. At higher temperatures it is necessary to detune the pump further from the Doppler profile to keep gains in desired narrow interval.

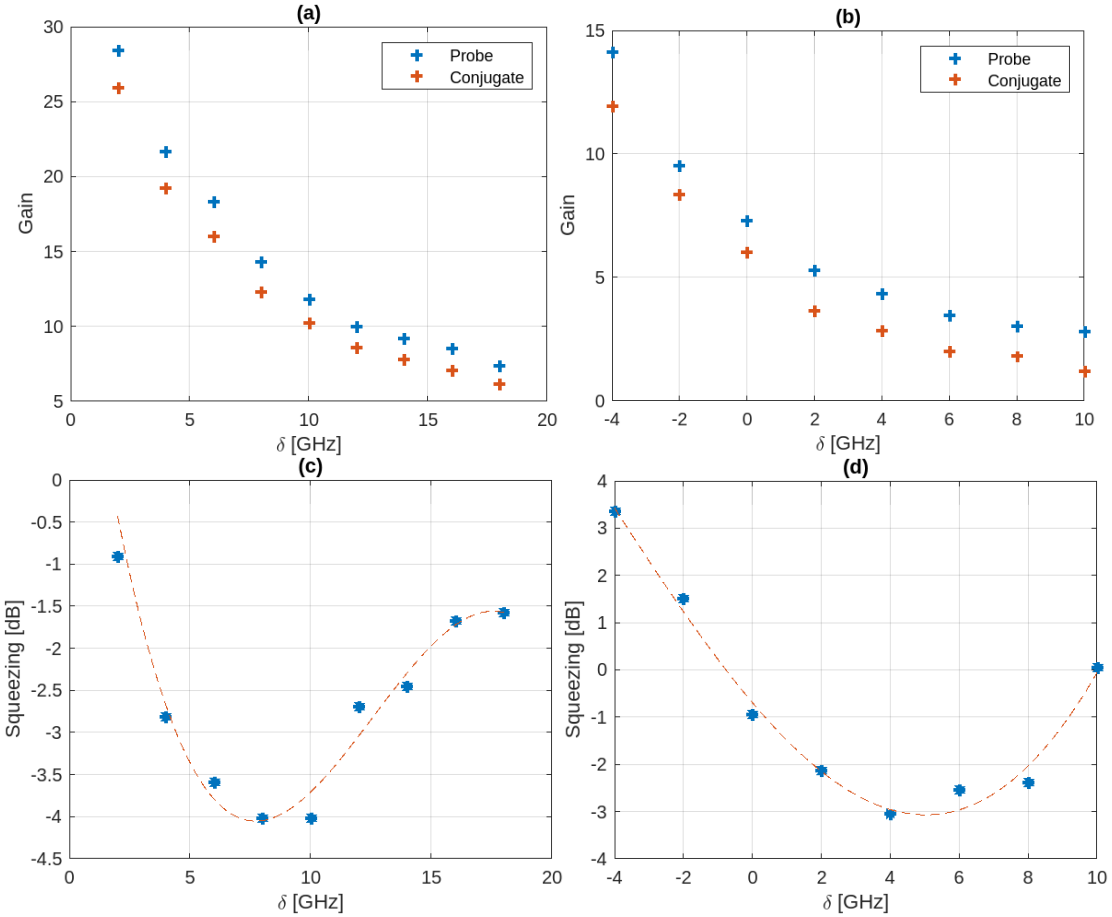


Figure 6.9 Gains of the probe and conjugate, and squeezing as a function of $\delta$ for (a),(c) $\Delta$= 1100 MHz, and (b)(d) $\Delta$= 1300 MHz, at 121°C, for $P_{pump} = 700$ mW. $P_{probe} = 6\ \mu$W.

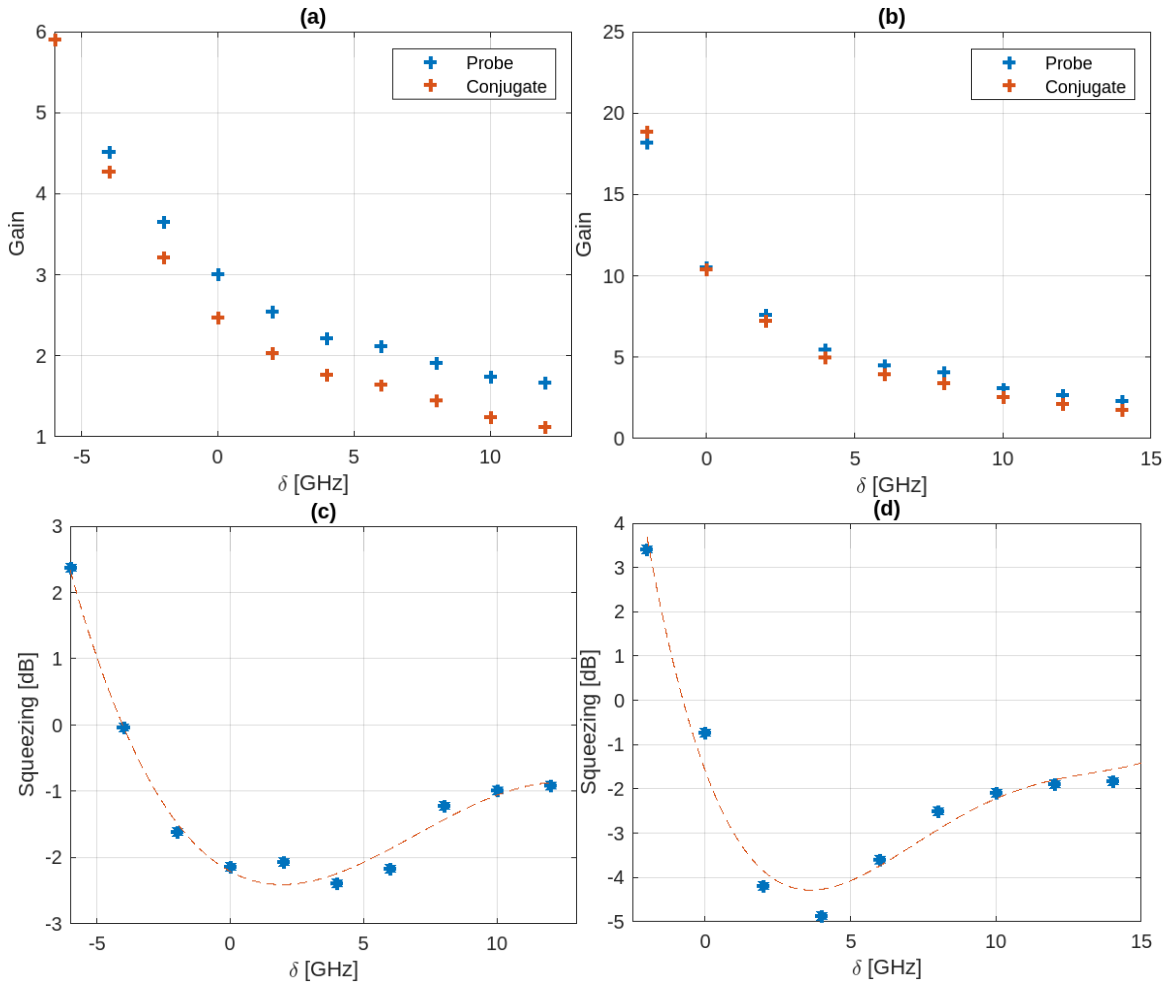


Figure 6.10 Gains of the probe and conjugate, and squeezing as a function of $\delta$ at different temperatures (a),(c) T=112°C $\Delta$= 850 MHz, and (b)(d) T=123°C $\Delta$= 1200 MHz, for $P_{pump} = 700$ mW. $P_{probe} = 6\ \mu$W.

*Dependence of gains and squeezing on the potassium cell temperature*

Dependence of squeezing on the temperature of potassium vapour is given in Figure 6.11. The results are for the range of temperatures from 110 °C to 125°C, corresponding to vapor densities from … to. Presented squeezing is for $\delta = 5$ MHz, and two values of one-photon detuning, $\Delta$= 1.1 GHz and $\Delta$= 1.2 GHz. We demonstrate a strong dependence of squeezing on the cell temperature, and that for the different combination of $\Delta$ and $\delta$, there is different optimal value of the density of potassium atoms needed for the best squeezing. Again, this result is in agreement with the microscopic model predictions, Figure 6.11.

In summary, we have demonstrated in both theoretical and experimental manner that FWM in K can be a source of strong relative intensity squeezing. The best squeezing in K, of – 6.1 dB, was obtained. In addition, we have studied the behaviour of the gains and squeezing as a function of various system parameters, and obtained good qualitative agreement of the measured results compared to our model predictions. The higher levels of the squeezing predicted by the model indicates that there is still room for the improvements in our experimental set-up.

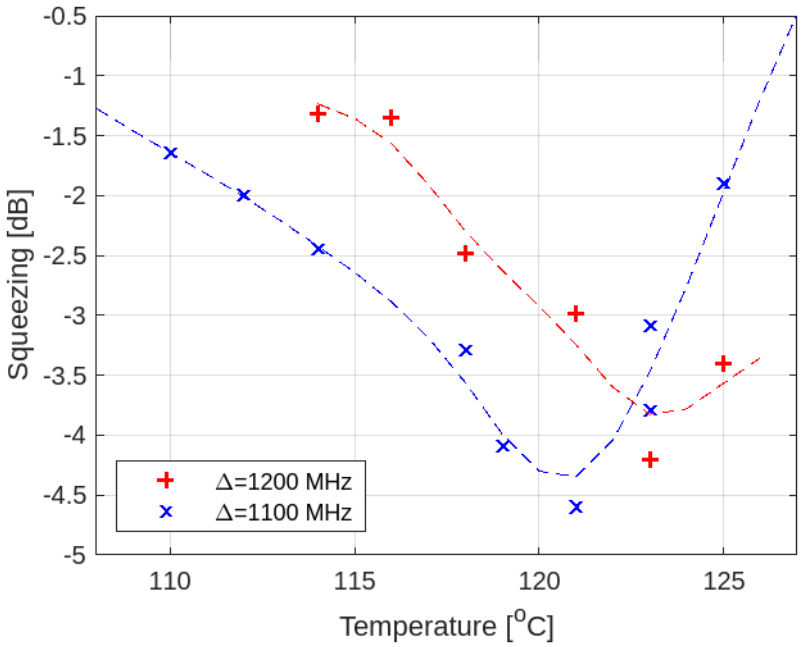


Figure. 6.11 Measured squeezing as a function of the cell temperature for Δ= 1100 MHz and Δ= 1200 MHz, when $\delta = 5\ MHz$, $P_{pump} = 700$ mW.

# 7. Conclusion

In this thesis we have described and explained the nonlinear effect of non-degenerate four-wave mixing in co-propagating beams configuration, realized in hot potassium vapour. We have performed an extensive study of the gains of the probe and conjugate by FWM as a function of system parameters and demonstrated that this system can act as a strong parametric amplifier with the gains of several hundreds, lager than observed for other alkali species under comparable conditions. This makes potassium competing element when it comes to the potential application in which this accumulated gain is of interest. We have learnt that for the highest amplifications one-photon detuning of the pump from $4S_{1/2},\ F = 1$ to $4P_{1/2}$ has to be shifted outside the Doppler broaden line. When it comes to the dependence on two-photon detuning, the optimal values lie in the narrow range, usually between -10 – 0 MHz. A strong sensitivity on other variables in the system, like atomic density, probe power and phase-matching condition, has also been demonstrated.

Beside the experimental work on the topic of the gain, we have performed complementary theoretical study. A semi-classical numerical model has been developed, and the results of the calculus have been compared to the measured ones. Good agreement has been obtained. In addition, by the use of the model, we were able to examine the effect of parameters whose values cannot be determined experimentally, like the contribution of the different relaxation mechanism and their effect on the results.

After we become familiar with the described FWM system in K, we were able to embark on another challenge and try to generate relative intensity squeezed light by the means of this nonlinear effect. We successfully demonstrated the noise reduction below standard quantum limit of -6.1 dB. These are the first-time measurements and analysis of FWM in potassium vapour, under certain atomic scheme that wasn't used before for this alkali element, which led to the higher degree of amplitude intensity squeezing. For a broad range of FWM parameters we have found that classical and quantum phenomena, gain and squeezing, can be in/out of sync with each other. We have discussed different analytical models in terms of qualitative and quantitative agreement with the experiments, as previously done for other alkalis. We found useful to test these models for potassium since it has quite different hyper-fine level splitting, much lower than Doppler broadening. We discussed our results, when and why, model and experiment agree or not. Our findings are complementary, but not always consistent with the ones reported experimentally and theoretically in Rb and Cs. Since it is not surprising that the models of operators do not always match with experiment as they are phenomenological, we have developed microscopic model based on Heisenberg-Langevin equations that makes a comprehensive analysis of the system, in terms of both gain and squeezing, possible. The relations between the gain and squeezing observed in the experiment, were also reproduced by the model. It is apparent that extensive experimental exploration of the whole parameter space is time consuming and demanding, hence, having a proper theoretical model can ease the choice of parameters' values, especially if some specific requirements are desired (or needed) by the future application of described system. By studying the system behaviour in response to the variation in the system parameters, we have acquired the knowledge that will enable us to implement such a new bright quantum light source for enhanced sensing and imaging.

# Bibliography


[1] Quantum optics and frontiers of physics: the third quantum revolution, A. Celi, A. Sanpera, V. Ahufinger and M. Lewenstein, Phys. Scr. 92 013003 (2017).

[2] Concerning an heuristic point of view toward the emission and transformation of light, A. Einstein, Annalen Phys. 17, 132–148 (1905).

[3] On the Law of Distribution of Energy in the Normal Spectrum, Max Planck, Annalen der Physik.4,553 (1901).

[4] Zur Theorie des Gesetzes der Energieverteilung im Normalspectrum, M.K.E.L. Planck, Verhandl. Dtsc. Phys. Ges. 2, 237 (1900).

[5] Stimulated Optical Radiation in Ruby, Maiman, T.H., Nature 187 , 493-494 (1960).

[6] Quantum technology: the second quantum revolution, Dowling J. P. and Milburn G. J., Phil. Trans. R. Soc. A. 3611655–1674 (2003).

[7] Optical quantum computing, J.L.O'Brien, Science, 318, 1567-1570 (2007).

[8] Generation of nonclassical photon pairs for scalable quantum communication with atomic ensembles, Kuzmich, A., Bowen, W., Boozer, A. et al., Nature 423, 731–734 (2003).

[9] Long-distance quantum communication with atomic ensembles and linear optics, Duan, L-M, et al., et al., Nature, 414, 413–418. (2001).

[10] Optical quantum memory, Lvovsky, A., Sanders, B. C. and Tittel, W. Nature Photonics, 3, 706–714 (2009).

[11] Quantum memory, Le Gouët, J-L. und Moiseev, S., J. Phys. B: At. Mol. Opt. Phys., 45, 120201 (2012).

[12] Optical quantum memory, Tittel , W., Sanders, B. C. und Lvovsky, A. I., Nature Photonics, 3, 706–714 (2009).

[13] 102ℏk Large Area Atom Interferometers, Chiow, S-wey, et al., et al., Phys. Rev. Lett., 107, 130403 (2011).

[14] Quantum sensing, C. L. Degen, F. Reinhard, and P. Cappellaro, Rev. Mod. Phys. 89, 035002 (2017).

[15] Long-Lived Solid-State Optica Memory for High-Rate Quantum Repeaters, M. F. Askarani, A. Das, J. H. Davidson, G. C. Amaral, N.Sinclair, J. A. Slater, S. Marzban,C. W. Thiel, R. L. Cone, D. Oblak, and W. Tittel, Phys. Rev. Lett. 127, 220502 (2021).

[16] Experimental Test of Bell's Inequalities Using Time-Varying Analyzers, A. Aspect, J. Dalibard, and G. Roger, Phys. Rev. Lett. 49, 1804 (1982).

[17] Experimental Entanglement Swapping: Entangling Photons That Never Interacted, J.-W. Pan, D. Bouwmeester, H. Weinfurter, and A. Zeilinger, Phys. Rev. Lett. 80, 3891 (1998).

[18] Direct Characterization of Ultrafast Energy-Time Entangled Photon Pairs, J-P. W. MacLean, J. M. Donohue, and K. J. Resch, Phys. Rev. Lett. 120, 053601 (2018).

[19] Einstein-Podolsky-Rosen Entanglement of Narrow-Band Photons from Cold Atoms, J.-C. Lee, K.-K. Park, T.-M. Zhao, and Y.-Ho Kim, Phys. Rev. Lett. 117, 250501 (2016).

[20] Generation and characterization of position-momentum entangled photon pairs in a hot atomic gas cell, Chengyuan Wang, Chung-Hyun Lee, and Yoon-Ho Kim, Optics Express 24, 34611-34617 (2019).

[21] Optimizing type-I polarization-entangled photons, Radhika Rangarajan, Michael Goggin, and Paul Kwiat, Optics Express , 17, 18920-18933 (2009).

[22] Entangled-Photon Imaging of a Pure Phase Object, Ayman F. Abouraddy, Patrick R. Stone, Alexander V. Sergienko, Bahaa E. A. Saleh, and Malvin C. Teich, Phys. Rev. Lett. 93, 213903 (2004).

[23] Entangled-photon compressive ghost imaging, Petros Zerom, Kam Wai Clifford Chan, John C. Howell, and Robert W. Boyd, Phys. Rev. A 84, 061804 (2011).

[24] Entangled Photon Spectroscopy, Audrey Eshun, Oleg Varnavski, Juan P. Villabona-Monsalve, Ryan K. Burdick, and Theodore Goodson, Acc. Chem. Res. 55, 7, 991–1003 (2022).

[25] Quantum Interferometric Optical Lithography: Exploiting Entanglement to Beat the Diffraction Limit, Agedi N. Boto, Pieter Kok, Daniel S. Abrams, Samuel L. Braunstein, Colin P. Williams, and Jonathan P. Dowling, Phys. Rev. Lett. 85, 2733 (2000).

[26] Quantum microscopy using photon correlations, Ashok Muthukrishnan, Marlan O Scully and M Suhail Zubairy, J. Opt. B: Quantum Semiclass. Opt. 6 575 (2004).

[27] Imaging with quantum states of light., Moreau, PA., Toninelli, E., Gregory, T. et al., Nat. Rev. Phys. 1, 367–380 (2019).

[28] A quantum-enhanced wide-field phase imager, Camphausen R, Cuevas Á, Duempelmann L, Terborg RA, Wajs E, Tisa S, Ruggeri A, Cusini I, Steinlechner F, Pruneri V., Sci Adv. 19 7(47) 2155. (2021).

[29] Quantum Enhanced Precision Estimation of Transmission with Bright Squeezed Light, G.S. Atkinson, E.J. Allen, G. Ferranti, A.R. McMillan, and J.C.F. Matthews, Phys. Rev. Applied 16, 044031 (2021).

[30] Squeezed-light-enhanced atom interferometry below the standard quantum limit Stuart S. Szigeti, Behnam Tonekaboni, Wing Yung S. Lau, Samantha N. Hood, and Simon A. Haine, Phys. Rev. A 90, 063630 (2014).

[31] Unconditional Quantum Teleportation. Furusawa, A., et al., et al., Science, S. 706-709 (1998).

[32] Teleportation with bright squeezed light. Ralph, T. C. und Lam, P. K., Phys. Rev. Lett., Bd. 81, S. 5668 (1998).

[33] Experimental demonstration of quantum teleportation of a squeezed state. Takei. N., et al., et al., Phys. Rev. A, Bd. 72, S. 042304 (2005).

[34] Quantum information with continuous variables, S. L. Braunstein and P. van Loock, Rev. Mod. Phys. 77, 513 (2005).

[35] Quantum Sensing with Squeezed Light, B. J. Lawrie, P. D. Lett, A. M. Marino, and R. C. Pooser, ACS Photonics 2019, 6, 1307–1318 (2019).

[36] Uber den anschaulichen Inhalt der quantentheoretischen Kinematik und Mechanik, W. Heisenberg, Z. Phys. 43, 172–198 (1927).

[37] Detection of amplitude modulation with squeezed light for sensitivity beyond the shot-noise limit. Xiao, M., Wu, L-A. und Kimble , H. J., Optics Letters, Bd. 13, S. 476-478 (1988).

[38] Two-color squeezing and sub-shot-noise signal recovery in doubly resonant optical parametric oscillators. Nabors, C. D. und Shelby, R. M. 1990, Phys. Rev. A, Bd. 42, S. 556.

[39] Spectroscopy with squeezed light. Polzik, E. S., Carri, J. und Kimble, H. J., Phys.Rev. Lett., Bd. 68, S. 3020-3023 (1992).

[40] Squeezed-light optical m agnetoinetry. Wolfgramm, F., et al., et al., Phys. Rev. Lett., Bd. 105, S. 053601 (2010).

[41] Quantum-enhanced magnetometer with low-frequency squeezing. Horrom, T., et al., et al., Phys. Rev. A., Bd. 86, S. 023803 (2012).
[42] Quantum Plasmonic Sensors, Changhyoup Lee, Benjamin Lawrie, Raphael Pooser, Kwang-Geol Lee, Carsten Rockstuhl, and Mark Tame, Chem. Rev., 121, 8, 4743–4804 (2021).
[43] Ultrasensitive measurement of microcantilever displacement below the shot-noise limit, Raphael C. Pooser and Benjamin Lawrie, Optica Vol. 2, 393-399 (2015).
[44] Improving sensitivity of an amplitude-modulated magneto-optical atomic magnetometer using squeezed light, Jiahui Li and Irina Novikova, J. Opt. Soc. Am. B 39, 2998-3003 (2022).
[45] Advanced LIGO: the next generation of gravitational wave detectors. Harry, G. M. und forthe LIGO Scientific Collaboration, Class. Quantum Grav., Bd. 27, S. 084006 (2010).
[46] Absorption spectroscopy at the ultimate quantum limit from single-photon states R Whittaker, C Erven, A Neville, M Berry, J L O'Brien, H Cable[1] and J C F Matthews, New J. Phys. 19 023013 (2017).
[47] Quantum-enhanced continuous-wave stimulated Raman scattering spectroscopy, Rayssa B. de Andrade, Hugo Kerdoncuff, Kirstine Berg-Sørensen, Tobias Gehring, Mikael Lassen, and Ulrik L. Andersen, Optica 7, 470-475 (2020).
[48] Boyd. R. W. Nonlinear Optics, New York: Academic, 2003.
[49] New High-Intensity Source of Polarization-Entangled Photon Pairs. Kwiat, P. G., et al., et al. Phys. Rev. Lett., 75, 4337–4341 (1995).
[50] Preparation and Storage of Frequency-Uncorrelated Entangled Photons from Cavity-Enhanced Spontaneous Parametric Downconversion. Zhang, H., et al., Nature Photonics, 5, 628–632 (2011).
[51] D. McKay, Potassium 5p Line Data, available online at http://fermionlattice.wdfiles.com/local–files/papers/5Pstructure, 2009.
[52] D. A. Steck, Rubidium 85 D Line Data, available online at https://steck.us/alkalidata/, 2008.
[53] D. A. Steck, Rubidium 87 D Line Data, available online at https://steck.us/alkalidata/, 2003.
[54] Atom based RF electric field sensing, Haoquan Fan, Santosh Kumar, Jonathon Sedlacek, Harald Kübler, Shaya Karimkashi and James P. Shaffer, J. Phys. B: At. Mol. Opt. Phys. 48 (2015).
[55] Budker, D., Romalis, M. Optical magnetometry. Nature Phys 3, 227–234 (2007).
[56] Nonlinear optical processes using electromagnetically induced transparency. Harris, S. E., Field, J. E. and Imamoglu, A. 64, Phys.Rev.Lett., Vol. 64, pp. 1107-1110 (1990).
[57] Electromagnetically induced absorption A. Lezama, S. Barreiro, and A. M. Akulshin, Phys. Rev. A 59, 4732 (1999).
[58] Coherent trapping of atomic populations. Gray, H. R., Whitley, R. M. and Stroud, Jr. C. R. , Opt.Lett., Vol. 3, pp. 218-220 (1978).
[59] Electromagnetically induced absorption due to transfer of population in degenerate two-level systems, C. Goren, A. D. Wilson-Gordon, M. Rosenbluh, and H. Friedmann, Phys. Rev. A 70, 043814 (2004).
[60] Electromagnetically induced transparency: Optics in coherent media, M. Fleischhauer, A. Imamoglu, and J. P. Marangos, Rev. Mod. Phys. 77, 633—673 (2005).
[61] Optimizing the Rydberg EIT spectrum in a thermal vapour, Hsuan-Jui Su, Jia-You Liou, I-Chun Lin, and Yi-Hsin Chen, Optics Express, 30, 1499-1510, (2022)

[62] Coherent Optical Detection of Highly Excited Rydberg States Using Electromagnetically Induced Transparency, A. K. Mohapatra, T. R. Jackson, and C. S. Adams, Phys. Rev. Lett. 98, 113003 (2007).

[63] A room-temperature single-photon source based on strongly interacting Rydberg atoms, Fabian Ripka, Harald Kübler, Robert Löw, and Tilman Pfau, Science, 362, 446-449 (2018).

[64] Spectroscopy of the D1 transition of cesium by dressed-state resonance fluorescence from a single (In,Ga)As/GaAs quantum dot S. M. Ulrich, S. Weiler, M. Oster, M. Jetter, A. Urvoy, R. Löw, and P. Michler, Phys. Rev. B 90, 125310 ( 2014).

[65] Enhanced intensity difference squeezing with a low gain off-resonant Four-Wave Mixing in potassium vapour, M. M. Curcic, B. M. Jelenkovic, Optics Communications, 533 , 129301 (2023).

[66] J. Okuma, N. Hayashi, A. Fujisawa and Masaharu Mitsunaga, Opt. Lett. 11, 1654–1656 (2009).

[67] V. Boyer, C. F. McCormick, E. Arimondo, and P. D. Lett, Phys. Rev. Lett. 99, 143601 (2007).

[68] V. Boyer, A. M. Marino, R. C. Pooser, Science 321, 544–547 (2008).

[69] Four-wave mixing in optical fibers: exact solution, Yijiang Chen, J. Opt. Soc. Am. B 6, 1986-1993 (1989).

[70] Slowing 80-ns light pulses by four-wave mixing in potassium vapour, D. Arsenović, M. M. Ćurčić, T. Khalifa, B. Zlatković, Ž. Nikitović, I. S. Radojičić, A. J. Krmpot, and B. M. Jelenković, Phys. Rev. A 98, 023829 (2018)

[71] Slow light in paraffin-coated Rb vapour cells, M. Klein, I. Novikova, D. F. Phillips & R. L. Walsworth, Journal of Modern Optics, 53:16-17, 2583-2591 (2006).

[72] Four-wave-mixing stopped light in hot atomic rubidium vapour, Camacho, R., Vudyasetu, P. & Howell, J., Nature Photon 3, 103–106 (2009).
Resonant four-wave mixing with slow light, Hoonsoo Kang, Gessler Hernandez, and Yifu Zhu, Phys. Rev. A 70, 061804 (2004)

[73] Ultraslow matched-pulse propagation in sodium vapor , Junji Okuma, Nobuhito Hayashi, Akihiko Fujisawa, and Masaharu Mitsunaga, Optics Letters 34, 1654-1656 (2009).

[74] Quantum squeezing and entanglement from a two-mode phase-sensitive amplifier via four-wave mixing in rubidium vapour, Yami Fang and Jietai Jing, New J. Phys. 17 023027 (2015).

[75] M. M. Curcic, T. Khalifa, B. Zlatkovic, I. S. Radojicic, A. J. Krmpot, D. Arsenovic, B. M. Jelenkovic, and M. Gharavipour, Phys. Rev. A 97, 063851 (2018).

[76] F. Song, Z. Wang, E. Li, Z. Huang, B. Yu, B. Shi, Appl. Phys. Lett., 119 (2), 024101 (2021).

[77] Enhancement of phase conjugation degenerate four-wave mixing using a Bessel beam, Qian Zhang, Xuemei Cheng, Haowei Chen, Bo He, Zhaoyu Ren, Ying Zhang, and Jintao Bai, Photon. Res. 6, 162-167 (2018).

[78] X. Pan, S. Yu, Y. Zhou, K. Zhang, K. Zhang, S. Lv, S. Li, W. Wang, and J. Jing, Phys. Rev. Lett. 123, 070506 (2019).

[79] K. Zhang, W. Wang, S. Liu, X. Pan, J. Du, Y. Lou, S. Yu, S. Lv, N. Treps, C. Fabre, and J. Jing, Phys. Rev. Lett. 124, 090501 (2020).

[80] C. F. McCormick, A. M. Marino, V. Boyer, and P. D. Lett, Phys. Rev. A 78, 043816 (2008).

[81] Q. Glorieux, L. Guidoni, S. Guibal, J.-P. Likforman, and T. Coudreau, Proc. SPIE 7727, 772703 (2010).
[82] Polarization-based truncated SU(1,1) interferometer based on four-wave mixing in Rb vapor Nikunjkumar Prajapati and Irina Novikova, Optics Letters 44, 5921-5924 (2019)
[83] Combinations of orbital angular momentum in two degenerate four-wave mixing processes in Rb vapour, M R L da Motta, A A C de Almeida and S S Vianna, J. Opt. 25 095501 (2023).
[84] Manipulation of the orbital angular momentum via four-wave mixing in Rb vapour, Ning Liu, Xuewen Wang, Jinpeng Yuan, Liantuan Xiao, Suotang Jia and Lirong Wang' Laser Phys. Lett. 20, 035204 (2023).
[85] Orbital-Angular-Momentum Multiplexed Continuous-Variable Entanglement from Four-Wave Mixing in Hot Atomic Vapor Xiaozhou Pan, Sheng Yu, Yanfen Zhou, Kun Zhang, Kai Zhang, Shuchao Lv, Sijin Li, Wei Wang, and Jietai Jing, Phys. Rev. Lett. 123, 070506 (2019).
[86] Narrow Band Source of Transform-Limited Photon Pairs via Four-Wave Mixing in a Cold Atomic Ensemble, Bharath Srivathsan, Gurpreet Kaur Gulati, Brenda Chng, Gleb Maslennikov, Dzmitry Matsukevich, and Christian Kurtsiefer, Phys. Rev. Lett. 111, 123602 (2013).
[87] Polarization entanglement and quantum beats of photon pairs from four-wave mixing in a cold $^{87}$Rb ensemble, Gurpreet Kaur Gulati, Bharath Srivathsan, Brenda Chng, Alessandro Cerè and Christian Kurtsiefer, New J. Phys. 17 093034 (2015).
[88] An, H., Owens, H., Ather, H. et al. Intensity instability and correlation in amplified multimode wave mixing. Sci Rep 12, 14784 (2022).
[89] Multimode four-wave mixing with a spatially structured pump, Jon D. Swaim, Erin M. Knutson, Onur Danaci, and Ryan T. Glasser, Optics Letters 43, 2716-2719 (2018).
[90] Entangled Images from Four-Wave Mixing, Vincent Boyer, Alberto M. Marino, Raphael C. Pooser, and Paul D. Lett, Science, 321, 544-547 (2008).
[91] Observation of Squeezed States Generated by Four-Wave Mixing in an Optical Cavity. Slusher, R. E., et al., et al., Phys. Rev. Lett, 788–788 (1986).
[92] Bright squeezed light from a singly resonant frequency doubler. Paschotta, R., et al., et al., Phys. Rev. Lett., Bd. 72, S. 3807 (1994).
[93] The Optical Kerr Effect and Quantum Optics in Fibers. Sizmann, A. und Leuchs, G., Progress in Optics, Bd. 39, S. 373-469 (1999).
[94] Experimental evidence for Raman-induced limits to efficient squeezing in optical fibers. Dong, R., et al., et al., Optics Letters, Vol. 33, pp. 116-118 (2008).
[95] Squeezed light at 1550 nm with a quantum noise reduction of 12.3 dB. Mehmet, M., et al., et al., Optics Express, Vol. 19, pp. 25763-25772 (2011).
[96] Quantum-nondemolition measurements using cold trapped atoms: Comparison between theory and experiment. Sinatra, A., et al., et al., Phys. Rev. A, Bd. 57, S. 2980 (1998).
[97] Cold atoms: A new medium for quantum optics. Lambrecht, L., et al., Applied Physics B, Bd. 60, S. 129–134 (1995).
[98] R. C. Pooser, A. M. Marino, V. Boyer, K. M. Jones, and P. D. Lett, Opt. Express 17, 16722–16730 (2009).
[99] S. Kim and A. M. Marino, Opt. Express 26, 33366–33375 (2018).

[100] Quadrature squeezed light generation by cross-phase modulation in semiconductors. Fox, A. M., et al., Optics Letters, Bd. 24, S. 2523-2525 (1995).
[101] Experimental vacuum squeezing in rubidium vapor via self-rotation. Ries, J., Brezger, B. und Lvovsky, A. I., Phys. Rev. A, Bd. 68, S. 025801 (2003).
[102] Polarization squeezing of light by single passage through an atomic vapor. Barreiro, S., et al., Phys. Rev. A, Bd. 84, S. 033851 (2011).
[103] A. Lvovsky, Squeezed light, Photonics Volume 1: Fundamentals of Photonics and Physics, 121–164, (2015).
[104] Increasing the Astrophysical Reach of the Advanced Virgo Detector via the Application of Squeezed Vacuum States of Light, F. Acernese et al. (Virgo Collaboration), Phys. Rev. Lett. 123, 231108 ( 2019).
[105] Multimode entanglement generation with dual-pumped four-wave-mixing of Rubidium Atoms, Yin Cai, Ling Hao, Da Zhang, Yang Liu, Binshuo Luo, Zhan Zheng, Feng Li, and Yanpeng Zhang, fox, Vol. 28, 25278-25292 (2020).
[106] Dorfman, K., Liu, S., Lou, Y., Wei, T.,Jing, J.,Schlawin, F, Mukamel, S. Multidimensional Four-Wave Mixing Signals Detected by,Quantum Squeezed Light. Proc. Natl. Acad. Sci. U.S.A., 118, No. e2105601118 (2021).
[107] Observation of squeezed states with strong photon-number oscillations, Moritz Mehmet, Henning Vahlbruch, Nico Lastzka, Karsten Danzmann, and Roman Schnabel, Phys. Rev. A 81, 013814 (2010).
[108] C. Liu, J. Jing, Z. Zhou, R.C. Pooser, F. Hudelist, L. Zhou, W. Zhang, Opt. Lett. 36 2979–2981 (2011).
[109] M. Guo, H. Zhou, D. Wang, J. Gao, J. Zhang, S. Zhu, Phys. Rev. A 89, 033813 (2014).
[110] R. Ma, W. Liu, Z. Qin, X. Jia, J. Gao, Phys. Rev. A 96, 043843 (2017).
[111] J.D. Swaim, R.T. Glasser, Phys. Rev. A 96, 033818 (2017).
[112] D. Zhang, C. Li, Z. Zhang, Y. Zhang, Y. Zhang, M. Xiao, Phys. Rev. A 96, 043847 (2017).
[113] L. Cao, J. Du, J. Feng, Z. Qin, A.M. Marino, M.I. Kolobov, J. Jing, Opt. Lett. 42, 1201–1204 (2017).
[114] S. Liu, H. Wang, J. Jing, Phys. Rev. A 97, 043846 (2018).
[115] H. Wang, C. Fabre, J. Jing, Phys. Rev. A 95, 051802(R) (2017).
[116] X. Pan, H. Chen, T. Wei, J. Zhang, A.M. Marino, N. Treps, R.T. Glasser, J. Jing, Phys. Rev. B 97, 161115(R) (2018).
[117] Generation of tripartite squeezed state by cascaded four-wave mixing in single hot rubidium atomic system, Changbiao Li, Yufeng Li, Wei Li, Kangkang Li, Yuliang Liu, Yin Cai, and Yanpeng Zhang, New J. Phys. 24 093022 (2022).
[118] C. J. Foot. Atomic physics. Oxford master series in physics. Oxford University Press (2005).
[119] K. Blum. Density Matrix Theory and Applications. Springer Series on Atomic, Optical, and Plasma Physics. Springer Berlin Heidelberg (2012).
[120] A. M. Fox, M. Fox, D. Fox, and O. U. Press. Quantum Optics: An Introduction. Oxford Master Series in Physics. OUP Oxford (2006).
[121] A short introduction to the Lindblad master equation. D. Manzano, AIP Adv. 10, 025106 (2020).
[122] Analytic solutions of the optical Bloch equations, H.-R. Noh and W. Jhe, Opt. Commun. 283, 2353 (2010),

[123] Properties of Potassium, T.G. Tiecke, https://www.tobiastiecke.nl/archive/PotassiumProperties.pdf
[124] A high-performance Raman-Ramsey Cs vapor cell atomic clock, Moustafa Abdel Hafiz,Grégoire Coget,Peter Yun , Stéphane Guérandel, Emeric de Clercq, Rodolphe BoudotJournal of Applied Physics 121, 104903 (2017).
[125] Efficient parametric non-degenerate four-wave mixing in hot potassium vapour, B Zlatković,A J Krmpot, N Šibalić, M Radonjić and B M Jelenković , Laser Phys. Lett. 13 015205 (2016).
[126] C. Alcock, V. Itkin, and M. Horrigan, Vapour pressure equations for the metallic elements: 298–2500k, Canadian Metallurgical Quarterly, vol. 23, no. 3, pp. 309–313, (1984).
[127] P. Van der Straten and H. Metcalf, Atoms and molecules interacting with light: Atomic physics for the laser era. Cambridge University Press, 2016.
[128] R. Loudon, The Quantum Theory of Light (OUP, Oxford, 2000), 3rd ed.
[129] H. Breuer and F. Petruccione, The Theory of Open Quantum Systems (OUP, Oxford,2002).
[130] Quantum theory of nonlinear mixing in multimode fields: General theory,G. S. Agarwal, Phys. Rev. A 34, 4055 (1986).
[131] P. D. Maker, R. W. Terhune, M. Niseno, and C. M. Savage, Effects of dispersion and focusing on the production of optical harmonics," Phys. Rev. Lett. 8, 21 (1962).
[132] Role of the phase-matching condition in nondegenerate four-wave mixing in hot vapors for the generation of squeezed states of light, M. T. Turnbull, P. G. Petrov, C. S. Embrey, A. M. Marino, and V. Boyer, Phys. Rev. A 88, 033845 ( 2013).
[133] Resonant Enhancement of Parametric Processes via Radiative Interference and Induced Coherence M. D. Lukin, P. R. Hemmer, M. Löffler, and M. O. Scully,Phys. Rev. Lett. 81, 2675 (1998).
[134] Q. Glorieux, R. Dubessy, S. Guibal, L. Guidoni, J. P. Likforman, T. Coudreau, and E. Arimondo, Phys. Rev. A 82, 033819 (2010).
[135] P. Kolchin, Phys. Rev. A 75, 033814 (2007).
[136] https://www.coherent.com/scientific/titanium-sapphire-lasers.
[137] Double-pass acousto-optic modulator system, E. A. Donley, T. P. Heavner, F. Levi, M. O. Tataw, and S. R. Jefferts, Rev. Sci. Instrum. 76, 063112 (2005).
[138] Bojan V. Zlatkovic, Four wave mixing in hot potassium, PhD Thesis, University of Belgrade, (2022).
[139] M. Jasperse, L. D. Turner, and R. E. Scholten, "Relative intensity squeezing by four-wave mixing with loss: an analytic model and experimental diagnostic," Opt. Express 19, 3765-3774 (2011).
[140] Scully, Marlan O.and M. Suhail Zubairy, Quantum Optics. Cambridge: Cambridge University Press (1997).
[141] Jon Sagle, RK Namiotka, and John Huennekens. Measurement and modelling of intensitydependent absorption and transit relaxation on the cesium line. Journal of Physics B: Atomic,Molecular and Optical Physics, 29(12):2629 (1996).
[142] Claude Fabre. Quantum fluctuations in light beams. Les Houches Session LXIII, June 27 - July 28, 1995., (1997).
[143] Quentin Glorieux. Etude theorique et experimentale des correlations quantiques obtenues par melange a quatre ondes dans une vapeur atomique. PhD thesis, 2010.

[144] https://www.thorlabs.com/thorproduct.cfm?partnumber=PDB450A-AC

**Биографски подаци**

Марија Ћурчић је рођена 12.08.1991. године у Краљеву. Изабрана је за ђака генерације након завршене основне школе. Уписала је Математичку гимназију у Краљеву, коју је завршила као носилац Вукове дипломе. У основној и средњој школи учествовала је на републичким такмичењима из математике и физике. Електротехнички факултет је уписала 2010. године. Дипломирала је на одсеку за Физичку електронику, смер Наноелектроника, оптоелектроника и ласерска техника, 2015. године са укупном просечном оценом 8.89, и оценом 10 на завршном раду на тему "Косимулација између Matlab-a и OptiSystem-a на примеру рефлексионих полупроводничких оптичких појачавача". Дипломске академске – мастер студије на Електротехничком факултету у Београду, на модулу за Наноелектронику и фотонику уписала је у октобру 2015. године. Положила је све испите са просечном оценом 10 и одбранила мастер рад, одрађен у Лабораторији за атомску и квантну физику Центра за фотонику Института за физику, на тему "Нелинеарна спектроскопија у пари калијума" са оценом 10.

У октобру 2016. године започиње докторске студије на Електротехничком факултету у Београду, на модулу Наноелектроника и фотоника. Од новембра 2016. је запослена у Центру за фотонику Института за физику у Београду, а од 2020. И завађу истаживач сарадник. Тренутно је ангажована је на више мађународних пројеката из области оптичке магнетометрије и квантне биофотонике. Коаутор је на три рада категорије М21 и једном категорије М22.

На јавној усменој одбрани одржаној 10.10.2019. на Електротехничком факултету у Београду одобрена јој је тема докторске дисертације под називом „Примена квантних и нелинеарних феномена у пари калијума за контролу особина ласерског зрачења”.

*образац изјаве о ауторству*

# Изјава о ауторству

Име и презиме аутора Марија Ћурчић

Број индекса 5014/2016

**Изјављујем**

да је докторска дисертација под насловом

Application of nonlinear and quantum phenomenon in hot potassium vapour for controling properties of laser radiation

- резултат сопственог истраживачког рада;
- да дисертација у целини ни у деловима није била предложена за стицање друге дипломе према студијским програмима других високошколских установа;
- да су резултати коректно наведени и
- да нисам кршио/ла ауторска права и користио/ла интелектуалну својину других лица.

**Потпис аутора**

У Београду, 31.8.2023

Ћурчић

# Изјава о истоветности штампане и електронске верзије докторског рада

Име и презиме аутора Марија Ћурчић

Број индекса 5014/2016

Студијски програм Наноелектроника и фотоника

Наслов рада Application of nonlinear and quantum phenomenon in hot potassium vapour for controling properties of laser radiation

Ментор др Бранислав Јеленковић

Изјављујем да је штампана верзија мог докторског рада истоветна електронској верзији коју сам предао/ла ради похрањивања у **Дигиталном репозиторијуму Универзитета у Београду.**

Дозвољавам да се објаве моји лични подаци везани за добијање академског назива доктора наука, као што су име и презиме, година и место рођења и датум одбране рада.

Ови лични подаци могу се објавити на мрежним страницама дигиталне библиотеке, у електронском каталогу и у публикацијама Универзитета у Београду.

**Потпис аутора**

У Београду, 31.8.2023.

*образац изјаве о коришћењу*

# Изјава о коришћењу

Овлашћујем Универзитетску библиотеку „Светозар Марковић“ да у Дигитални репозиторијум Универзитета у Београду унесе моју докторску дисертацију под насловом:

Application of quantum and nonlinear phenomenon in hot potassim vapour for controling properties of laser radiation

која је моје ауторско дело.

Дисертацију са свим прилозима предао/ла сам у електронском формату погодном за трајно архивирање.

Моју докторску дисертацију похрањену у Дигиталном репозиторијуму Универзитета у Београду и доступну у отвореном приступу могу да користе сви који поштују одредбе садржане у одабраном типу лиценце Креативне заједнице (Creative Commons) за коју сам се одлучио/ла.

1. Ауторство (CC BY)

2. Ауторство – некомерцијално (CC BY-NC)

3. Ауторство – некомерцијално – без прерада (CC BY-NC-ND)

4. Ауторство – некомерцијално – делити под истим условима (CC BY-NC-SA)

5. Ауторство – без прерада (CC BY-ND)

6. Ауторство – делити под истим условима (CC BY-SA)

(Молимо да заокружите само једну од шест понуђених лиценци.
Кратак опис лиценци је саставни део ове изјаве).

**Потпис аутора**

У Београду, 31.8.2023